EFFECTIVE RESERVOIR MANAGEMENT FOR UNCONVENTIONAL RESERVOIRS USING THE FAST MARCHING METHOD AND MACHINE LEARNING

A Dissertation

by

TSUBASA ONISHI

Submitted to the Graduate and Professional School of
Texas A&M University
in partial fulfillment of the requirements for the degree of

DOCTOR OF PHILOSOPHY

Chair of Committee,	Akhil Datta-Gupta
Co-Chair of Committee,	Michael J. King
Committee Members,	Eduardo Gildin
	Yalchin Efendiev
Head of Department,	Jeff Spath

December 2021

Major Subject: Petroleum Engineering

ABSTRACT

Modeling unconventional reservoirs has been an active area of research in response to significant reserves in the U.S. Various analytical and numerical models incorporating relevant physics at varying fidelity levels have been proposed. A common approach to capture complex physics inherent in unconventional reservoirs is to run numerical reservoir simulations. However, fine spatio-temporal discretization is required to capture underlying nonlinear dynamics, resulting in long runtimes which are typically too computationally expensive to perform tasks like history matching and optimization. To address this challenge, the fast-marching method (FMM) based rapid simulation workflow has been proposed. The approach transforms original 2-D or 3-D problem into an equivalent 1-D problem along the diffusive time-of-flight (DTOF) coordinate representing travel time of pressure front propagation. The coordinate transformation enables significant savings in the computation time. To date, the powerful FMM-based simulation workflow has found many applications in modeling unconventional reservoirs, including rapid history matching and optimization. However, the approach poses certain limitations in capturing the effects of gravity because the physical direction of gravity is not necessarily aligned with the 1-D DTOF coordinate. Also, the current FMM calculations are difficult to generalize for irregular grid systems, such as unstructured grids, despite their increasing use in modern reservoir simulators.

Three major research contributions are made in this dissertation. First, we present an extension of the FMM-based simulation workflow that can account for gravity. The effects of gravity and multiphase flow are captured by retaining original discretization (gridblocks) for hydraulic fractures during the coordinate transformation. Second, a new FMM framework based on a finite-volume discretization of the Eikonal equation is developed as a generalization of the FMM calculations for irregular grid systems. The power and efficacy of the approach are demonstrated through its application to a variety of examples with different types of irregular grids. Third, an efficient deep learning-based approach that can visualize subsurface images, such as pressure propagation, in near real-time is developed. The FMM-based simulation workflow developed in the previous chapters is used in place of full-physics simulation to efficiently generate training datasets. The workflow is further enhanced by incorporating an autoencoder to perform a dimensionality reduction. The resultant subsurface visualizations can be readily used for qualitative and quantitative characterization and forecasting of unconventional reservoirs. The novelty of the approach is the framework which combines the strengths of deep learning-based models and the FMM-based rapid simulation.

DEDICATION

To my parents

ACKNOWLEDGEMENTS

I am deeply grateful to my supervisor, Dr. Akhil Datta-Gupta for his continuous support and guidance throughout my graduate school career. I would like to thank my co-chair, Dr. Michael J. King, and my committee members, Dr. Eduardo Gildin and Dr. Yalchin Efendiev, for their valuable suggestions during our discussions. I would also like to express my sincere gratitude to Dr. Masanori Kurihara and Dr. Nobuo Morita for their support and encouragements.

I wish to thank Feyi Olalotiti-Lawal, Atsushi Iino, Shusei Tanaka, and Nozomu Yoshida, for their mentorship. I credit much of my growth through summer internship positions that were offered by Los Alamos National Laboratory and Chevron. Many thanks to Derrick Berger and the IT crew for their software support services. Lastly, my appreciation also goes out to MCERI colleagues and alumni for being wonderful collaborators.

CONTRIBUTORS AND FUNDING SOURCES

Contributors

This work was supervised by a dissertation committee consisting of Professor Akhil Datta-Gupta (advisor), Michale J. King and Eduardo Gildin of the Department of Petroleum Engineering and Professor Yalchin Efendiev of the Department of Mathematics.

The fast-marching method (FMM)-based simulation workflow in Chapter 2 was an extension of the original work by Atsushi Iino. The FMM software used in Chapter 3 and Chapter 4 was developed by Hongquan Chen. The cases with unstructured grid systems in Chapter 3 were generated by Jaeyoung Park.

All other work conducted for the dissertation was completed by the student independently.

Funding Sources

Graduate study was supported by Texas A&M University Joint Industry Projects (JIP), Model Calibration and Efficient Reservoir Imaging (MCERI).

TABLE OF CONTENTS

Page

LIST OF FIGURES

LIST OF TABLES

CHAPTER I

INTRODUCTION*

1.1 Literature Review

There has been extensive research on the development and application of modeling approaches for tight unconventional reservoirs in response to their significant reserves in North America (EIA 2021). To date, many different approaches incorporating varying levels of data and physics have been proposed.

1.1.1 Analytical Models

For time series data, such as production data, decline curve analysis (DCA) (Arps 1945, Fetkovich 1980, Carter 1985, Fetkovich et al. 1987, Blasingame et al. 1991, Palacio

---

* Part of this chapter is reprinted with permission from Onishi, Tsubasa, Iino, Atsushi, Jung, Hye Young et al. 2020. Fast Marching Method Based Rapid Simulation Accounting for Gravity. Proc., Asia Pacific Unconventional Resources Technology Conference, Brisbane, Australia, 18-19 November 20191093-1111. Copyright 2020 Society of Petroleum Engineers. Further reproduction is prohibited without permission.

* Part of this chapter is reprinted with permission from Hongquan, Chen, Tsubasa, Onishi, Jaeyoung, Park et al. 2020. Computing Pressure Front Propagation Using the Diffusive Time of Flight in Structured and Unstructured Grid Systems Via the Fast Marching Method. Proc., SPE Annual Technical Conference and Exhibition. https://doi.org/10.2118/201771-MS. Copyright 2020 Society of Petroleum Engineers. Further reproduction is prohibited without permission.

* Part of this chapter is reprinted with permission from Chen, Hongquan, Onishi, Tsubasa, Park, Jaeyoung et al. 2021. Computing Pressure Front Propagation Using the Diffusive-Time-of-Flight in Structured and Unstructured Grid Systems via the Fast-Marching Method. SPE Journal: 1-21. Copyright 2021 Society of Petroleum Engineers. Further reproduction is prohibited without permission.

* Part of this chapter is reprinted with permission from Onishi, Tsubasa, Chen, Hongquan, Datta-Gupta, Akhil et al. 2021. An Efficient Deep Learning-Based Workflow Incorporating a Reduced Physics Model for Subsurface Imaging in Unconventional Reservoirs. Proc., SPE Annual Technical Conference and Exhibition. Copyright 2021 Society of Petroleum Engineers. Further reproduction is prohibited without permission.

and Blasingame 1993, Agarwal et al. 1999, Ilk et al. 2008, Duong 2010, Valkó and Lee 2010) and pressure/rate transient analysis (PTA/RTA) (Wattenbarger et al. 1998, Ilk et al. 2010, Song and Ehlig-Economides 2011, Nobakht and Clarkson 2012b, 2012a, Uzun et al. 2016, He, Cheng, et al. 2018) have been widely used for forecasting and reservoir characterization. While these methods provide significant benefits in terms of simplicity and computational efficiency, capturing complex physics inherent in unconventional reservoirs, such as heterogeneities of hydraulic fracture and reservoir properties, still remains a challenge.

1.1.2 Full-physics Numerical Models

Numerical simulations are capable of capturing complex nonlinear dynamics in unconventional reservoirs. Multiple continuum models (Warren and Root 1963, Kazemi, Merrill, et al. 1976), unstructured discrete fracture models (Cipolla et al. 2011, Cipolla et al. 2012, Sun and Schechter 2015, Marongiu-Porcu et al. 2016), multi-segment wells (Du et al. 2016), embedded discrete fracture models (EDFMs) (Li and Lee 2008, Moinfar et al. 2014, Ţene et al. 2017), and their hybrid models (Jiang and Younis 2016, Yang et al. 2018) are some of the notable numerical models. In most unconventional reservoir developments in the U.S., operators often first drill the minimum number of wells (parent wells) to hold the acreages, followed by drilling infill (child) wells to enhance the recovery (Lindsay et al. 2018). As many operators initiated their developments between 2003 and 2010, many parent wells have been depleted, leading to increasing number of infill wells in recent years. In fact, majority of the unconventional reservoirs have reached the point where the number of infill wells has surpassed that of newly drilled parent wells (Miller et al. 2016). Refracturing is another technique that can potentially improve the recovery from both parent and infill wells (Lindsay et al. 2016, Xu et al. 2017). Rather than the simple analytical models focusing on time series data, the capability of the numerical models that allows us to ‘see’ within the subsurface by visualizing the simulation results on discretized gridblocks, such as pressure and stress fields, is particularly useful to better design field development plans including well and completion spacing as well as treatment designs. However, performing computationally intensive tasks such as history matching, uncertainty quantification, and optimization for unconventional reservoirs involving complex multiphase flow and geomechanics in high contrast systems with hydraulic and natural fractures can be too expensive.

1.1.3 Reduced Order Models

To address the time consuming full physics simulations, the use of fast proxy or surrogate models has been extensively investigated. Reduced order models (ROMs) using a proper orthogonal decomposition (POD) (Van Doren et al. 2006, Cardoso et al. 2009, He and Durlofsky 2014, Ghasemi et al. 2015) or a dynamic mode decomposition (DMD) (Ghommem et al. 2013, Ghommem et al. 2016, Kutz et al. 2016, Bao and Gildin 2017) are some of the popular approaches on the basis of model decomposition. Although efficient, the training (offline) procedure requiring multiple full simulation runs can be computationally expensive. As a result, while applications of such ROMs to cases like 2D or simple 3D cases in both conventional and unconventional reservoirs are available (He et al. 2013, Klie and Florez 2020), field scale applications have not yet been fully explored.

1.1.4 The Fast-Marching Method-Based Rapid Simulation

In an effort to overcome the challenges posed by existing modeling approaches for unconventional reservoirs, applications of an asymptotic approach to the diffusivity equation have been proposed (Xie et al. 2015). The use of a high-frequency asymptotic solution to the diffusivity equation leads to the Eikonal equation which governs the propagation of a pressure front propagation and generalizes the depth of investigation (Lee 1982) for heterogeneous reservoirs. Vasco et al. (2000) and Kulkarni et al. (2001) presented trajectory-based solutions to the Eikonal equation. Specifically, the trajectories are approximated by ray path (Vasco et al. 2000) or by convective streamlines (Kulkarni et al. 2001), then the phase or diffusive time-of-flight (DTOF) are obtained by calculating the line integral along the trajectories. An alternative approach to computing the DTOF is the fast marching method (FMM), a class of front-tracking algorithm, which does not require explicit construction of the trajectories and can solve the Eikonal equation efficiently without iterations (Sethian 1999).

The DTOF represents the propagation time of the peak pressure disturbance caused by an impulse source. The propagation distance is known as the depth of investigation and the associated volume defined as drainage volume, which is the region of the reservoir contributing to the production of the well at any given time. The DTOF and drainage volume are quite useful quantities and have found many applications in modeling unconventional reservoirs. For example, we can visualize the drainage volume evolution by thresholding the propagation time at selected time intervals. This offers visual appeal and physically intuitive representation of the complex interaction between hydraulic and natural fractures and can be utilized in order to optimize development plans, such as the number of hydraulic fracturing stages and their spacing (Vasco and Datta-Gupta 2016). Besides the visualizations, the DTOF can be used as a spatial coordinate in flow simulation. Specifically, we can transform original 2-D or 3-D problems into equivalent 1-D problems along the DTOF (Zhang et al. 2016). This leads to substantial savings in computational time in the numerical simulation while maintaining accuracy. The original work (Zhang et al. 2016) focused on modeling shale-gas reservoirs. Later, the approach has been extended to account for more complex problems, such as multiphase and multicomponent flow (Fujita et al. 2016, Iino, Onishi, et al. 2020) and non-isothermal flow (Cui et al. 2016), as well as complex grid systems including multiple continuum models (Fujita et al. 2016), unstructured discrete fracture models (Yang et al. 2017), and EDFMs (Xue, Yang, et al. 2019a). Yang et al. (2015) and Xue, Yang, Park, et al. (2019) proposed another class of approach using the concept of DTOF for production data analysis. In their approach, instead of solving the Eikonal equation using the FMM, the DTOF and $w(\tau)$ function, which is defined as derivative of drainage pore volume with respect to the DTOF, are obtained from the production data. The data-driven diagnostic plots using the DTOF and $w(\tau)$ function offer a simple and intuitive understanding of the transient-drainage volume and fracture conductivity. In this study, we focus on solving the Eikonal equation using the FMM.

The success of the DTOF-based approaches is contingent on the FMM. While well established for reservoir models with structured grid systems, the FMM is less straightforward in more general grid systems. For example, special treatments, such as sub-gridding are required to handle unstructured grids (Yang et al. 2017), local grid refinements, and EDFMs (Xue, Yang, et al. 2019a). Such algorithms are typically less efficient and difficult to generalize. In addition to the discrete fracture models, dual-porosity dual-permeability (DPDK) models where both matrix and fracture contribute to the flow are also widely used for modeling unconventional reservoirs (Hui et al. 2019, Thomas et al. 2019, Yang et al. 2018, Kumar et al. 2019). Although the FMM applications are successful in the dual-porosity single-permeability (DPSK) (Zhang et al. 2016) and triple-porosity single-permeability (TPSK) systems (Fujita et al. 2016), explicit tracking of the pressure front in the two interacting continua in DPDK systems is challenging. Furthermore, because the physical direction of gravity is not necessarily aligned with the 1D DTOF coordinate, it is challenging to incorporate gravity effects in the current FMM-based simulation workflow.

1.2.5 Deep Learning-Based Models

The success of deep learning in a variety of fields including computer vision, natural language processing, and many others (Goodfellow et al. 2016) has led to the use of such techniques in subsurface modeling. We note here that the following literature review is focused on the models for predicting state maps that are relevant to our focus in the dissertation, rather than simpler models, for example, ones with a univariate output dimension. One of the earliest works reported by Zhu and Zabaras (2018) showed an application of an image-to-image regression using a convolutional encoder-decoder network, whereby gridblocks in the discretized flow domain are treated like pixels in an image, to construct a surrogate model that predicts state maps given permeability maps.

The model is applied to a simple problem involving single phase steady-state flow with Gaussian permeability distribution. Extensions of the approach to multiphase flow (Mo et al. 2019) and non-Gaussian conductivity fields (Mo et al. 2020) were presented. In the context of reservoir simulation, Tang et al. (2020) applied a residual U-Net (Ronneberger et al. 2015) and a convolutional long short term memory recurrent neural network (Hochreiter and Schmidhuber 1997) to develop a surrogate model that predicts state maps and flow responses at wells, given permeability maps in 2D channelized reservoir models. An application of the surrogate model within a probabilistic history matching workflow has been demonstrated. Subsequently, Zhong et al. (2021) presented a slightly different deep learning-based surrogate model using the coupled generative adversarial network (Co-GAN) that predicts pressure and saturation simultaneously. Several recent works have focused on the application of such techniques for modeling geologic CO_2 sequestration (Tang, Fu, et al. 2021, Tang, Ju, et al. 2021, Wen et al. 2021, Yan, Harp, Chen, et al. 2021). Recently, there has been intensive research efforts on investigating the use of deep learning-based methods to solve forward and inverse problems in science and engineering applications. Notable works that brought a new paradigm of data-driven modeling have been presented by Raissi et al. (2019) and Zhu et al. (2019). The method is often referred to as physics-informed neural network (PINN) or physics-informed machine learning (PIML). While standard deep learning models are typically trained solely using data, the loss function in the PIML framework consists of data misfit term(s) as well as regularization term(s) based on some physical laws, which are typically residuals of governing partial differential equations, to ensure that the trained model is consistent with the given underlying physical laws. Partial derivatives in the physics term can be readily computed by leveraging the automatic differentiation (Baydin et al. 2018). In the field of reservoir modeling, applications of the PIML framework to the Buckley Leverett problem (Buckley and Leverett 1942) have been investigated by several authors (Fraces et al. 2020, Fuks 2020, Xu et al. 2021). More recently, Yan, Harp, and Pawar (2021) presented applications of PIML for modeling geologic CO_2 sequestration. Despite the widespread use of deep learning-based methods for subsurface modeling in recent years, the applications are mostly limited to simple cases like two phase flows in 2D or simple 3D grid systems. The challenge here is that the workflow becomes very expensive as the complexity of the problem in terms of size in space and time and nonlinearity increases. There are two components contributing to the expensive runtime: generating datasets for training by running a large number of full physics simulations and the training (solving the minimization problem) to find optimal weights and biases of the neurons. The latter tends to be more evident in the PIML framework due to the physics term(s) in the loss function that typically results in slower convergence, as in other minimization problems with regularizations.

1.2 Dissertation Outline

We present extensions of the Fast-Marching Method (FMM)-based rapid simulation workflow and a variety of applications of the developed method. Details on these are provided in the following chapters. The highlights of each chapter are as follows:

- In the 2nd chapter, we present an extension of the FMM-based simulation that can account for gravity segregation and multiphase flow in hydraulic fracture planes. The implementation is first validated with a full-physics numerical simulator using illustrative examples. Then, an application to a 3D field-scale unconventional reservoir is presented to demonstrate the robustness of the approach.
- In the 3rd chapter, we propose a generalized FMM for arbitrary finite-volume grid systems. A motivation for this work comes from the increasing use of irregular grid systems, such as multiple continuum and unstructured grids, in modern reservoir simulators and the limitations in the current FMM solvers for such grid systems. The new approach is first validated with analytical solutions using cases involving homogeneous reservoir properties. Then, the versatility and efficacy of the approach are demonstrated through the applications of the approach to a variety of irregular grid systems at varying levels of complexity.
- In the 4th chapter, we present a novel deep learning-based workflow incorporating the FMM-based simulation that can efficiently visualize well drainage volume and pressure front propagation in unconventional reservoirs in near real-time. The approach combines the strengths of deep learning-based models and the FMM-based rapid simulation and for the first time, allows data-driven visualization of unconventional well drainage volume in 3D.

CHAPTER II

FAST MARCHING METHOD BASED RAPID SIMULATION ACCOUNTING FOR GRAVITY[†]

2.1 Chapter Summary

The fast marching method (FMM)-based rapid reservoir simulation workflow has proven to be effective for various applications in unconventional reservoirs. The FMM-based simulation relies on the concept of the 'Diffusive-Time-of-Flight' (DTOF) that represents the travel time of pressure front propagation and captures geological heterogeneity as a 1-D spatial coordinate. It is challenging to model gravity in the FMM-based approach because the 1-D DTOF coordinate is not necessarily aligned with the physical direction of gravity.

We present a novel FMM-based simulation workflow that can account for gravity segregation in the fracture planes. The DTOF is first obtained by solving the Eikonal equation using the FMM assuming that gravity segregation is negligible in the ultra-tight matrix domain. Next, the 3-D transport problems in the matrix domain are transformed into a 1-D problem using the DTOF as a spatial coordinate. The hydraulic fractures are treated as gridded 2D planes to allow for gravity segregation and are connected to the 1-

---

[†] Part of this chapter is reprinted with permission from "Onishi, Tsubasa, Iino, Atsushi, Jung, Hye Young et al. 2020. Fast Marching Method Based Rapid Simulation Accounting for Gravity. Proc., Asia Pacific Unconventional Resources Technology Conference, Brisbane, Australia, 18-19 November 20191093-1111". Copyright 2020 Society of Petroleum Engineers. Further reproduction is prohibited without permission.

D matrix domain through non-neighbor connections (NNCs). A critical aspect here is computing the matrix-fracture transmissibilities based on the surface area of the DTOF contour. The proposed approach retains the speed of the FMM-based simulation while incorporating additional dominant physical mechanisms.

The FMM based model is benchmarked with a commercial finite volume simulator using a series of synthetic and field scale numerical examples encompassing different levels of geologic complexity to illustrate the accuracy and efficiency of the approach. We applied our proposed model and the standard FMM-based approach to synthetic cases and a field scale example with multi-million gridblocks and over 100 hydraulic fractures and compared flow responses and CPU time. It is found that the proposed approach effectively captures gravity effects, and the results are in close agreement with 3-D finite volume simulation compared to the standard FMM-based approach. The FMM-based approaches are orders of magnitude faster in CPU time than the 3-D finite volume simulation. These numerical examples clearly demonstrate that our proposed approach is able to adequately model gravity effects while retaining computational efficiency.

The uniqueness of this work is incorporating gravity effects for the first time in the FMM-based reservoir simulation framework. The proposed approach is relatively simple and easy to implement, and the rapid workflow is capable of performing field scale history matching and optimization much faster and within realistic time frame.

2.2 Introduction

Unconventional reservoirs account for a significant amount of hydrocarbon reserves in the U.S. (EIA 2021). In order to better understand the performance of unconventional reservoirs, analytical and numerical models incorporating relevant physics at varying fidelity levels have been developed. Decline curve analysis (Arps 1945, Fetkovich 1980) and pressure/rate transient analysis (Song and Ehlig-Economides 2011) are commonly used for fracture characterization and well performance predictions. While these analytical models provide significant benefits in terms of computational efficiency and simplicity, capturing important details such as heterogeneities of reservoir properties remains a considerable challenge.

High-fidelity, full-physics numerical simulators that typically employ finite volume schemes are capable of simulating detailed non-linear descriptions. For fractured media, many approaches including multiple continuum models (Warren and Root 1963, Kazemi, Merrill, et al. 1976), unstructured discrete fracture models (Karimi-Fard and Firoozabadi 2001), and embedded discrete fracture models (EDFMs) (Li and Lee 2008, Moinfar et al. 2014) have been presented. For unconventional reservoirs, detailed spatial and temporal discretization is required to accurately model multiphase flow in complex fracture networks and high contrast systems and therefore numerical models tend to be computationally expensive. This challenge has been partly mitigated by state-of-the-art solvers, parallelization, and new numerical schemes; however, it is still too expensive to perform uncertainty assessments, history matching, or optimizations where hundreds or thousands of simulations may be required. The FMM-based approach has been applied to rapid flow simulations accounting for realistic and complex flow physics such as multi-phase and multi-component flow, non-isothermal flow, multiple continuum, and unstructured grid systems (Zhang et al. 2016, Fujita et al. 2016, Yang et al. 2017, Iino, Onishi, et al. 2020). The rapid workflow enables us to explore complex interactions among a large number of uncertain variables in field scale history matching and optimization problems (Iino et al. 2017).

In an effort to improve computational efficiency in the numerical models, the Fast Marching Method based rapid flow simulation workflow has been proposed (Zhang et al. 2016). This approach relies on a high frequency asymptotic solution of the diffusivity equation leading to the Eikonal equation in which we generalize the concept of radius of investigation (Lee 1982) for heterogeneous media. The Eikonal equation can be efficiently solved using the FMM for diffusive time of flight (DTOF), which is a representation of travel time of the 'peak' pressure response corresponding to an impulse source (Datta-Gupta et al. 2011, Vasco and Datta-Gupta 2016). The 3-D problems are simplified into equivalent 1-D problems along the DTOF, leading to a significant speedup.

It is worth mentioning that, recently, another class of approach, physics-based data-driven models, has been proposed (Zhang et al. 2018). In this approach, instead of starting from a reservoir model and calculating DTOF for the 3-D to 1-D coordinate transform, they introduced a new diffusive diagnostic function (DDF) which is also used to formulate a 1D flow equation, but different than the formulation using the DTOF. The workflow starts from data, instead of a reservoir model, and performs history matching using the available observed data and the 1-D simulation model in which DDFs are tuning parameters. History matched DDFs can be used for flow diagnostics in unconventional reservoirs. Later, an extension of the approach that can adjust other parameters, such as initial pressure and saturation distributions, together with DDFs was presented (Zhang et al. 2019).

In this study, we focus on improving the numerical model using the FMM. Specifically, we present an extension of the FMM based flow simulation approach that can account for gravity segregation in the fracture planes. Because the physical direction of gravity is not aligned with the 1D DTOF coordinate, it is challenging to incorporate gravity effects in the current workflow. In our approach, unlike the standard FMM-based approach, we treat the hydraulic fracture domain and the matrix domain separately. The DTOF in the matrix domain is first obtained by solving the Eikonal equation using the FMM. Next, the 3-D problems in the matrix domain are transformed into 1-D problems using the DTOF as a spatial coordinate, assuming that gravity segregation is negligible in the ultra-tight matrix domain. The hydraulic fractures are treated as 2D planes to allow for gravity segregation. Each of the gridblocks in the hydraulic fracture planes is linked with the first gridblock in the 1-D matrix domain through non-neighbor connections (NNCs). The idea is similar to EDFMs, in which matrix-fracture connections are described by NNCs.

The outline of this chapter is as follows. First, we present the simulation model formulation including the concept of the DTOF and coordinate transformation of the 3-D flow equation into an equivalent 1-D flow equation along the DTOF. Next, we provide the steps involved in our workflow to incorporate gravity effects. Then we present synthetic illustrative examples. Finally, we demonstrate the robustness of our approach using a field scale unconventional reservoir.

2.3 Methods

The key concept of our FMM-based approach is transformation of the 3-D flow equation into equivalent 1-D flow equation along the DTOF coordinate. This section presents the concept of the DTOF and the coordinate transformation of diffusivity equation from 3-D space into 1-D DTOF space. Also, a detailed description of the proposed FMM based simulation approach accounting for gravity (FMMG) will be discussed.

2.3.1 Diffusive Time-of-Flight

Pressure propagation in porous media is a diffusive process but we can draw an analogy with propagating waves (Vasco and Datta-Gupta 2016). A high frequency asymptotic solution for diffusivity equation leads to the Eikonal equation governing the "phase" of propagating disturbance of pressure, which is represented by the DTOF. We will refer to this as the pressure 'front' analogous to wave fronts. The DTOF can be obtained by solving the Eikonal equation (Eq. (2.1)) which is derived from the diffusivity equation and its asymptotic solution (Datta-Gupta and King 2007, Vasco and Datta-Gupta 2016),

$$\left|\nabla \tau(\mathbf{x})\right| = \frac{1}{\sqrt{\alpha(\mathbf{x})}} \tag{2.1}$$

where τ and α represent the DTOF and diffusivity at location **x**, respectively. Under multi-phase conditions, we define diffusivity as follows,

$$\sqrt{\alpha(\mathbf{x})} = \frac{\lambda_t(\mathbf{x})k(\mathbf{x})}{\phi(\mathbf{x})c_t(\mathbf{x})} \tag{2.2}$$

where ϕ: porosity, k: permeability, λ_t: total mobility and c_t: total compressibility. The Eikonal equation is a generalization of the well-known concept of radius of investigation for homogeneous reservoirs in the sense that it allows us to have spatial heterogeneity in the diffusivity. The Eikonal equation can be efficiently solved for the DTOF using the FMM, which is a class of front tracking methods constructing the DTOF solution in an orderly one-pass fashion outwards from the sources (Sethian 1999). Figure 2.1 shows examples of the DTOF calculated for homogeneous and heterogeneous reservoir models using the FMM where arbitrary well geometry can be accounted for including vertical, deviated/ horizontal, and multi-stage hydraulically fractured wells.

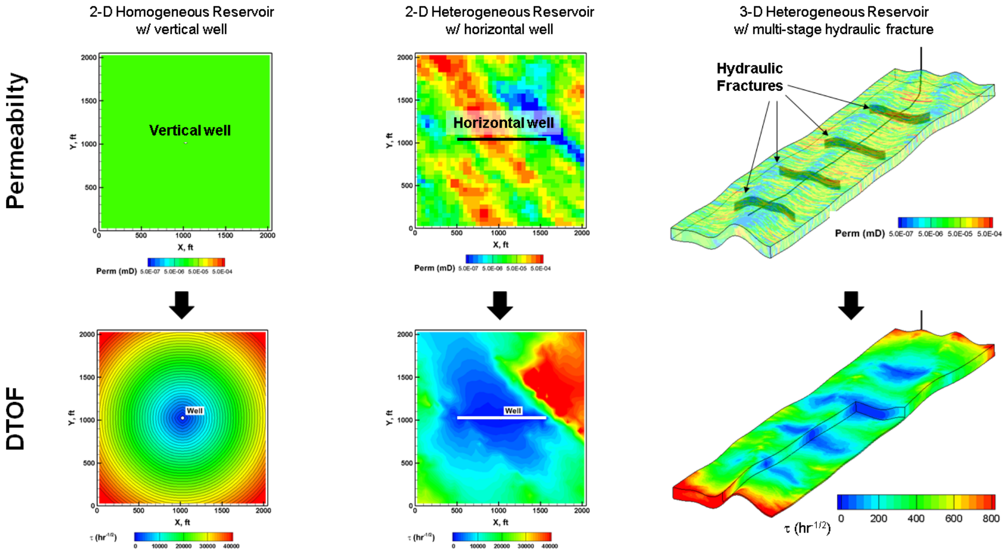

(a) (b) (c)

Figure 2.1 Examples of DTOF (Iino et al. 2019): Upper row is permeability distributions and lower row is the corresponding DTOF. (a) 2-D homogeneous reservoir with a vertical well. (b) 2-D heterogeneous reservoir with a horizontal well. (c) 3-D heterogeneous reservoir with a multi-stage hydraulically fractured well (reprinted with permission from Onishi et al., 2020).

2.3.2 Diffusive Time-of-Flight as a Spatial Coordinate

The key idea of the rapid simulation based on the FMM is to utilize the DTOF as spatial coordinate in order to recast 3-D flow equations into equivalent 1-D flow equations. Figure 2.2 illustrates 2-D homogenous (left) and heterogeneous (right) reservoirs with a vertical well depicted by stars. We expect circular propagation of the pressure front as depicted by the DTOF in homogeneous reservoirs, whereas the DTOF in heterogeneous reservoirs will be distorted due to the spatial heterogeneity. The diffusivity equation for heterogeneous reservoirs can be formulated along the DTOF coordinate which embeds the spatial heterogeneity.

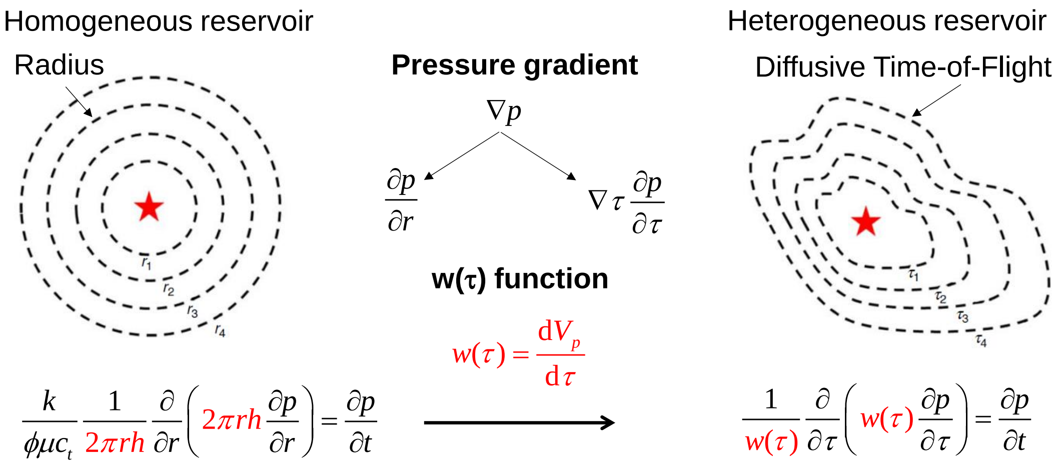

Figure 2.2 Analogy between the DTOF as a spatial coordinate and radial coordinate in a homogeneous reservoir (Zhang et al. 2016) (reprinted with permission from Onishi et al., 2020)

Zhang et al. (2016) proposed a novel approach of coordinate transformation from physical 3-D space into 1-D DTOF space, leading to the following diffusivity equation using the DTOF coordinate,

$$\frac{1}{w(\tau)}\frac{\partial}{\partial\tau}\left[w(\tau)\frac{\partial p}{\partial\tau}\right]=\frac{\partial p}{\partial t} \tag{2.3}$$

where single-phase, constant compressibility, and viscosity are assumed for simplicity. In the 1-D equation (Eq. (2.3)), the $w(\tau)$ function is defined as the derivative of drainage pore volume, V_p, with respect to the DTOF,

$$w(\tau)=\frac{\mathrm{d}V_p(\tau)}{\mathrm{d}\tau} \tag{2.4}$$

Comparison of Eq. (2.3) with the radial flow equation in Figure 2.2 reveals that $w(\tau)$ function physically represents surface area of the propagating pressure front. Solution of the Eikonal equation (Eq. (2.1)) using the FMM gives the DTOF mapped on gridblocks. The $w(\tau)$ can be calculated based on the drainage pore volume, V_p, that is accumulated as a function of the DTOF (Zhang et al. 2016). Extension to more complicated cases, such as compressible fluid, multi-phase and multi-component flow, has also been proposed to date (Fujita et al. 2016, Iino, Onishi, et al. 2020).

2.3.3 Workflow of the FMMG

The standard FMM and FMMG approaches are summarized in Figure 2.3. In this figure, the top row, with red arrows, and the bottom row, with blue arrows, correspond to the FMM (Iino 2018) and the FMMG workflows, respectively. As seen in Figure 2.3, the FMMG approach is in many ways fundamentally similar to the standard FMM workflow. Therefore, we will focus on important aspects for the FMMG implementation in this section. First, multi-phase diffusivity on original 3D gridblocks is computed based on the initial reservoir properties. Next, the Eikonal equation is solved by FMM for the DTOF.

Here, we apply the multi-stencil FMM, in which each node has 26 neighbors in 3D space (8 neighbors in 2D) (Hassouna and Farag 2007). This treatment plays an important role to better represent pressure front propagation, especially in high contrast media like hydraulic fractures in unconventional reservoirs (Li 2018). In this step, we have special treatments in the FMMG to obtain surface area of the hydraulic fracture corresponding the first $w(\tau)$, which will be used to calculate transmissibilities between the hydraulic fracture gridblocks and the 1-D DTOF gridblocks representing the rest of the domain. This can be done by setting the source points along hydraulic fracture planes from which we start front tracking, as shown in Figure 2.4. As a result, a uniform DTOF(=0) is obtained within the hydraulic fracture plane using the FMMG approach, while we see propagating DTOF in the FMM (step 2). Once we obtain the DTOF, we utilize the DTOF as a 1-D spatial coordinate and calculate the drainage pore volume, V_p, along the 1-D DTOF coordinate (step 3). Next, V_p is discretized on the 1-D DTOF coordinate (step 4) and calculate the $w(\tau)$ function (step 5). We note here that the $w(\tau)$ function in the FMMG shows slightly greater values compared to the standard FMM at early time, with similar trends at late time (step 5). This is because the first $w(\tau)$ in the FMMG corresponds to the surface area of the 2-D hydraulic fracture plane, whereas, there can be several 1-D gridblocks ($w(\tau)$) within the hydraulic fracture plane, (number of 1D-gridblocks ($w(\tau)$) varies depending on the discretization scheme) in the standard FMM approach. Finally, the 1-D (+2D hydraulic fracture plane if FMMG) simulation will be performed using the pore volume and transmissibilities obtained from the previous steps. In the FMMG approach, connections between the hydraulic fracture plane and the first DTOF gridblock are described by NNCs (step 6). In this step, we calculate transmissibilities between each gridblock in the hydraulic fracture plane and the first 1-D gridblock, T_i as,

$$T_i = w_i T_{ave} \tag{2.5}$$

where $w_i = A_i / A_{HF}$, A_i is the surface area of a gridblock in the hydraulic fracture plane, AHF is the total surface area of the hydraulic fracture plane, and T_{ave} is an average transmissibility between the hydraulic fracture plane and the first 1-D grid that can be obtained using the first $w(\tau)$. The computed transmissibilities using Eq. (2.5) will be used as part of NNC inputs in the 1-D flow simulation.

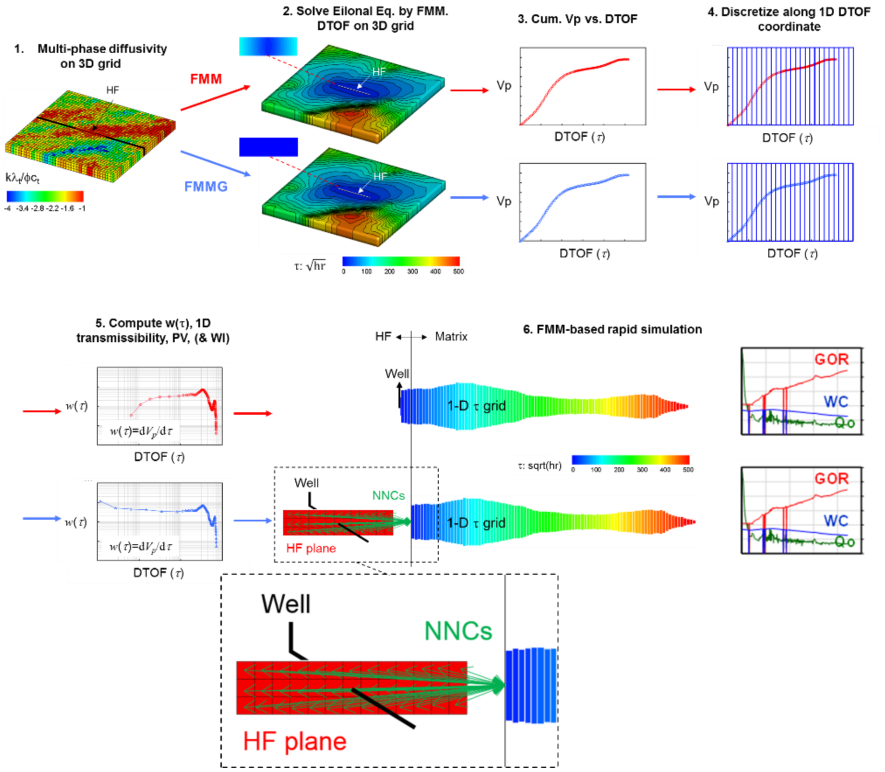

Figure 2.3 An Illustration of the standard FMM-based simulation workflow (top row with red arrows) and the FMM-based simulation workflow accounting for gravity (FMMG) (bottom row with blue arrows) (reprinted with permission from Onishi et al., 2020)

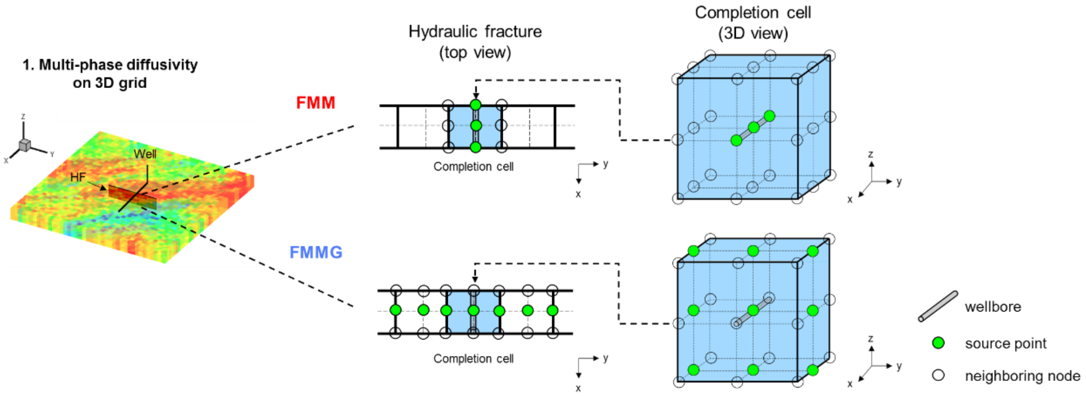

Figure 2.4 Source points set-up for the standard FMM (top) and the FMMG (bottom) (reprinted with permission from Onishi et al., 2020)

2.4 Validation

We present cases to validate our FMM-based approaches using a commercial reservoir simulator (https://www.software.slb.com/products/eclipse). In this section, we first focus on 2D examples without gravity to validate implementation of the transmissibility calculations for NNCs in the FMMG workflow. The capability of the FMMG for capturing effects of gravity in 3-D examples will be analyzed in the next section.

2.4.1 Example 1. 2D Homogeneous Case

We begin with a single phase 2D homogeneous problem with a single hydraulic fracture. The geometry and reservoir properties are provided in Figure 2.5(a). The flow domain is discretized into 101×101×1 gridblocks, and tartan gridding is used to describe the hydraulic fracture. A slightly compressible system is assumed. The well produces water with a constant rate of 1.0 (stb/d) for 500 days. Computed DTOF maps obtained from the FMMG and the standard FMM are provided in Figure 2.5(b) and (c). Similar trends are obtained in the top view (Figure 2.5(b) and (c), top), whereas we see different results between the FMMG and FMM in the hydraulic fracture plane (Figure 2.5(b) and (c), bottom). Specifically, while the FMMG shows DTOF=0 in the hydraulic fracture planes, the FMM shows small DTOF in the hydraulic fracture plane. This is because we setup the source points (DTOF=0) along the hydraulic fracture in the FMMG approach Figure 2.4. Using these results, the drainage pore volumes and $w(\tau)$ functions are calculated along the DTOF coordinate as shown in Figure 2.6, in which different flow regimes can be identified between the FMMG and the standard FMM at early time. This is because, as discussed earlier, the first $w(\tau)$ in the FMMG corresponds to the surface area of the hydraulic fracture (the first point on the blue line in Figure 2.6), therefore we see linear flow in the matrix immediately after the first $w(\tau)$ in the FMMG, followed by radial flow, and finally boundary dominated flow. Detailed discussions of the flow diagnostics using $w(\tau)$ functions are summarized in Xu et al., (2018). On the other hand, in the standard FMM, we see pressure propagation in the hydraulic fracture at early time, followed by a similar profile to the FMMG beyond the hydraulic fracture plane. These observations are consistent with the visual comparison of the DTOF map (Figure 2.5).

Simulation results in terms of bottom-hole pressure (BHP) are compared as shown in Figure 2.7. Both the FMMG and the standard FMM show excellent agreement with the commercial finite volume simulator, validating our implementation of the transmissibility calculations for homogeneous media.

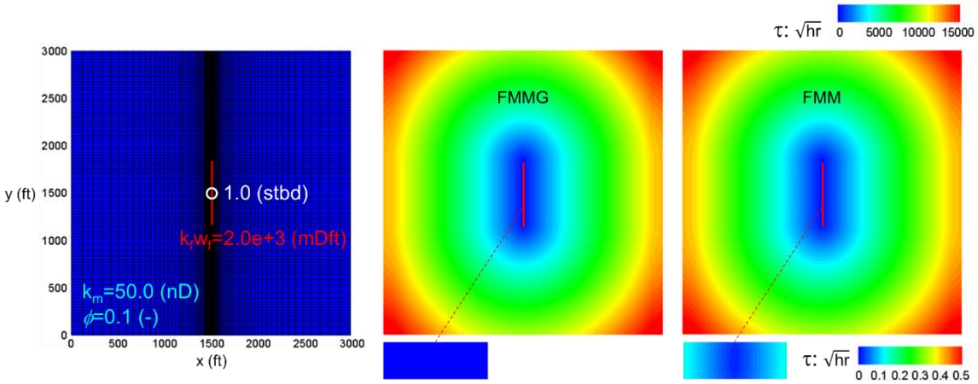

Figure 2.5 Homogeneous 2D model showing (a) uniform permeability distribution with a hydraulic fracture located at the center on the red line, (b) DTOF map based on FMMG, and (c) DTOF map based on FMM (reprinted with permission from Onishi et al., 2020)

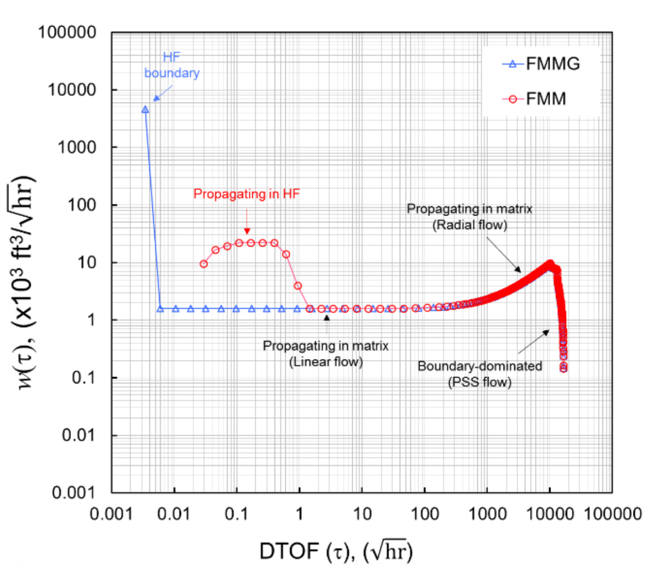

Figure 2.6 Comparison of the $w(\tau)$ function for the FMMG (blue) and the FMM (red) (reprinted with permission from Onishi et al., 2020)

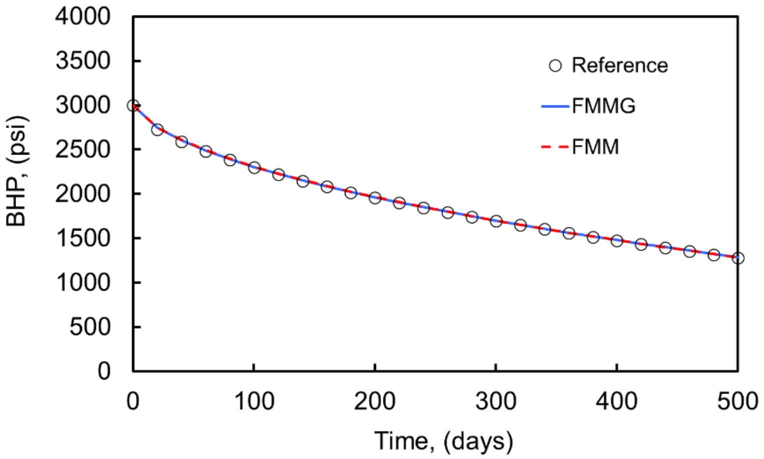

Figure 2.7 Model validation results showing comparison of simulated BHP responses between the commercial finite volume simulator (reference), the FMMG, and the standard FMM (reprinted with permission from Onishi et al., 2020)

2.4.2 2D Heterogeneous Case

Next, we demonstrate the FFMG model with a 2D heterogeneous reservoir with a single hydraulic fracture described by tartan gridding, to illustrate the capability of our approach for heterogeneous media. The model size is $6000 \times 6000 \times 100$ (ft^3) with $218 \times 200 \times 1$ grid discretization. The heterogeneous permeability field is provided in Figure 2.8(a). A slightly compressible system is assumed to have uniform porosity values of 0.1. Water was produced with a constant rate of 5.0 (stb/d) for 500 days. The computed DTOF maps in this example resulted in twisted trends reflecting the effect of the heterogeneity as shown in Figure 2.8(b) and (c). The $w(\tau)$ diagnostic plot based on the DTOF maps is provided in Figure 2.9, in which we see similar trends compared to the previous example.

Bottom-hole pressure (BHP) comparison is presented in Figure 2.10. Again, both the FMMG and the standard FMM show excellent agreement with the commercial finite volume simulator, validating our implementation of the transmissibility calculations for heterogeneous media.

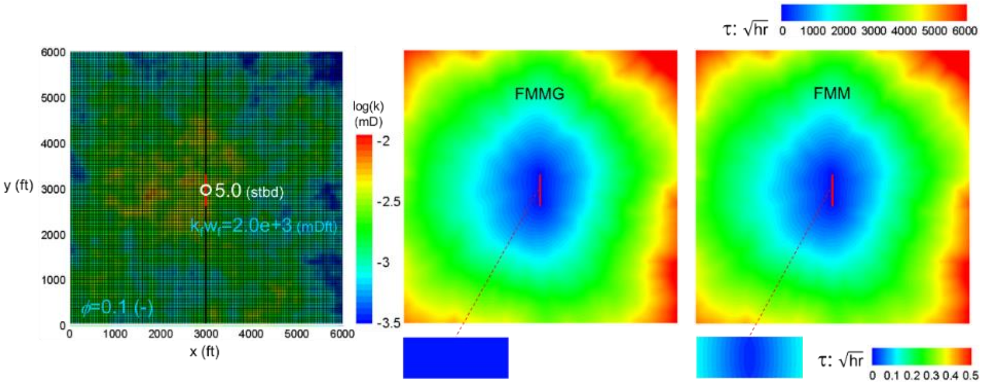

Figure 2.8 Heterogeneous 2D model showing (a) heterogeneous permeability distribution with a hydraulic fracture located at the center on the red line, (b) DTOF map based on FMMG, and (c) DTOF map based on FMM (reprinted with permission from Onishi et al., 2020)

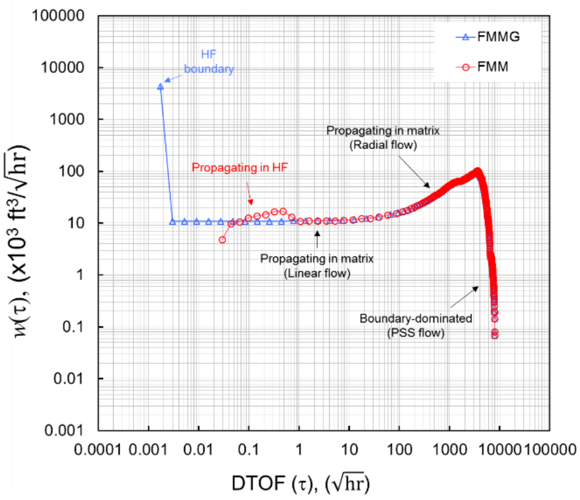

Figure 2.9 Comparison of the $w(\tau)$ function for the FMMG (blue) and the FMM (red) (reprinted with permission from Onishi et al., 2020)

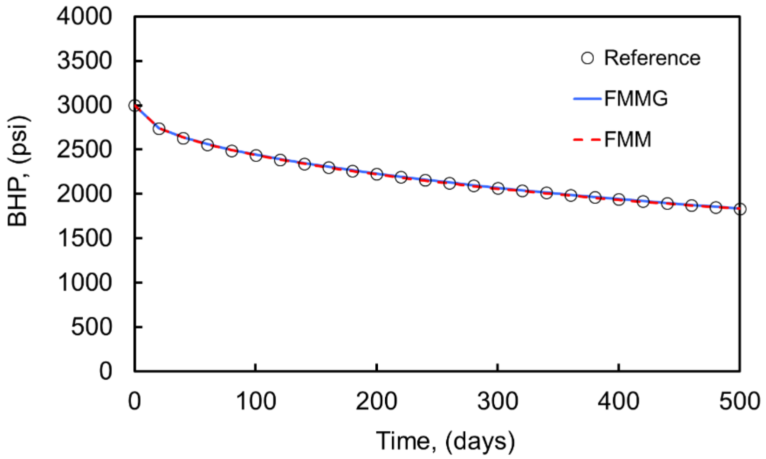

Figure 2.10 Model validation results showing comparison of simulated BHP responses between the commercial finite volume simulator (reference), the FMMG, and the standard FMM (reprinted with permission from Onishi et al., 2020)

2.5 Applications

Next, we apply the FMMG scheme to 3D multi-phase examples including synthetic and field scale models to examine capability of the FMMG for modeling gravity segregation. These applications are sufficiently realistic and complex to demonstrate the practical feasibility of our approach.

2.5.1 3D Heterogeneous Reservoir

In this example, we consider a synthetic unconventional reservoir. As shown in Figure 2.11, the model comprises a single horizontal well with 15 planner hydraulic fractures described by tartan gridding. Heterogeneous permeability distribution for the matrix and the stimulated reservoir volume (SRV), and a uniform porosity of 0.04 for the whole domain are assumed. The fluids modeled in this example are described by water, oil, and gas phases. Relative permeability curves and PVT data are provided in Figure

2.12 and Figure 2.13, respectively. Transmissibility reductions due to rock compaction effects are modeled using different tables for the hydraulic fractures, the SRV region, and the matrix (Figure 2.14). We applied a uniform initial pressure of 3,300 psi (initially undersaturated). Uniform water saturation values of 0.2, 0.3, and 0.6 are assigned to the matrix, the SRV, and the hydraulic fractures to mimic water saturation distribution at the end of hydraulic fracturing treatments. The well produces fluids for 1000 days with a constant BHP control of 1000 psi.

Computed DTOF maps are shown in Figure 2.15, and the $w(\tau)$ diagnostic plot based on the DTOF maps is provided in Figure 2.16. Here, again we see different trends between the FMM and FMMG results at early time, and subsequent flow regimes are similar in the two approaches. In this example, we see different flow regimes than the previous examples due to multiple hydraulic fracture planes and the SRV region.

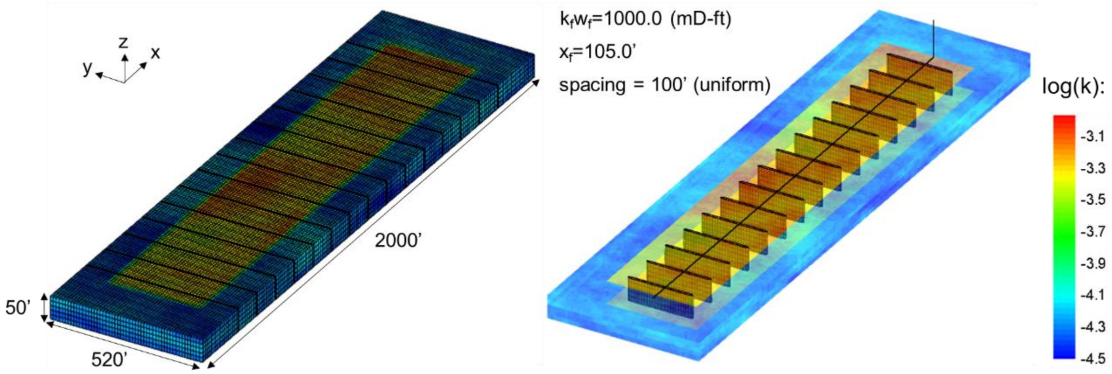

Figure 2.11 Heterogeneous 3D model showing logarithm of permeability distribution (left), and hydraulic fracture geometry and properties (right) (reprinted with permission from Onishi et al., 2020)

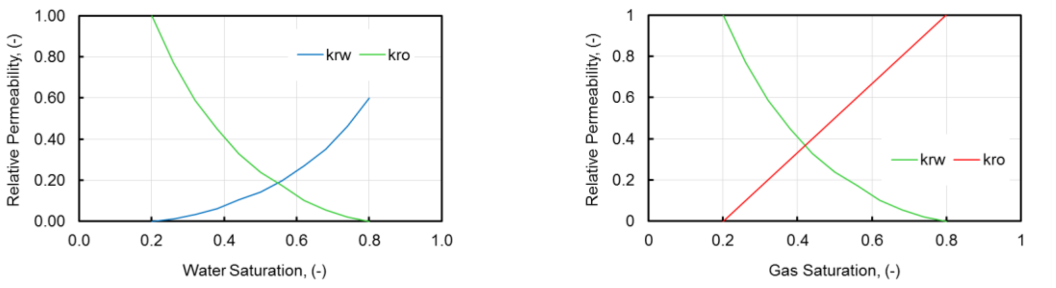

Figure 2.12 Relative permeability curves (reprinted with permission from Onishi et al., 2020)

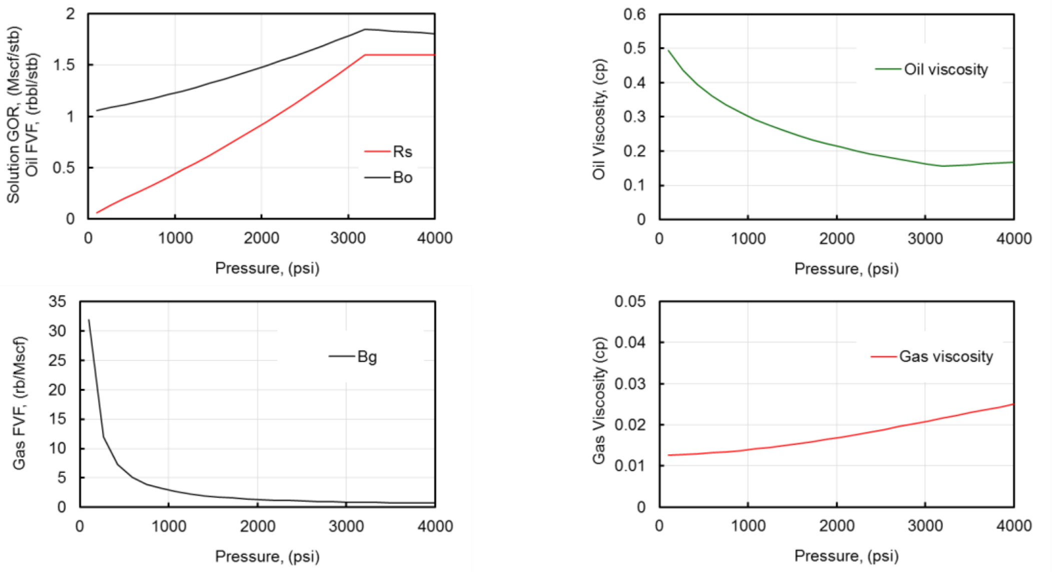

Figure 2.13 PVT data (reprinted with permission from Onishi et al., 2020)

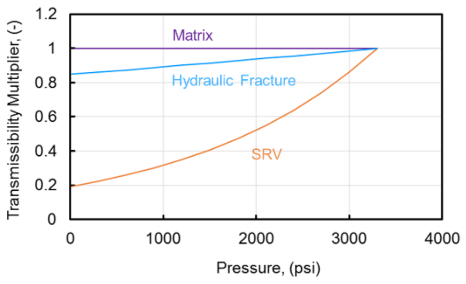

Figure 2.14 Rock compaction table (reprinted with permission from Onishi et al., 2020)

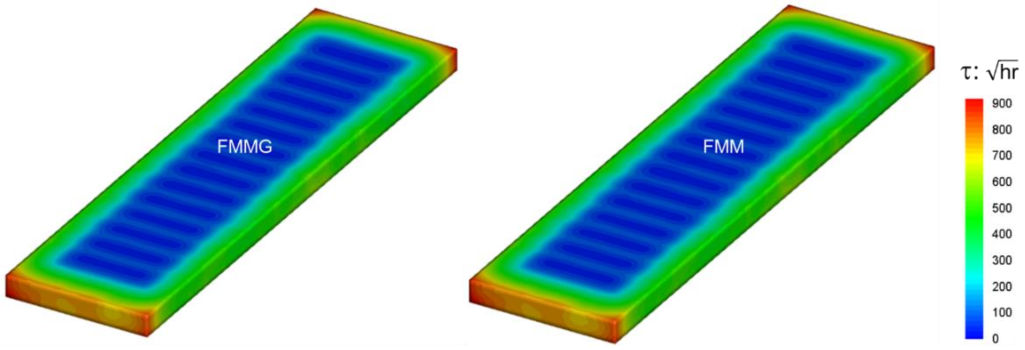

Figure 2.15 Comparison of the DTOF maps for the FMMG (left) and the FMM (right) (reprinted with permission from Onishi et al., 2020)

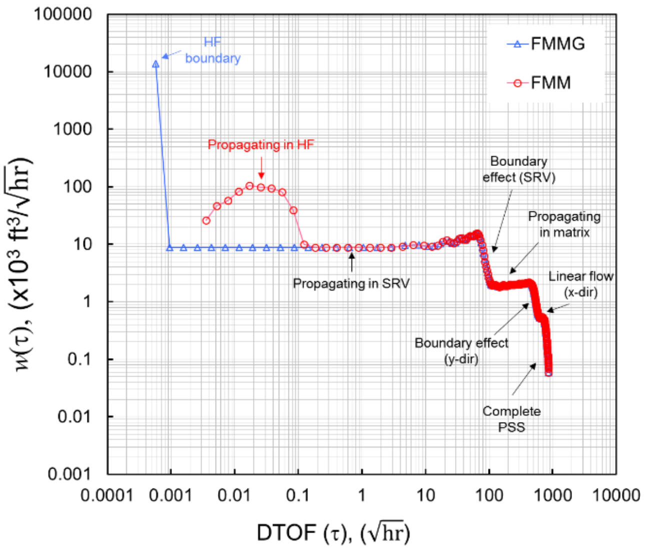

Figure 2.16 Comparison of the *w*(*τ*) function for the FMMG (blue) and the FMM (red) (reprinted with permission from Onishi et al., 2020)

Flow response comparisons are summarized in Figure 2.17. While solutions using the standard FMM shows deviations compared to the reference solution, good agreement was obtained between the reference solution and the FMMG solutions. Figure 2.18-20 show visual comparisons of the three different methods in terms of pressure, water saturation, and gas saturation at the end of the simulation period (1,000 days). In the 3D views, all of them show similar results; however, averaged profiles are obtained in the standard FMM in the 2D cross section views. Clearly, the FMMG approach captures the effect of gravity and multi-phase flow in the hydraulic fracture planes.

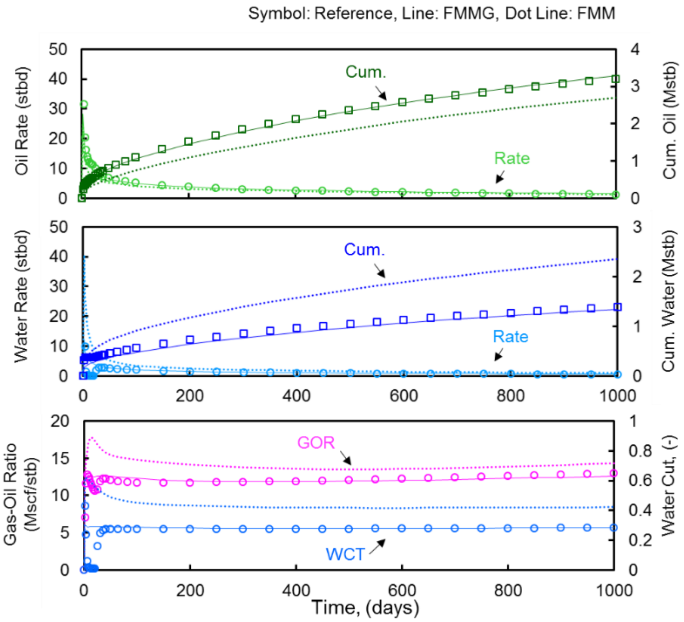

Figure 2.17 Flow response comparisons (reprinted with permission from Onishi et al., 2020)

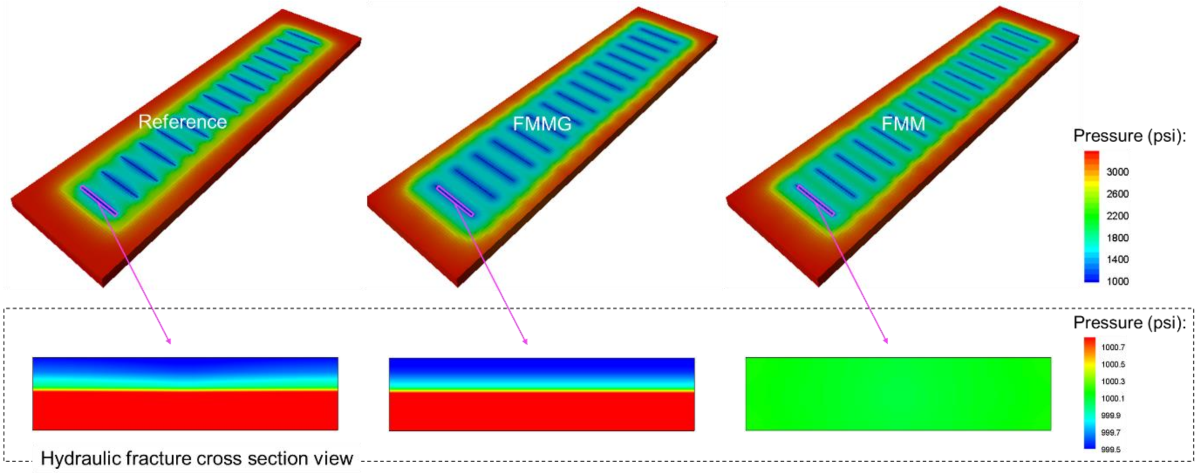

Figure 2.18 Pressure distribution from the reference solution (left), FMMG (middle), and FMM (right) at the end of simulation (1000 days) (reprinted with permission from Onishi et al., 2020)

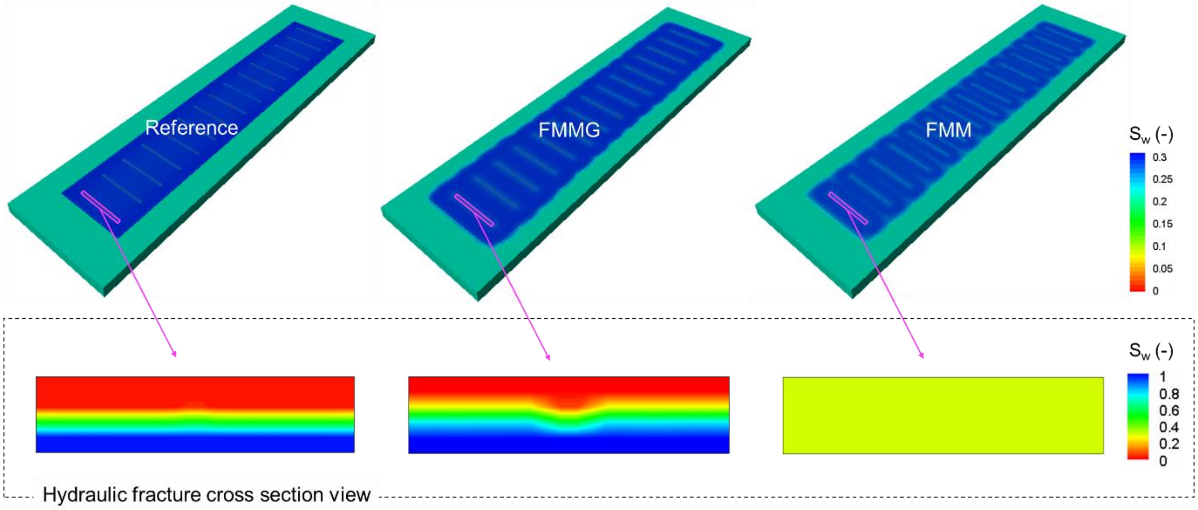

Figure 2.19 Water phase saturation from the reference solution (left), FMMG (middle), and FMM (right) at the end of simulation (1000 days) (reprinted with permission from Onishi et al., 2020)

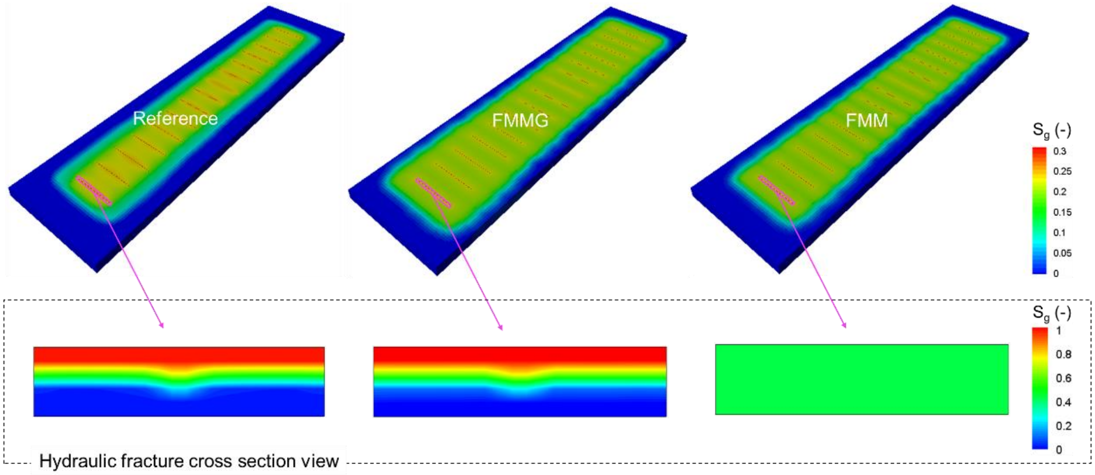

Figure 2.20 Gas phase saturation from the reference solution (left), FMMG (middle), and FMM (right) at the end of simulation (1000 days) (reprinted with permission from Onishi et al., 2020)

2.5.2 Field Application

Finally, we applied our modeling approach to a field scale example, a tight oil reservoir with typical reservoir properties in the Eagle Ford formation. The model size is

1200×6300×340(ft3) with 41×1267×46 (~2.4 million) grid discretization. Figure 2.21 shows the model structure and grid properties with matrix permeability ranging between 0.1-10 μD and matrix porosity between 0.5-6.0 %. The same fluid model and rock compaction tables from the synthetic example in the previous case are used. Average initial pressure is 3,300 psi (initially undersaturated) and average water saturation values of 0.3 and 0.8 are assigned to the matrix and hydraulic fracture planes. The model consists of a single horizontal well with 120 hydraulic fractures (4 clusters×30 stages) described by tartan gridding. The well produces fluids for 200 days with a varying oil production rate constraint. With the large number of gridblocks and multi-phase flow, this is a challenging application of FMM-based rapid reservoir simulation workflow.

The drainage volume propagation with time using the FMM and FMMG are shown in Figure 2.22. Again, different trends are obtained at early time due to the special treatment in the FMMG, and the subsequent trends are similar in the two approaches. This observation is consistent with the $w(\tau)$ diagnostic plot provided in Figure 2.23.

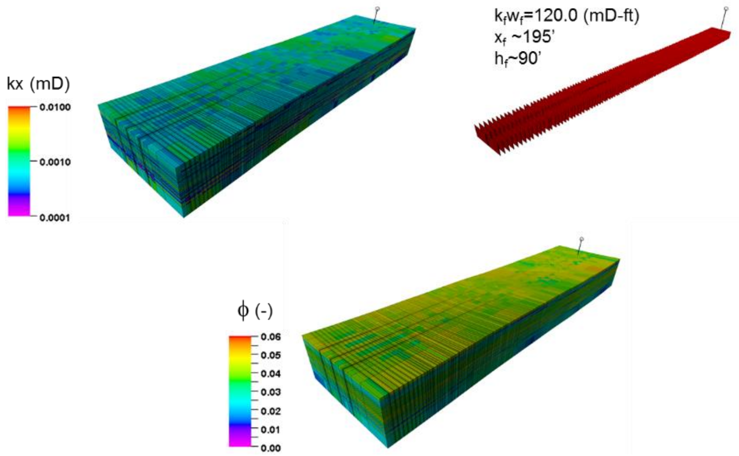

Figure 2.21 Grid permeability and hydraulic fracture properties (top), and grid porosity (bottom) (reprinted with permission from Onishi et al., 2020)

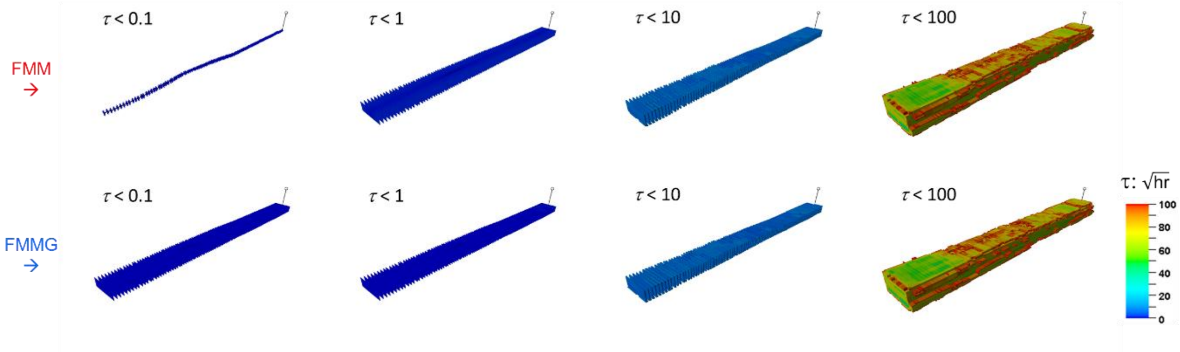

Figure 2.22 Drainage volume propagations with time: top row (FMM) and bottom row (FMMG) (reprinted with permission from Onishi et al., 2020)

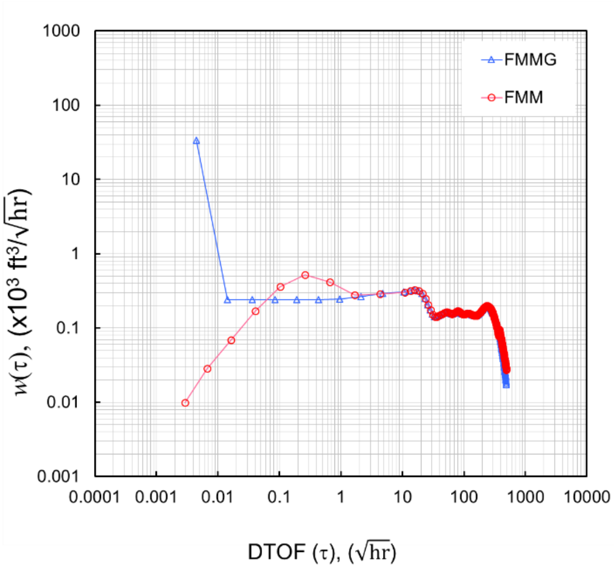

Figure 2.23 Comparison of the $w(\tau)$ function for the FMMG (blue) and the FMM (red) (reprinted with permission from Onishi et al., 2020)

Flow response comparisons are summarized in Figure 2.24. The FMMG captures the effects of gravity and multi-phase flow in the hydraulic fractures, resulting in good agreement with the reference solution, while the FMM solutions show deviations. However, the FMMG solutions degrade to some degree, which is likely due to the higher complexity of the model (>100 hydraulic fractures). Use of the surface area weighted averaged transmissibilities (Eq. (2.5)) is possibly the cause of the issue. A potential treatment to improve this could be extending the region where we use original gridblocks. That is, using the matrix gridblocks surrounding the hydraulic fracture planes in addition to the hydraulic fracture planes, and connecting surface area of the matrix gridblocks with the first 1-D DTOF gridblock via NNCs when we build a FMMG simulation model. Transmissibility calculations using this approach are likely to be less affected by the averaging effects as reservoir properties in the matrix are typically much less heterogeneous. Another possibility of the discrepancies is the no flow boundaries at the fracture inferences and outer boundaries that may cause reflections and transmissions of pressure waves, leading to increase or loss in pressure amplitude (Wang et al. 2018). Although beyond scope of this study, this can be improved by using an extended FMM approach considering additional pressure front arrivals (Huang et al. 2017).

CPU time comparison is provided in Figure 2.25. The FMM and FMMG approaches are found to be significantly more efficient than the reference case using the commercial simulator. The FMMG shows slightly more CPU time than the FMM approach because the FMMG approach solves for more unknowns (1D-grid along the DTOF + 2D hydraulic fracture planes) than the FMM approach (1D-grid along the DTOF). Nevertheless, the increment of CPU time in the FMMG approach is minimal. We recognize that the CPU of the FMM and FMMG mostly comes from pre-processing which includes solving the Eikonal equation (Eq. (2.1)), calculating 1-D transmissibilities, and

I/O. For the Eikonal solver, further speedup can be potentially obtained by, for example, parallelizing the workflow (Jeong and Whitaker 2007).

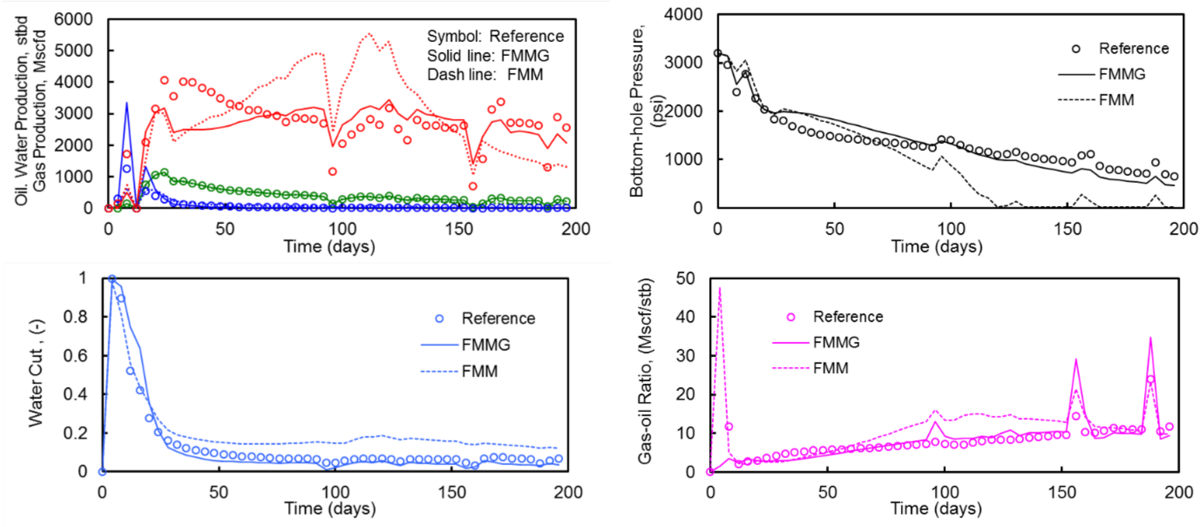

Figure 2.24 Flow response comparisons (Symbol: reference, dash line: FMM, and solid line: FMMG) (reprinted with permission from Onishi et al., 2020)

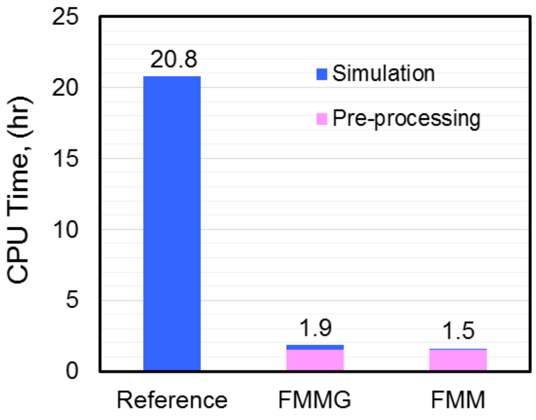

Figure 2.25 CPU time comparison (reprinted with permission from Onishi et al., 2020)

2.6 Conclusions

The FMM-based simulation approach accounting for gravity effects has been presented. We demonstrated the efficacy, utility and practical feasibility of our approach using synthetic and field-scale examples with realistic levels of complexity. From the observations made in this study, following conclusions are drawn:

- Our method treats hydraulic fractures and a matrix domain separately. While 3-D problems in a matrix domain are transformed into 1-D problems along the DTOF, original 2-D gridblocks are retained to represent the hydraulic fracture planes. Connections between the 1-D matrix domain and the hydraulic fractures are described by NNCs. These changes are relatively minor and can be easily implemented into an existing FMM-based rapid simulation workflow.
- We first tested our implementation using 2D examples without gravity to examine the NNC treatment. Good agreement was obtained between the reference solution, the FMM, and the FMMG, in homogeneous and heterogeneous examples, validating our transmissibility calculations.
- The proposed approach is applied to 3D synthetic and field scale examples. Our approach captures the effect of gravity in the hydraulic fracture plane which is vital for reliable prediction of the multiphase flow during unconventional reservoir developments, while retaining computational efficiency of rapid FMM-based simulation workflow.

CHAPTER III

COMPUTING PRESSURE FRONT PROPAGATION USING THE DIFFUSIVE TIME OF FLIGHT IN STRUCTURED AND UNSTRUCTURED GRID SYSTEMS VIA THE FAST MARCHING METHOD[‡]

3.1 Chapter Summary

Diffusive-time-of-flight (DTOF), representing the travel time of pressure front propagation, has found many applications in unconventional reservoir performance analysis. The computation of DTOF typically involves upwind finite difference of the Eikonal equation and solution using the fast-marching method (FMM). However, the application of the finite difference-based FMM to irregular grid systems remains a challenge. In this study, we present a novel and robust method for solving the Eikonal equation using finite volume discretization and the FMM.

The implementation is first validated with analytical solutions using isotropic and anisotropic models with homogeneous reservoir properties. Consistent DTOF distributions are obtained between the proposed approach and the analytical solutions.

[‡] Part of this chapter is reprinted with permission from "Hongquan, Chen, Tsubasa, Onishi, Jaeyoung, Park et al. 2020. Computing Pressure Front Propagation Using the Diffusive Time of Flight in Structured and Unstructured Grid Systems Via the Fast Marching Method. Proc., SPE Annual Technical Conference and Exhibition. https://doi.org/10.2118/201771-MS". Copyright 2020 Society of Petroleum Engineers. Further reproduction is prohibited without permission.

[‡] Part of this chapter is reprinted with permission from "Chen, Hongquan, Onishi, Tsubasa, Park, Jaeyoung et al. 2021. Computing Pressure Front Propagation Using the Diffusive-Time-of-Flight in Structured and Unstructured Grid Systems via the Fast-Marching Method. SPE Journal: 1-21". Copyright 2021 Society of Petroleum Engineers. Further reproduction is prohibited without permission.

Next, the implementation is applied to unconventional reservoirs with hydraulic and natural fractures. Our approach relies on cell volumes and connections (transmissibilities) rather than the grid geometry, and thus can be easily applied to complex grid systems. For illustrative purposes, we present applications of the proposed method to embedded discrete fracture models (EDFMs), dual-porosity dual-permeability models (DPDK), and unstructured perpendicular-bisectional (PEBI) grids with heterogeneous reservoir properties. Visualization of the DTOF provides flow diagnostics, such as evolution of the drainage volume of the wells and well interactions.

The novelty of the proposed approach is its broad applicability to arbitrary grid systems and ease of implementation in commercial reservoir simulators. This makes the approach well-suited for field applications with complex grid geometry and complex well architecture.

3.2 Introduction

Modeling unconventional reservoir developments has been an active area of research as a response to the significant amount of reserves in the U.S. (EIA 2021). Various numerical and analytical models incorporating relevant physics at varying fidelity levels have been proposed. Multiple continuum models (Warren and Root 1963, Kazemi, Merrill Jr, et al. 1976), unstructured discrete fracture models (Cipolla et al. 2011), multi-segment well (Du et al. 2016), and embedded discrete fracture models (EDFMs) (Li and Lee 2008) are some of the notable numerical models that have been proposed. In order to capture the complex non-linear descriptions, detailed spatial-temporal discretization is required to accurately represent multiphase flow in complex fracture networks and high contrast systems. Therefore, the numerical models tend to be computationally expensive. As a result, simple analytical models, such as decline curve analysis (Arps 1945, Fetkovich 1980) and rate transient analysis (Fetkovich et al. 1987, Blasingame et al. 1991, Song and Ehlig-Economides 2011) have become popular. Although conceptually simple and computationally efficient, these analytical models are typically dependent on certain assumptions including homogeneous reservoir properties, planar fractures, and single-phase flow. Therefore, capturing more detailed physics still remains a challenge in these simplified models.

In an effort to overcome the challenges in the existing modeling approaches for unconventional reservoirs, applications of an asymptotic approach to the diffusivity equation have been proposed (Xie et al. 2015). The use of an asymptotic solution to the diffusivity equation leads to the Eikonal equation which governs the propagation of a pressure front propagation and generalizes the depth of investigation (Lee 1982) for heterogeneous reservoirs. Vasco et al. (2000) and Kulkarni et al. (2001) presented trajectory-based solutions to the Eikonal equation. Specifically, the trajectories are approximated by ray path (Vasco et al. 2000) or by convective streamlines (Kulkarni et al. 2001), then the phase or diffusive time-of-flight (DTOF) are obtained by calculating the line integral along the trajectories. An alternative approach to computing the DTOF is the fast marching method (FMM), a class of front-tracking algorithm, which does not require explicit construction of the trajectories and can solve the Eikonal equation efficiently without iterations (Sethian 1999).

The DTOF represents the propagation time of the peak pressure disturbance caused by an impulse source. The propagation distance is known as the depth of investigation and the associated volume defined as drainage volume which is the region of the reservoir contributing to the production of the well at any given time. The DTOF and drainage volume are quite useful quantities and have found many applications in modeling unconventional reservoirs. For example, we can visualize the drainage volume evolution by thresholding the propagation time at selected time intervals. This offers visual appeal and physically intuitive representation of the complex interaction between hydraulic and natural fractures and can be utilized in order to optimize development plans, such as the number of hydraulic fracturing stages and their spacing (Vasco and Datta-Gupta 2016). Besides the visualizations, the DTOF can be used as a spatial coordinate in flow simulation. Specifically, we can transform original 2-D or 3-D problems into equivalent 1-D problems along the DTOF (Zhang et al. 2016). This leads to substantial savings in computational time in the numerical simulation while retaining accuracy. The original work (Zhang et al. 2016) focused on modeling shale-gas reservoirs. Later, the approach has been extended to account for more complex problems, such as multiphase and multicomponent flow (Fujita et al. 2016, Iino, Onishi, et al. 2020), non-isothermal flow (Cui et al. 2016), and gravity (Onishi, Iino, et al. 2019), as well as complex grid systems including multiple continuum models (Fujita et al. 2016), unstructured discrete fracture models (Yang et al. 2017), and EDFMs (Xue, Yang, et al. 2019a). Yang et al. (2015) and Xue, Yang, Park, et al. (2019) proposed another class of approach using the concept of DTOF for production data analysis. In their approach, the DTOF and $w(\tau)$ function which is defined as derivative of drainage pore volume with respect to the DTOF are obtained from the production data, instead of solving the Eikonal equation using the FMM. The data-driven diagnostic plots using the DTOF and $w(\tau)$ function offer a simple and intuitive understanding of the transient-drainage volume and fracture conductivity. In this study, we focus on solving the Eikonal equation using the FMM.

The success of the DTOF-based approaches is contingent on the FMM. While well established for reservoir models with structured grid systems, the FMM is less straightforward in more-general grid systems. For example, special treatments, such as sub-gridding are required to handle unstructured grids (Yang et al. 2017), local grid refinements, and EDFMs (Xue, Yang, et al. 2019a). Such algorithms are typically less efficient and difficult to generalize. In addition to the discrete fracture models, dual-porosity dual-permeability (DPDK) models where both matrix and fracture contribute to the flow are also widely used for modeling unconventional reservoirs (Hui et al. 2019, Thomas et al. 2019, Yang et al. 2018, Kumar et al. 2019). Although the FMM applications are successful in the dual-porosity single-permeability (DPSK) (Zhang et al. 2016) and triple-porosity single-permeability (TPSK) systems (Fujita et al. 2016), explicit tracking of the pressure front in the two interacting continua in DPDK systems is challenging.

It is worth mentioning that we have seen similar challenges in the context of flow diagnostics for conventional reservoirs on the basis of two key parameters, streamlines and convective time-of-flight, defined as the travel time of neural tracer influenced by a defined velocity field (Datta-Gupta and King 2007) along the streamlines. The streamlines and convective time-of-flight have been utilized in a number of applications, including, but not limited to visualization (Olalotiti-Lawal et al. 2019) forward simulation (Batycky et al. 1997, Jessen and Orr Jr 2002, Cheng et al. 2006, Iino and Arihara 2007, Tanaka et al. 2014, Olalotiti-Lawal, Tanaka, et al. 2020), data integration (Vasco et al. 1998, He et al. 2002, Cheng et al. 2005, Bhark et al. 2012, Tanaka et al. 2015, Kam and Datta-Gupta 2016, Olalotiti-Lawal et al. 2019, Chen, Yang, et al. 2020, Liu et al. 2020), and optimization (Thiele and Batycky 2003, Alhuthali et al. 2007, Tanaka et al. 2017, Tanaka et al. 2020). The streamline-based methods are quite useful but require explicit streamline tracing (Pollock 1988). Although possible, tracing streamlines is difficult and less efficient in the irregular grid systems (Prevost et al. 2001, Matringe and Juanes 2005, Jimenez et al. 2010, Zhang et al. 2012, Chen, Onishi, et al. 2020) like the front tracking in the FMM discussed earlier. As a result, an alternative finite volume based approach has been proposed by Natvig et al. (2007). In their approach, a single matrix solve generates the convective time-of-flight and numerical tracer concentrations on finite-volume grids. These information can be used in the applications that have been done using streamlines in a more general manner with the finite volume framework (Shahvali et al. 2012). It may suffer from numerical dispersion effects which are tied with any grid-based methods (Lantz 1971), unlike the streamline-based methods which offer sub-grid resolutions, hence less numerical artifacts. The effects of numerical dispersion can be significant if there are high concentration of wells in a small region with relatively coarsened grid resolution. Nevertheless, the finite volume based flow diagnostics approach is widely accepted in industry and has found many practical applications (Lie et al. 2015, Møyner et al. 2015, Olalotiti-Lawal, Hetz, et al. 2020) due to its utility and compatibility with the existing reservoir simulators. The majority of commercial reservoir simulators use finite volume methods, and many techniques to address the numerical artifacts already exist. Such techniques can be readily incorporated in the finite volume based flow diagnostics approach.

This study is inspired by the previous works on the finite volume based flow diagnostics method for conventional reservoirs. In this study, we present a finite volume based approach for solving the Eikonal equation using the FMM which is designed for diffusive processes, typical characteristics in tight unconventional reservoirs. We put forth a robust method that circumvents the need of the special treatments, such as sub-gridding (Xue, Yang, et al. 2019a), for solving the Eikonal equation in irregular grid systems by introducing a finite volume discretization of the Eikonal equation. The discrete systems can be efficiently solved by the FMM. As presented in the following sections, the proposed method is general and applicable to arbitrary finite-volume grid systems in reservoir models, including, but not limited to single porosity models, DPDK models, EDFM, and unstructured grids.

The following sections are organized as follows. First, we revisit the concept of pressure front propagation and the asymptotic approach. We then provide a description of the proposed finite volume based method. The implementation is validated by comparing with a series of analytical and numerical examples. Next, we present applications of our approach to field scale examples to illustrate the robustness and versatility of the approach. Our focus in this study is flow diagnostics in unconventional reservoirs using the DTOF and visualization of the drainage volume. Although further applications, such as the rapid

1-D flow simulation utilizing the DTOF as a 1-D spatial coordinate (Zhang et al. 2016, Iino et al. 2020), can be readily done using the DTOF and drainage pore volume, we leave them as future work.

3.3 Methods

3.3.1 Pressure Front Propagation

This section describes details of the proposed approach. The notations in this work follow the convention as follows:

- A vector is treated as a column vector by default, and a row vector is denoted by transpose notation *T*.
- Divergence of a vector **v** is interpreted as the "transpose" of the gradient operator multiplied by the column vector, that is, $\nabla \cdot \mathbf{v}$ is expressed as $\nabla^T \mathbf{v}$.

The single-phase fluid flow in porous media is governed by the diffusion equation,

$$\nabla^T \left(\frac{\mathbf{k}}{\mu} \nabla (p - \rho g z) \right) = \phi c_t \frac{\partial p}{\partial t},$$

$$\mathbf{k} = \begin{bmatrix} k_x & & \\ & k_y & \\ & & k_z \end{bmatrix}, \nabla = \begin{bmatrix} \partial_x \\ \partial_y \\ \partial_z \end{bmatrix}, \nabla^T = \begin{bmatrix} \partial_x & \partial_y & \partial_z \end{bmatrix} \tag{3.1}$$

where p is pressure, $\mathbf{k}$ is permeability tensor, ϕ is porosity, μ is fluid viscosity, ρ is fluid density, c_t is total compressibility, g is the gravity acceleration, and z is the depth. Using Fourier transform of the diffusion equation and a high-frequency asymptotic approach, we can derive the Eikonal equation that governs the pressure front propagation in the subsurface (Vasco et al. 2000),

$$\nabla^T \tau\, \mathbf{k}\, \nabla \tau = \phi \mu c_t \tag{3.2}$$

where τ is the DTOF representing the propagation time. In previous studies, the upwind finite difference method has been used to discretize the Eikonal equation into a quadratic form, which is subsequently solved by the FMM.

$$\sum_{l}^{\pm x, \pm y, \pm z} \max(D_{ijk}^{l} \tau, 0)^2 = \frac{1}{\phi \mu c_t} \tag{3.3}$$

where the finite difference operator D for $\pm x$ directions can be written as and $D_{ijk}^{+x} \tau = \left(\tau_{i+1,j,k} - \tau_{i,j,k} \right) / \Delta x$ and $D_{ijk}^{-x} \tau = \left(\tau_{i,j,k} - \tau_{i-1,j,k} \right) / \Delta x$. Similar formulas hold for $\pm y$ and $\pm z$ directions. The finite-difference-based solution has been extended to unstructured grids (Yang et al. 2017), local grid refinements, and EDFM (Xue, Yang, et al. 2019a). However, such algorithms are strictly dependent on grid geometry and difficult to generalize for complex reservoir architecture and stratigraphy, which are typically modeled by gridblock volumes and connections. This study formulates the finite volume form of the Eikonal equation and implements its corresponding FMM solution so as to lay the foundation for the DTOF-based applications on general finite-volume grid systems.

3.3.2 The Finite-volume Formulation

The goal here is to enable the calculation of DTOF based on properties of cell volumes and cell connections. The calculation of cell connections usually involves surface integrals converted from volume integrals in the partial differential equation containing divergence terms. Hence, the strategy is to expand the Eikonal equation into terms with divergence operator. Using product rule, the left-hand side of Eq. (3.2) is first converted into two divergence terms.

$$\nabla^T \tau\, \mathbf{k}\, \nabla \tau = \nabla^T \left(\tau\, \mathbf{k}\, \nabla \tau\right) - \tau\, \nabla^T \left(\mathbf{k}\, \nabla \tau\right) \tag{3.4}$$

The partial differential equation is then integrated within a finite volume (Figure 3.1a), shown as follows,

$$\iiint_V \left(\nabla^T \left(\tau\, \mathbf{k}\, \nabla \tau\right) - \tau\, \nabla^T \left(\mathbf{k}\, \nabla \tau\right)\right) dV = \iiint_V \left(\phi \mu c_t\right) dV \tag{3.5}$$

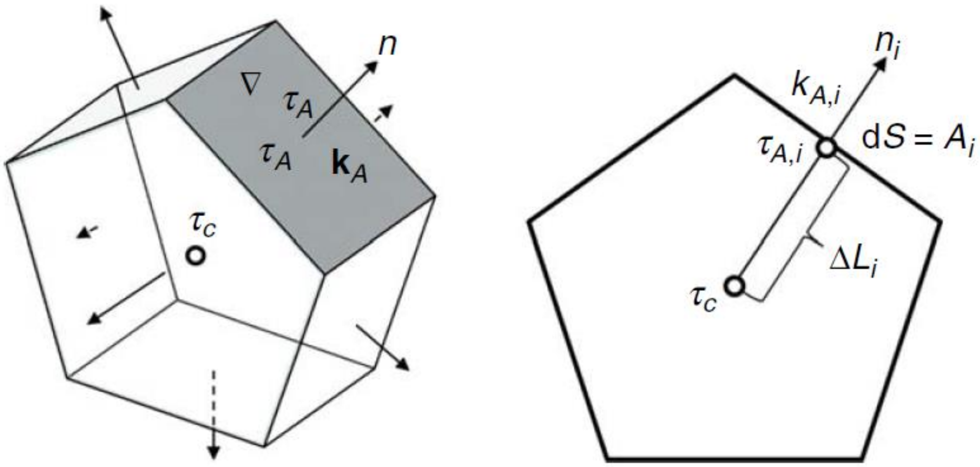

Figure 3.1 Illustration of the geometries for the finite-volume derivation: (left) a volume *V* bounded by the surface *S* with the surface normal *n*, and (right) discretization of a polyhedron in terms of connections (reprinted with permission from Chen et al., 2021).

The volume integral on the left-hand side of Eq. (3.5) can be transformed into surface integrals (Eq. (3.6)) using the divergence theorem. This step aims to associate the variation of DTOF with flow properties on the interface of two volume elements.

$$
\begin{aligned}
&\iiint_V \left(\nabla^T \left(\tau\, \mathbf{k}\, \nabla \tau \right) - \tau\, \nabla^T \left(\mathbf{k}\, \nabla \tau \right) \right) dV \\
&= \iiint_V \nabla^T \left(\tau\, \mathbf{k}\, \nabla \tau \right) dV - \iiint_V \tau\, \nabla^T \left(\mathbf{k}\, \nabla \tau \right) dV \\
&\approx \iiint_V \nabla^T \left(\tau\, \mathbf{k}\, \nabla \tau \right) dV - \tau_c \iiint_V \nabla^T \left(\mathbf{k}\, \nabla \tau \right) dV \\
&= \iint_S \left(\tau\, \mathbf{k}\, \nabla \tau \right)^T \mathbf{n}\, dS - \tau_c \iint_S \left(\mathbf{k}\, \nabla \tau \right)^T \mathbf{n}\, dS
\end{aligned}
\tag{3.6}
$$

Eq. (3.6) shows the detailed steps to get the surface integrals, in which the area of surface element is *dS* and its normal direction is **n**. Here, we also use DTOF at the cell center τ_c as a representative DTOF for the volume integration containing the second divergence term. The integral form of the Eikonal equation is finally expressed as follows,

$$
\iint_S \left(\tau\, \mathbf{k}\, \nabla \tau \right)^T \mathbf{n}\, dS - \tau_c \iint_S \left(\mathbf{k}\, \nabla \tau \right)^T \mathbf{n}\, dS = \iiint_V \left(\phi \mu c_t \right) dV \tag{3.7}
$$

Each term in Eq. (3.7) needs to be discretized (Figure 3.1b) to get the form of algebraic equations. Eq. (3.8) gives the discretization of the first term. The contact area of the interface with respect to connection *i* is A_i; $\tau_{A,i}$, $\mathbf{k}_{A,i}$, and $\nabla \tau_{A,i}$ are representative values on the surface element, and ΔL_i is the distance from block center to that interface. Also, ($\nabla^T \tau_{A,i} \mathbf{k}_{A,i} \mathbf{n}_i$), the product of gradient of DTOF and permeability tensor in the normal direction of the interface, is approximated by the finite difference term ($\tau_{A,i}$- τ_c)/ΔL_i and the directional permeability $k_{A,i}$, which finally leads to the transmissibility of the corresponding connection $T_{A,i}$ defined as $k_{A,i} A_i / \Delta L_i$. Particularly, the connection transmissibilities in our implementation are the standard ones obtained from any reservoir simulator.

$$
\begin{aligned}
&\iint_S \left(\tau\, \mathbf{k}\, \nabla \tau\right)^T \mathbf{n}\, dS \\
&\approx \sum_i \left(\tau_{A,i} \left(\mathbf{k}_{A,i}\, \nabla \tau_{A,i}\right)^T \mathbf{n}_i A_i\right) \\
&= \sum_i \left(\tau_{A,i} \left(\nabla^T \tau_{A,i}\, \mathbf{k}_{A,i}\, \mathbf{n}_i\right) \cdot A_i\right) \\
&\approx \sum_i \left(\tau_{A,i} k_{A,i} \frac{\tau_{A,i} - \tau_c}{\Delta L_i} A_i\right) \\
&= \sum_i \left(\tau_{A,i} \left(\tau_{A,i} - \tau_c\right) \frac{k_{A,i} A_i}{\Delta L_i}\right) = \sum_i \left(\tau_{A,i} \left(\tau_{A,i} - \tau_c\right) T_{A,i}\right)
\end{aligned}
\tag{3.8}
$$

Similarly, Eqs. (3.9) and (3.10) give the discretization of the second and the third terms in Eq. (3.7), respectively.

$$\tau_c \iint_S \left(\mathbf{k}\, \nabla \tau\right)^T \mathbf{n}\, dS = \tau_c \sum_i \left(\left(\tau_{A,i} - \tau_c\right) T_{A,i}\right) \tag{3.9}$$

$$\iiint_V \left(\phi \mu c_t\right) dV = V_p \mu c_t \tag{3.10}$$

Where, V_p is the pore volume of the gridblock. Substituting Eqs. (3.8) - (3.10) into Eq. (3.7), we get the following expression,

$$\sum_i \left(\left(\tau_{A,i} - \tau_c\right)^2 T_{A,i}\right) = V_p \mu c_t \tag{3.11}$$

For the two gridblocks in a connection, the one with smaller DTOF is called the upstream gridblock. The single-point-upstream weighting scheme is necessary to formulate the FMM to solve this problem. Adopting upstream gridblock DTOF τ_i to replace the surface DTOF $\tau_{A,i}$ for each connection, we can get the finite volume form of the Eikonal equation.

$$\sum_i^{connections} \left(\max\left(\tau_c - \tau_i, 0\right)^2 T_{A,i}\right) = V_p \mu c_t \tag{3.12}$$

Accounting for the upstream connections only, we get the following final form,

$$\sum_{i}^{\substack{\text{upstream}\\ \text{connections}}} \left(\left(\tau_c - \tau_i\right)^2 T_{A,i} \right) = V_p \mu c_t \tag{3.13}$$

Figure 3.2 gives an example of the surface DTOF interpolation based on the single-point-upstream weighting scheme. Based on the scenario (τ_1, $\tau_2 < \tau_c < \tau_3$, τ_4, τ_5), Connections 1 and 2 are upstream connections where $\tau_{A,i} - \tau_c = \tau_i - \tau_c$, and Connections 3, 4, and 5 are downstream connections where $\tau_{A,i} - \tau_c = 0$.

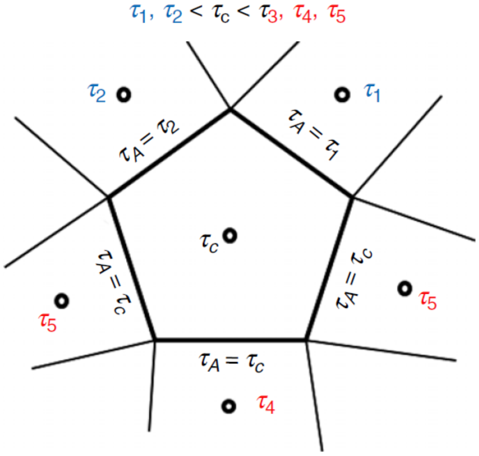

Figure 3.2 Illustration of the upstream scheme for the surface DTOF in a given scenario where τ_1, $\tau_2 < \tau_c < \tau_3$, τ_4, τ_5 (reprinted with permission from Chen et al., 2021)

3.3.3 The Fast-Marching Method

From Eq. (3.13), we can see that the DTOF of a gridblock only depends on its upstream gridblocks, and the calculation of the DTOF involves solving a local quadratic equation. This enables the solution of s to be constructed in an orderly fashion from smaller values to larger values. Such strategy is developed as a numerical algorithm called the FMM by Sethian (1999). Though the FMM is initially developed on the nodes in the finite difference scheme, it can also be extended to the gridblocks in the finite-volume scheme.

The calculation or update of the DTOF values by FMM contains only upwind neighbors and strictly follows the causality of the pressure propagation process. During the progression of the FMM, gridblocks are dynamically labeled as far (not yet visited), considered (visited and value tentatively assigned), and accepted (visited and value permanently assigned). The basic steps are as follows,

1. To begin with, assign every assign every gridblock x_i an infinite DTOF value, $\tau_i = +\infty$, and label them as 'far'; assign gridblocks where the pressure front propagation starts their initial values (usually zero), $\tau_i = 0$, and label them as 'accepted' (Figure 3.3a).
2. For every far gridblock x_i connected to the accepted ones, use Eq. (3.13) to calculate a new DTOF value $\tilde{\tau}$ and label it as 'considered' (Figure 3.3b).
3. Let $\tilde{x}$ be the one with smallest DTOF value among all 'considered' gridblocks, and label $\tilde{x}$ as 'accepted' (Figure 3.3c).
4. For every x_i connected to $\tilde{x}$, if x_i is either 'considered' or 'far', calculate a new DTOF value $\tilde{\tau}$ using Eq. (3.13). If $\tilde{\tau} < \tau_i$, set $\tau_i = \tilde{\tau}$. If x_i is labeled as 'far', set it as 'considered' (Figure 3.3d).
5. If there exists a 'considered' node, return to Step 3. Otherwise, terminate.

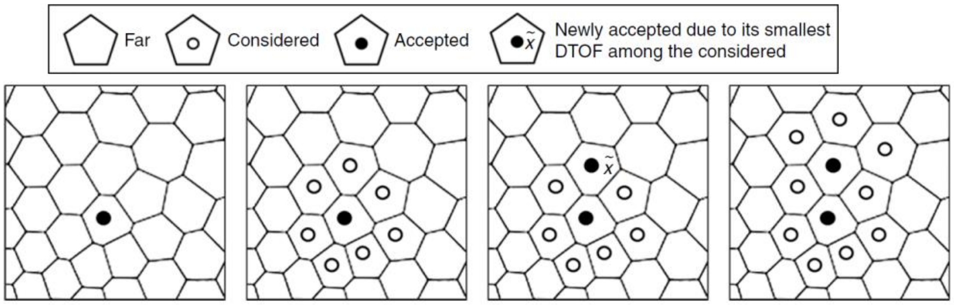

(a) (b) (c) (d)

Figure 3.3 Illustration of the FMM on finite volume gridblocks (reprinted with permission from Chen et al., 2021)

There are significant differences between the implementation of this finite-volume FMM and previous variations of finite-difference FMM (Sethian 1999, Yang et al. 2017, Li 2018, Xue, Yang, et al. 2019a). The finite-difference-FMM variations propose a sub-grid resolution in which nodes of interest are not only placed in the center but also on the boundary of each gridblock following a five-stencil or nine-stencil scheme in 2D (can be extended to nine-stencil or 27-stencil scheme in 3D), and DTOF values need to be calculated or updated based on each triangular element (Figure 3.4). The connections and causalities between nodes of interest in the finite-difference FMM depend on the grid geometry and property features, such as anisotropy and heterogeneity, leading to a situation in which DTOF gradients may not be consistent with model characteristics. The causality issues have been discussed in several previous papers (Sethian and Vladimirsky 2001, Zhang et al. 2013). In this finite-volume FMM, only one DTOF value for each gridblock is calculated, and no geometry calculation is involved because the grid geometry and properties are presented by transmissibilities and pore volumes obtained from finite-volume simulators. Although the finite-volume FMM does not use the sub-grid resolution designed for the causality issue, its simplicity and robustness can extend the FMM application to much more complex grids, and its universal usage of the transmissibility and the pore volume inherently guarantees a better consistency between the FMM diagnostics and simulation results.

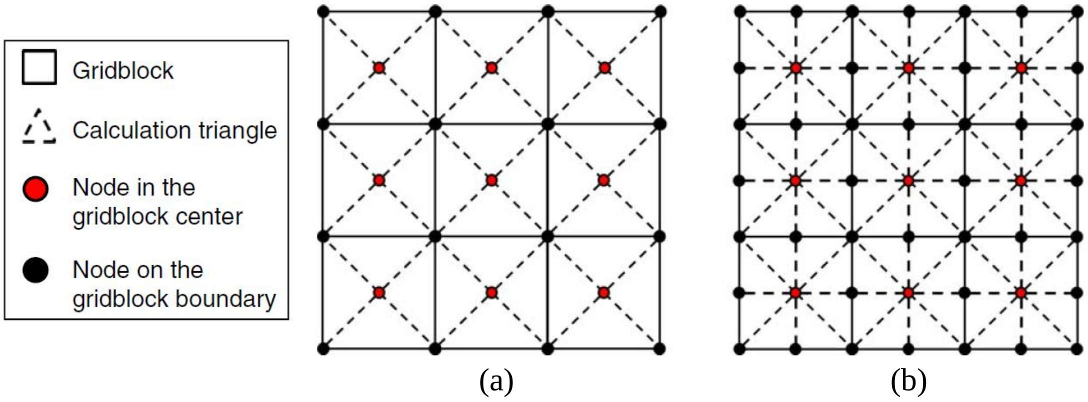

Figure 3.4 2D sub-grid discretization schemes in a finite-difference-FMM implementation: (a) five-stencil scheme and (b) nine-stencil scheme (reprinted with permission from Chen et al., 2021)

3.4 Validation

In this section, we validate our implementation using simple 2D homogeneous reservoirs, for which we can analytically calculate the DTOF, $\tau(\vec{x})$, using the path of the fastest pressure propagation back to the source points (i.e., well cell), where $\tau = 0$. Specifically, $\tau = r/\sqrt{\alpha}$, where r is distance from the source point, and α is the diffusivity ($=k/\mu\phi c_t$). We will show comparisons between the analytical solution and the numerical solution using our implementation, in terms of the DTOF distribution, cumulative drainage pore volume along τ, and the $w(\tau)$ diagnostic plot which is the derivative of the drainage pore volume with respect to DTOF (Zhang et al. 2016).

3.4.1 Example 1: 2D Homogeneous, Isotropic Case

The first example comprises of a homogeneous square domain of length 1.0 (*ft*). The grid resolution is 501×501×1. The other grid properties are summarized in Figure

3.5a. The fluid viscosity is 1.0 (*cp*), and the total compressibility is 2.0e-6 (psi^{-1}). The model consists of a single production well in the center of the domain.

A comparison of the DTOF is shown in Figure 3.5b-c. The DTOF using our approach shows good agreement with the analytical solution. In addition to the visual comparison, we conducted a quantitative comparison using the relative error of the DTOF over the domain,

$$relative\ error = \sum_{i=1}^{N}\left(\tau_a^i - \tau_n^i\right)^2 \Big/ \sum_{i=1}^{N}\tau_a^{i\,2} \tag{3.14}$$

where, N is the number of gridblocks, τ_a^i and τ_n^i denote the DTOF at gridblock i using the analytical solution and the numerical solution. In this example, we obtained the relative error = 3.56e-5.

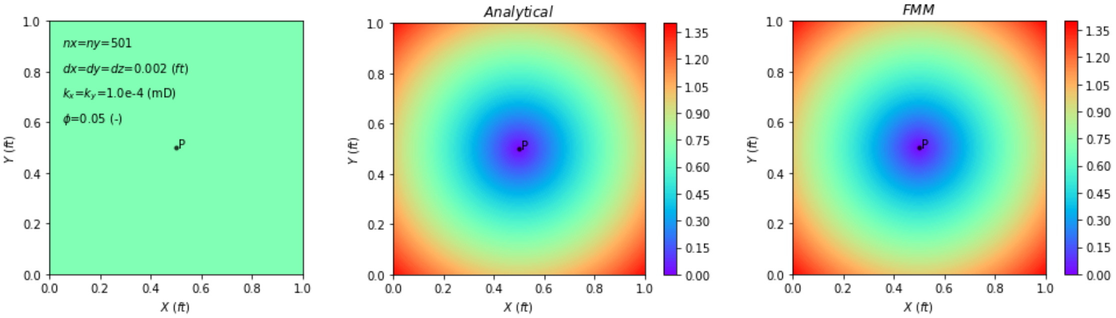

(a) (b) (c)

Figure 3.5 Homogeneous and isotropic case: (a) model domain and grid properties, (b) analytical DTOF ($\sqrt{hr}$), and (c) FMM-based DTOF ($\sqrt{hr}$) (reprinted with permission from Chen et al., 2021).

Furthermore, comparisons of cumulative drainage pore volume, $V_p(\tau)$, and the $w(\tau)$ diagnostic plot are shown in Figure 3.6. Here, $V_p(\tau)$ is sum of pore volumes within gridblocks whose τ values are smaller than τ of interest (x-axis in Figure 3.6a), whereas, the $w(\tau)$ function is defined as $dV_p(\tau)/d\tau$ and represents surface area of the pressure front propagation. In the plots in Figure 3.6, our approach shows excellent agreement with the analytical solution. The $w(\tau)$ diagnostic plot (Figure 3.6b) is useful for flow regime identification. At early time, the $w(\tau)$ shows a unit slope, indicating radial flow regime. Later, the pressure front reaches the reservoir boundary, and $V_p(\tau)$ no longer increases. As a result, we obtain a sharp drop in the $w(\tau)$ which corresponds to boundary dominated pseudo-steady state (PSS) flow. For more detailed discussions on the $w(\tau)$ diagnostic plots, the reader is referred to Xue, Yang, Park, et al. (2019).

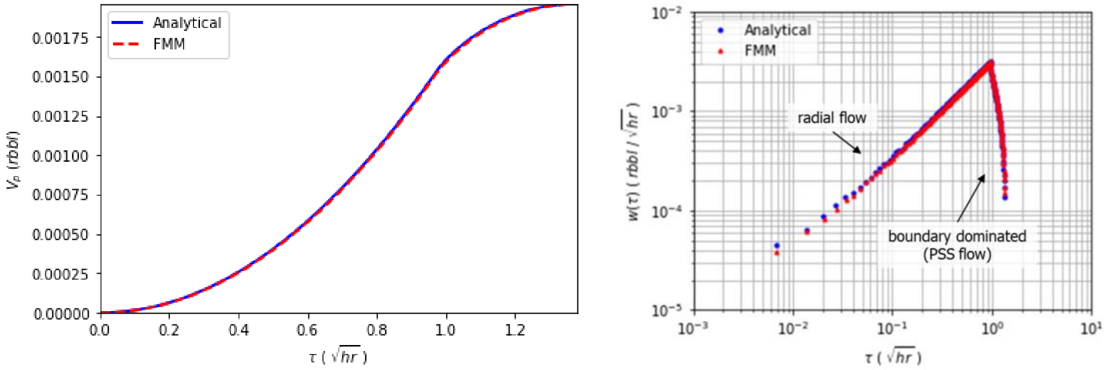

(a) (b)

Figure 3.6 Diagnostic plots comparing the analytical solution and the FMM approach based on the homogeneous and isotropic case: (a) $V_p(\tau)$ and (b) $w(\tau)$ (reprinted with permission from Chen et al., 2021)

3.4.2 Example 2: 2D Homogeneous, Anisotropic Case

We repeated the same exercise using a case involving permeability anisotropy (k_x/k_y=5). The other settings are same as the example 1. The permeability anisotropy needs to be considered in the analytical solution as shown below.

$$\tau = \frac{r}{\sqrt{\alpha}}, \text{where } r = \sqrt{\left(k_y / k_x\right)\left(x - x_{source}\right)^2 + \left(y - y_{source}\right)^2} \tag{3.15}$$

A visual comparison of the DTOF, and the $V_p(\tau)$ and $w(\tau)$ diagnostic plots are provided in Figure 3.7b-c, and Figure 3.8, respectively. As expected, the DTOF maps are elongated due to the anisotropy. Another interesting observation here is that the $w(\tau)$ function drops twice (Figure 3.8b). This is because, as seen in Figure 3.7, the pressure front first reaches the horizontal boundary. After that, the $V_p(\tau)$ still keeps increasing until the front reaches the vertical boundary. As a result, the first $w(\tau)$ drop is not as sharp as the second drop since the $V_p(\tau)$ still increases after the first boundary effect. Finally, the front arrives at the vertical boundary and $w(\tau)$ shows a sharp drop.

Again, we obtained excellent agreement between the FMM approach and the analytical solution, validating our implementation for scenarios with permeability anisotropy.

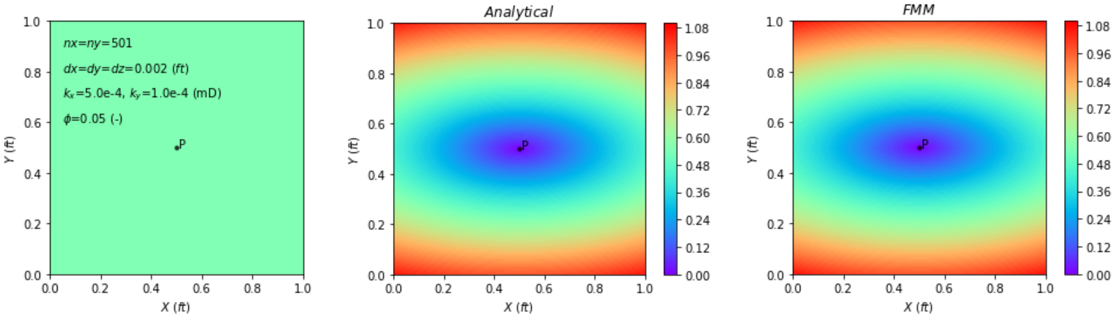

(a) (b) (c)

Figure 3.7 Homogeneous and anisotropic case: (a) model domain and grid properties, (b) analytical DTOF ($\sqrt{hr}$), and (c) FMM-based DTOF ($\sqrt{hr}$). The relative error is 2.06e-5 (reprinted with permission from Chen et al., 2021).

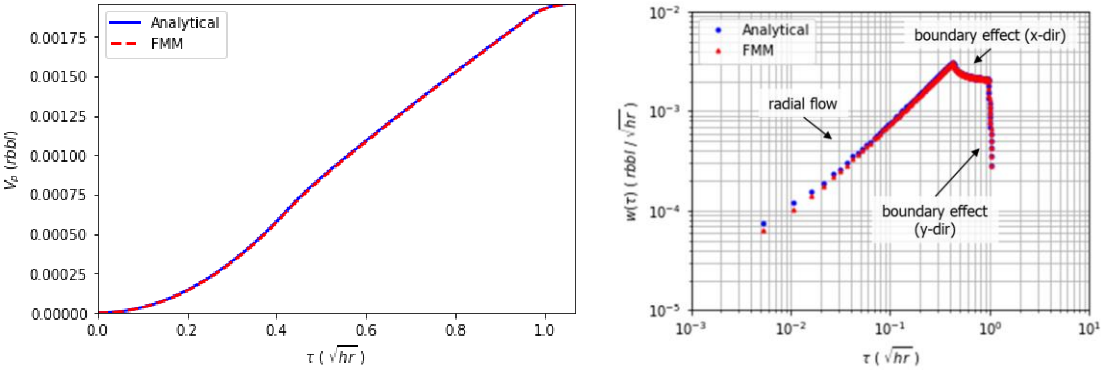

(a) (b)

Figure 3.8 Diagnostic plots comparing the analytical solution and the FMM approach based on the homogeneous and anisotropic case: (a) $V_p(\tau)$ and (b) $w(\tau)$ (reprinted with permission from Chen et al., 2021)

3.4.3 Grid Resolution Sensitivity

In this section, we investigate sensitivity of grid resolution. While a small domain size and fine scale discretization are used for validation purposes in the previous section, here we use a larger domain size and different grid resolutions to investigate the accuracy of our numerical approach in more realistic settings. In this exercise, again we consider homogeneous reservoirs, isotropic and anisotropic permeabilities ($k_x/k_y=5$), and the domain size of the case is 2,430×2,430×10 (ft^3). We consider 3 different discretization schemes, 243×243, 81×81, and 27×27. The other reservoir properties are the same as the examples in the previous section. Visual comparisons of the DTOF, and the $V_p(\tau)$ are displayed in Figure 3.9 and Figure 3.10. As expected, as the grid resolution is coarsened, the difference between analytical and numerical methods becomes more evident. For instance, the $V_p(\tau)$ calculations using coarser grids show deviations compared to the analytical solution in both isotropic and anisotropic cases (Figure 3.10), whereas, the solutions using the fine scale gridding converges to the reference. As in any numerical simulation study, it is recommended to carry out a grid resolution sensitivity to understand its impact on the solution.

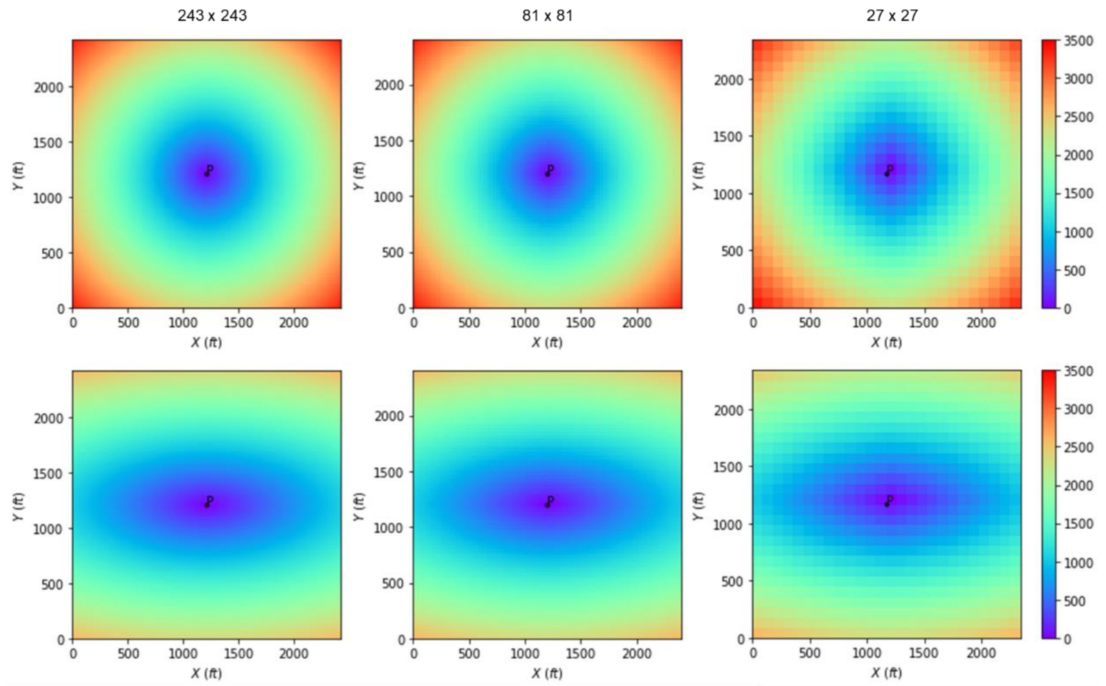

Figure 3.9 Comparisons of the map of DTOF ($\sqrt{hr}$) using different grid resolutions. Top: 2D homogeneous and isotropic cases, and bottom: 2D anisotropic cases (reprinted with permission from Chen et al., 2021)

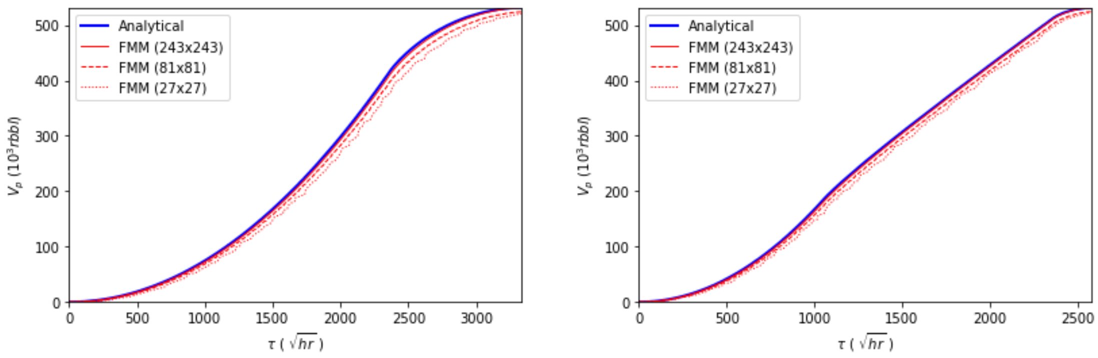

(a)

(b)

Figure 3.10 Comparison of the $V_p(\tau)$ using different grid resolutions for (a) 2D homogeneous and isotropic cases, and (b) for 2D anisotropic cases (reprinted with permission from Chen et al., 2021)

3.5 Applications

In this section, we discuss applications of our approach to the DPDK models, EDFM, and unstructured grids. In each case, we present both simplified and field-scale examples to demonstrate the underlying concepts and the practical feasibility of our approach.

3.5.1 Dual-Porosity Dual-Permeability Models

Dual-porosity models are often used for modeling fractured reservoirs involving different flow mechanisms in fractures and rock matrix (Figure 3.11). In the dual-porosity single-permeability (DPSK) model, the reservoir is discretized into two interacting continua, matrix and fracture, assuming that the majority of flow occurs in the fracture domain and matrix acts as source/sink. In contrast, both matrix and fracture domains are sufficiently conductive and contribute to flow in dual-porosity dual-permeability (DPDK) systems. The interactions between the two continua can be described by the transfer transmissibility (Kazemi, Merrill Jr, et al. 1976) which are used together with the transmissibilities within each of the domains during the pressure front tracking in our finite volume based approach.

This work presents, for the first time, applications of the FMM and concept of the DTOF to DPDK systems. We first present detailed numerical experiments and discussions and then a field-scale example.

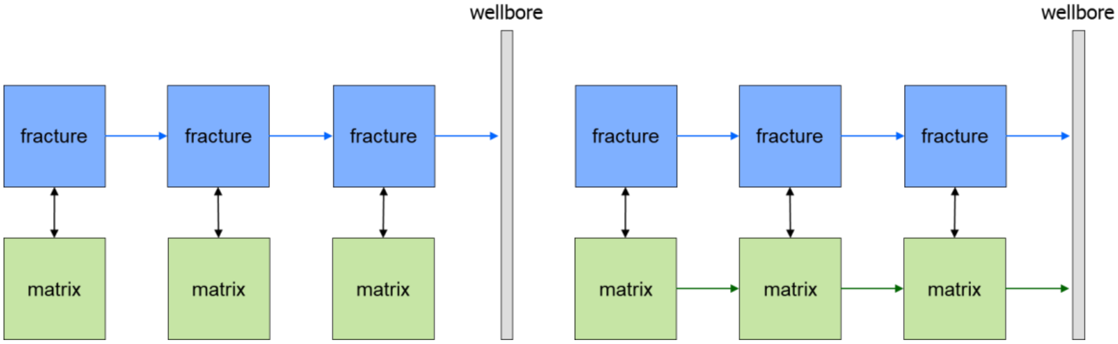

(a) (b)

Figure 3.11 Illustrations of (a) DPSK model, and (b) DPDK model (reprinted with permission from Chen et al., 2021)

2D homogeneous case. First, we applied our approach to a simple 2D homogeneous DPDK system with a single well at the center of the domain completed in both matrix and fracture system. The flow domain is discretized into 101×101×1 gridblocks (for each domain) with cell sizes of 29.7×29.7×100 (ft^3). The fluid properties are same as the validation case. Uniform grid properties are assigned and summarized in Table 3.1. Note that σ is a geometric shape factor (Kazemi, Merrill Jr, et al. 1976).

Parameter	Value
Permeability (matrix, fracture), k_m, k_f (mD)	1.0e-4, 1.0
Porosity (matrix, fracture), ϕ_m, ϕ_f, (-)	0.05, 0.01
Shape factor, σ, (ft^{-2})	0.12

Table 3.1 Inputs for the 2D homogeneous case (reprinted with permission from Chen et al., 2021)

Figure 3.12 presents the drainage volume evolution using different threshold DTOF values. Specifically, τ = 5, 10, and 20 ($\sqrt{hr}$), corresponding to some timings showing different characteristics:

1. The pressure front propagation visible only in the fracture domain
2. We start seeing the pressure front propagation in the matrix domain. The front in the fracture domain has evolved further.
3. The pressure front covers the entire fracture domain and majority of the matrix domain.

The visualizations provide useful insights regarding the propagating pressure front in the two interacting continua. More detailed analyses can be done using the $V_p(\tau)$ and $w(\tau)$ plots shown in Figure 3.13. As expected, the pressure front propagates within the more conductive fracture domain in the beginning, and then propagates in the matrix at a later time. The magnitude of $V_p(\tau)$ is different for the two continua (Figure 3.13a). This is because the matrix domain has greater pore volume. In addition, in the $w(\tau)$ diagnostic plot (Figure 3.13b), we see a unit slope corresponding to radial flow in the fracture domain at early time. Next, the $w(\tau)$ shows an increase at $\tau \sim 6(\sqrt{hr})$ which corresponds to the timing when the pressure front starts propagating in the matrix domain (the green line in Figure 3.13a). Later, while we start seeing the boundary effects in the fracture domain at $\tau \sim 15(\sqrt{hr})$, the $w(\tau)$ does not show a drop because the pressure front is still propagating in the matrix domain. Finally, beyond $\tau \sim 20(\sqrt{hr})$, the pressure front arrived at the boundary in the matrix domain and as a result, the $w(\tau)$ shows a signature of boundary dominated pseudo steady state.

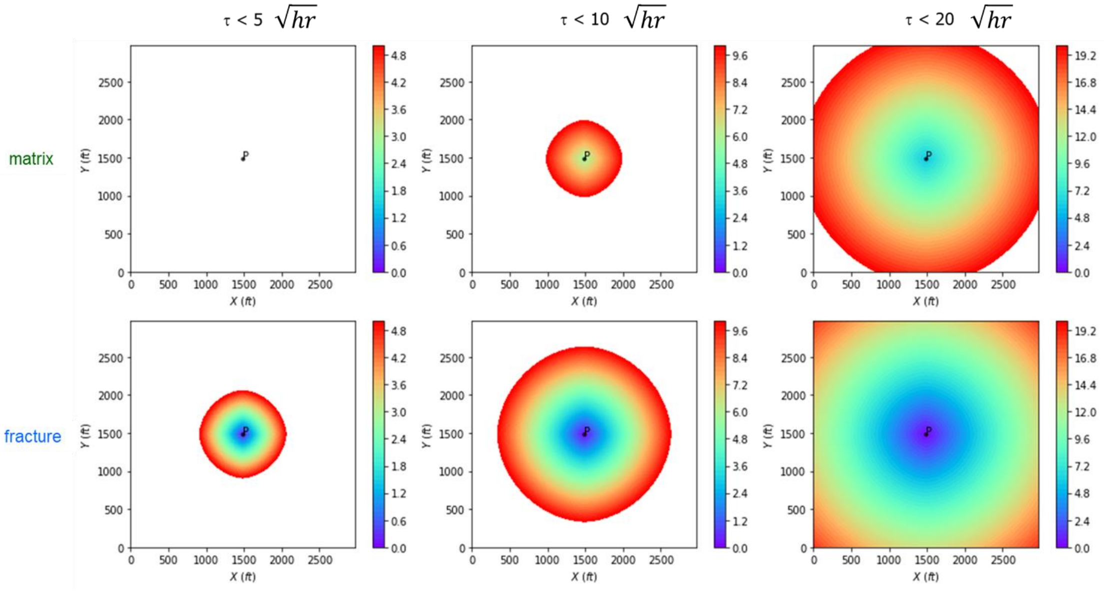

Figure 3.12 Visualizing the evolution of the drainage volume in the 2D homogeneous DPDK model using different DTOF threshold values (reprinted with permission from Chen et al., 2021)

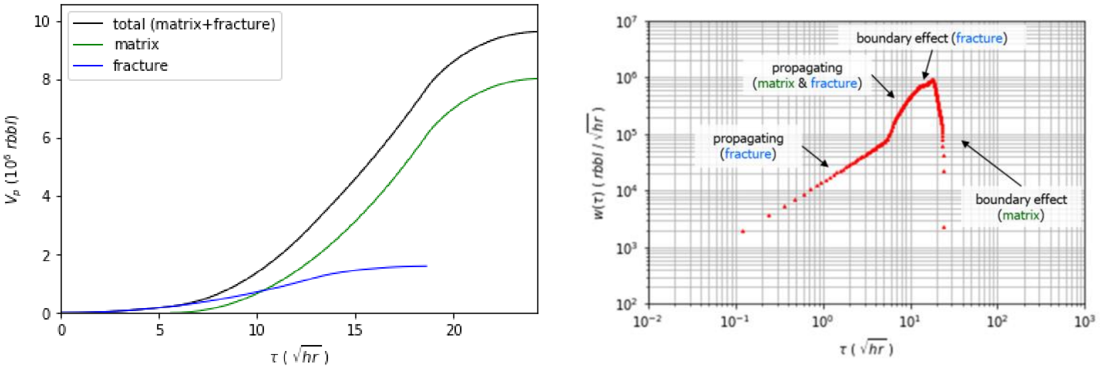

(a) (b)

Figure 3.13 Diagnostic plots for the 2D homogeneous DPDK model: (a) $V_p(\tau)$ and (b) $w(\tau)$ (reprinted with permission from Chen et al., 2021)

Sensitivity Analysis. Sensitivity studies were conducted to evaluate the effects of influential parameters on pressure front propagation in DPDK systems. Specifically, we attempt to investigate the effects of shape factor (fracture geometry), σ, and matrix permeability, k_m. Both contribute to the transfer transmissibility (Kazemi, Merrill Jr, et al. 1976). To this end, we defined ranges to be explored for each of the parameters shown in Table 3.2, ran the finite volume based FMM to cases with low/high values, and compared the DTOF maps and the diagnostic plots. Since the goal here is to investigate the influences of σ and k_m over the pressure propagation in the matrix, we select $\tau = 20\sqrt{hr}$ as the investigation time when the fracture media is already fully covered by the pressure front.

Parameter	Low	Mid	High
shape factor, σ, (ft^{-2})	0.012	0.12	1.2
matrix permeability, k_m, (mD)	1.0e-6	1.0e-4	1.0e-2

Table 3.2 Parameters for the sensitivity study for DPDK systems (reprinted with permission from Chen et al., 2021)

A visual inspection of the drainage volume evolution maps for different σ and k_m are provided in Figure 3.14 and Figure 3.15. Similar trends are obtained in the fracture domain using different values of σ and k_m, whereas, we see greater drainage volume as σ and k_m increase in the matrix domain, as expected. The corresponding $w(\tau)$ diagnostic plots are shown in Figure 3.16. A first observation is that, σ contributes to the timing of the pressure front arrival into the matrix domain. In Figure 3.16a, all the cases show a unit slope corresponding to radial flow at early time. Later, the pressure front arrives at the matrix domain, and we see increases in the $w(\tau)$ plot whose timing varies depending upon the σ values. While the matrix domain starts draining before the boundary effects in the fracture domain come into play in the base case (σ=0.12 ft^{-2}) and the case with the high value (σ =1.2 ft^{-2}), the matrix domain starts draining after the fracture domain is fully propagated in the low value case (σ=0.012 ft^{-2}). As a result, the $w(\tau)$ (the low value case, σ=0.012 ft^{-2}) increases for the second time after the first drop caused by the boundary dominated flow in the fracture domain. Figure 3.16b shows the effect of matrix permeability, k_m, on the $w(\tau)$ diagnostic plot in which noticeable differences compared to the shape factor sensitivity (Figure 3.16a) are observed at early time for the high value case (k_m=1.0e-2 mD). That is, we do not see a unit slope, a signature of radial flow. The unit slope in other cases are resulted from the radial flow in the fracture domain. The slope increases more than the unit slope as the pressure front starts propagating in the matrix domain. We miss the lag caused by the delay of pressure propagation in the matrix domain in the high matrix permeability case, and there are two possible reasons. First, the magnitude of k_m ratio (=$k_{m,high}/k_{m,base}$) is greater than that of σ ratio (=$\sigma_{high}/\sigma_{base}$). As a result, the use of $k_{m,high}$ enhances matrix-fracture connections more that σ_{high} does. Note here that the transfer transmissibility is defined as $T=C\cdot k_m\cdot V_{b,m}\cdot\sigma$ where C is a unit conversion constant (field), k_m is matrix permeability, $V_{b,m}$ is bulk volume of the matrix gridblock, and σ is the shape factor (Schlumberger 2015). This explains the first reason. Second, the matrix permeability contributes to not only matrix-fracture connections, but also matrix-matrix connections. The different trends using the low value (k_m=1.0e-6 mD) can be explained similarly.

We note here that the detailed analyses on the basis of the DTOF and $w(\tau)$ for DPDK systems were achieved using our finite volume based FMM approach, which would be difficult with the existing FMM-based approaches, and in fact, DPDK systems have never been explored in the context of the DTOF and $w(\tau)$ in the past for understanding flow regimes.

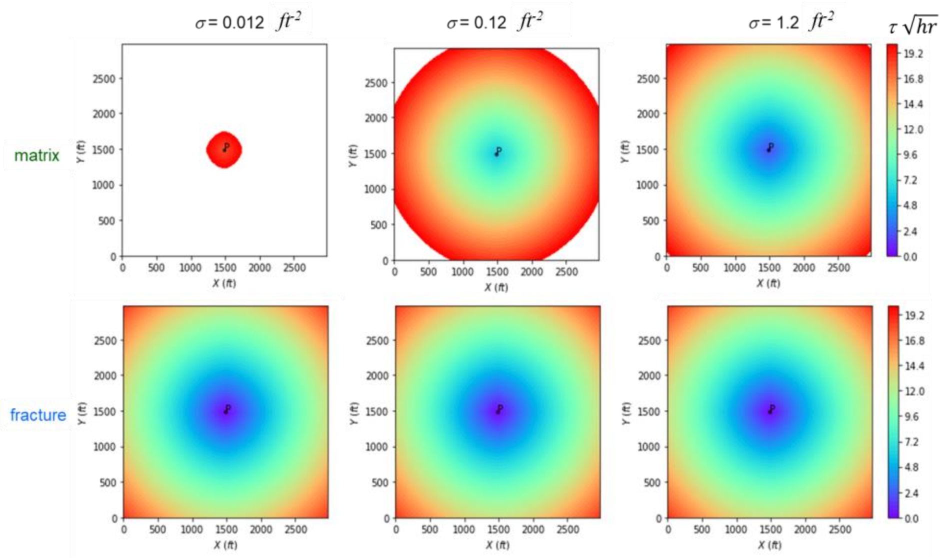

Figure 3.14 Visualizing the evolution of the drainage volume in the 2D homogeneous DPDK model using different values of shape factor, σ. The threshold value of τ is 20 ($\sqrt{hr}$) (reprinted with permission from Chen et al., 2021).

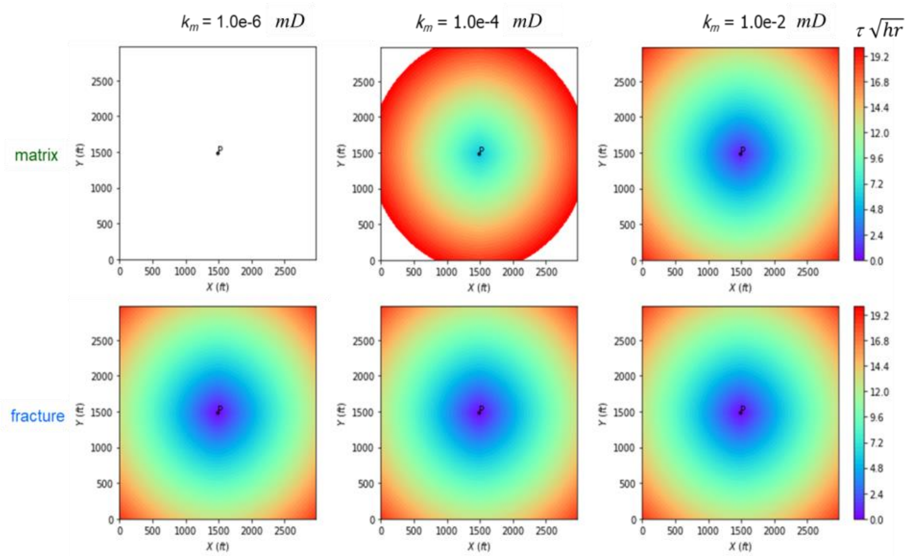

Figure 3.15 Visualizing the evolution of the drainage volume in the 2D homogeneous DPDK model using different values of matrix permeability, k_m. The threshold value of τ is 20 ($\sqrt{hr}$) (reprinted with permission from Chen et al., 2021).

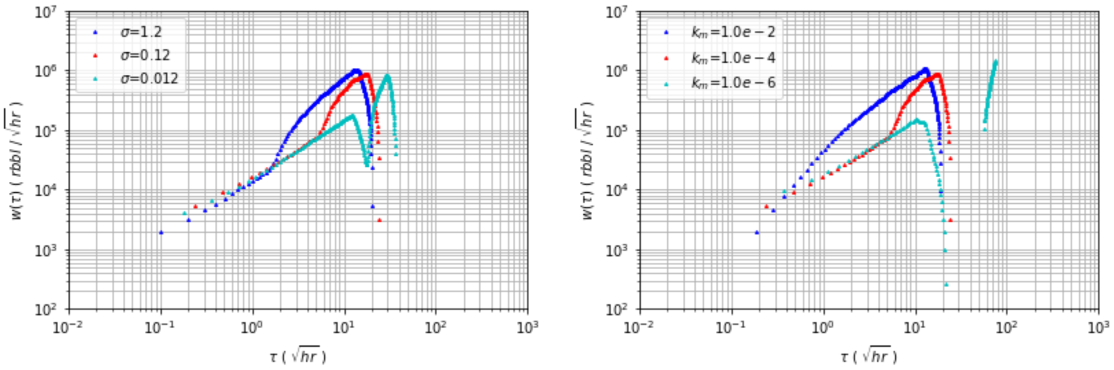

(a) (b)

Figure 3.16 $w(\tau)$ diagnostic plots investigating sensitivities of (a) shape factor, σ, and (b) matrix permeability, k_m based on the 2D homogeneous DPDK model (reprinted with permission from Chen et al., 2021)

2D heterogeneous case. We repeated the same exercises using a 2D heterogeneous case. This time, the fracture permeability is heterogeneous as shown in Figure 3.17, whereas, the matrix permeability remains homogeneous (k_m=*1.0e-4 mD*). The other inputs are same as the example 1.

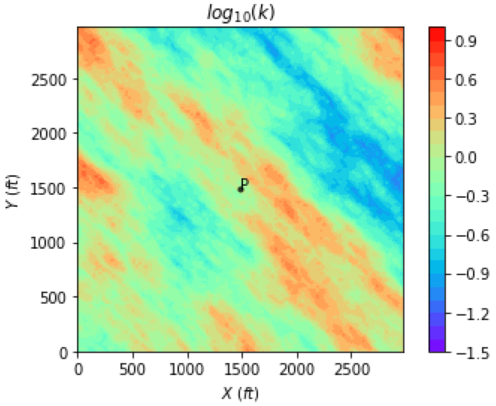

Figure 3.17 2D Heterogeneous DPDK model: heterogeneous fracture permeability and uniform matrix permeability (k_m=*1.0e-4 mD*) (reprinted with permission from Chen et al., 2021)

The maps of drainage volume evolution using different DTOF threshold values are provided in Figure 3.18. An interesting observation here is the pressure front propagation in the matrix domain. Although the matrix domain has uniform grid properties, shape of the DTOF contour maps is twisted (top row, Figure 3.18). This implies that the drainage in the matrix domain is dominated by the pressure propagations through the matrix-fracture connections, rather than the matrix-matrix connections. In addition, the $V_p(\tau)$ and $w(\tau)$ plots are shown in Figure 3.19. Slightly different results are obtained compared to the previous example due to fracture heterogeneity; however, the overall trends and flow regimes are similar.

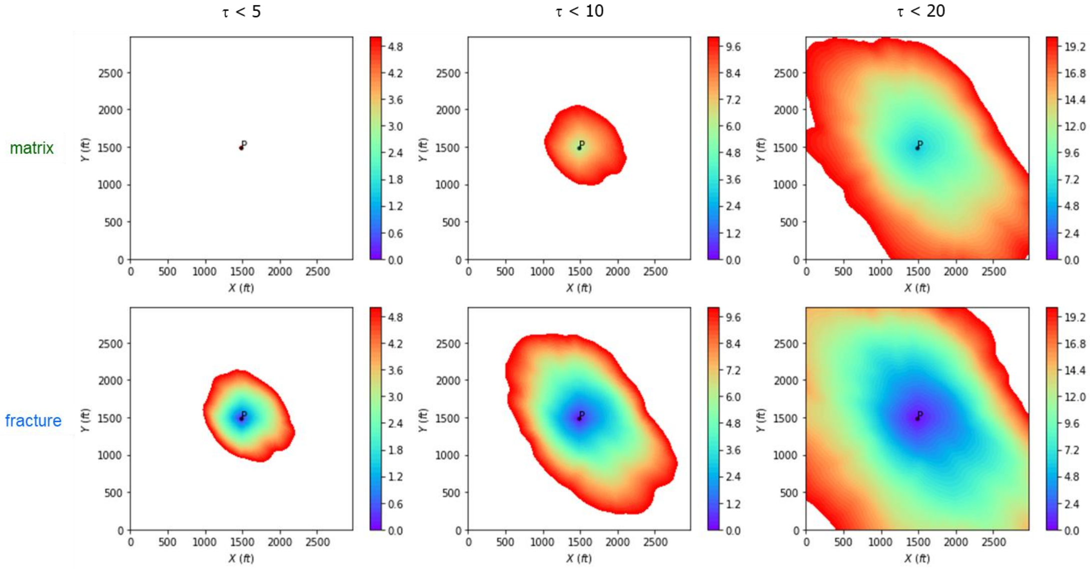

Figure 3.18 Visualizing the evolution of the drainage volume in the 2D heterogeneous DPDK model using different threshold values (in $\sqrt{hr}$) (reprinted with permission from Chen et al., 2021)

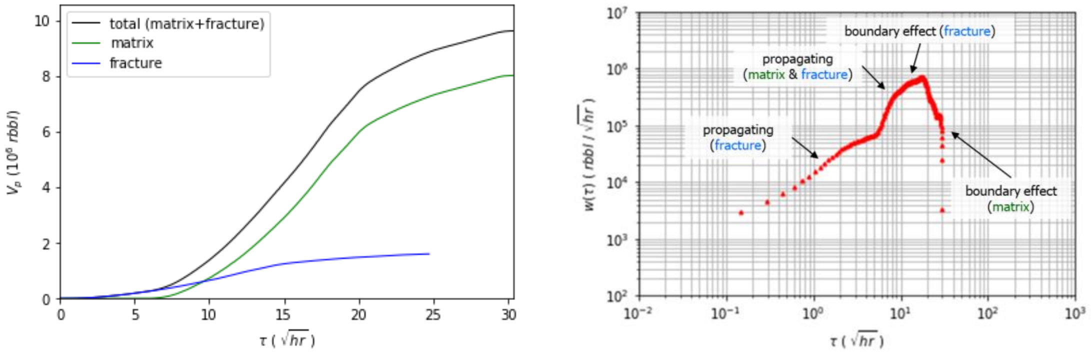

(a) (b)

Figure 3.19 Diagnostic plots for the 2D heterogenous DPDK model: (a) $V_p(\tau)$ and (b) $w(\tau)$ (reprinted with permission from Chen et al., 2021)

Sensitivity Analysis. Again, we conducted sensitivity studies to evaluate the effects of shape factor, σ, and matrix permeability, k_m, using the same parameters ranges (Table 3.2). While we observed different trends to a certain degree due to the heterogeneity, in general, same conclusions can be drawn from this study as the homogeneous reservoir.

Field-scale application. We applied our approach to a field-scale shale gas reservoir based on (Fujita et al. 2016). The model size is 2,000×4,000×150 (ft^3) with 200×400×30 grid discretization for each of the domains (~4.8 million active gridblocks). Figure 3.20 shows the heterogeneous permeability distribution for the fracture domain. The matrix domain has uniform permeability and porosity values of 1.0e-4 *mD* and 0.1 respectively, and a uniform porosity of 0.01 is used for the fracture domain. A homogeneous shape factor of 0.12 is assumed. The fluid model is based on the original study by (Fujita et al. 2016). The model comprises a single horizontal well with 12 hydraulic fractures using the original grid resolution. Effective values of grid permeability are assigned to the hydraulic fractures. With the large number of gridblocks and the additional matrix-fracture connections (2.4 million matrix-fracture connections), this is a challenging application of our proposed approach.

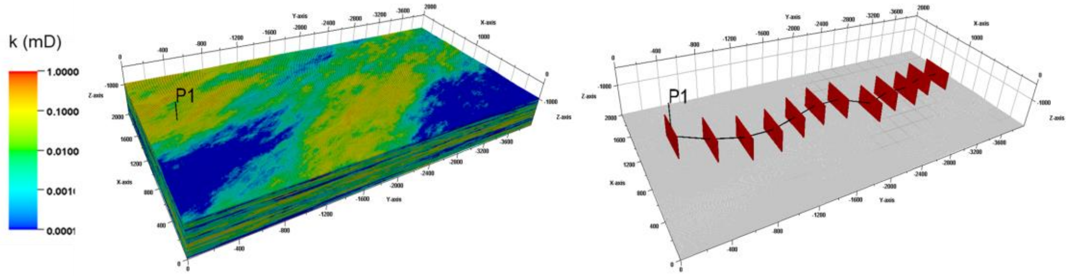

Figure 3.20 Field-scale gas reservoir showing fracture permeability field, and hydraulic fractures along the horizontal well (reprinted with permission from Chen et al., 2021)

The reservoir drainage by the well at various times by thresholding the DTOF, and corresponding $w(\tau)$ diagnostic plot are shown in Figure 3.21, and Figure 3.22. We can identify multiple flow regimes. At the beginning, the pressure front propagates inside the hydraulic fracture planes, followed by the propagation beyond the hydraulic fracture planes into the fracture domain. Later, the matrix domain starts draining. Finally, the pressure front reaches the domain boundaries and the $w(\tau)$ shows a drop. It is worth mentioning that the FMM calculations only cost roughly 17 seconds using a 64-bit Intel® Xeon® central processing unit (CPU) E5-2630 v4 at 2.20 GHz and 32.0 GB RAM. Note here that we focused on the CPU time of the FMM solver itself excluding I/O. Despite the complexity of the model with multi-million gridblocks, the efficacy of our implementation is demonstrated here.

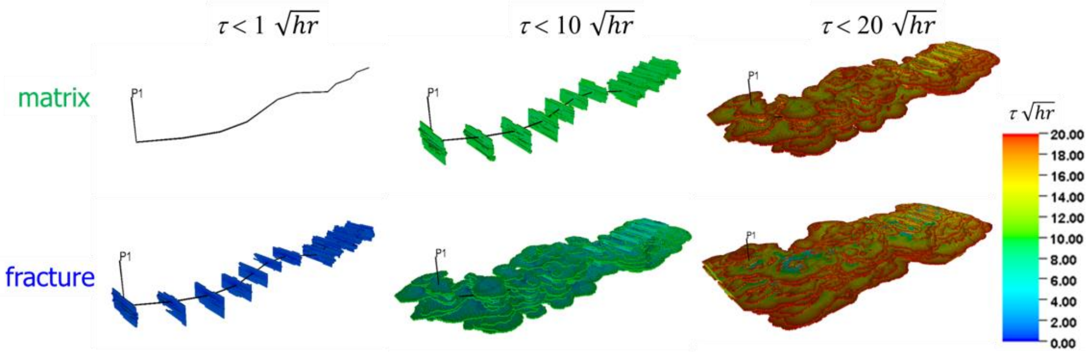

Figure 3.21 Visualizing the evolution of the drainage volume in the 3D DPDK model using different DTOF threshold values (reprinted with permission from Chen et al., 2021)

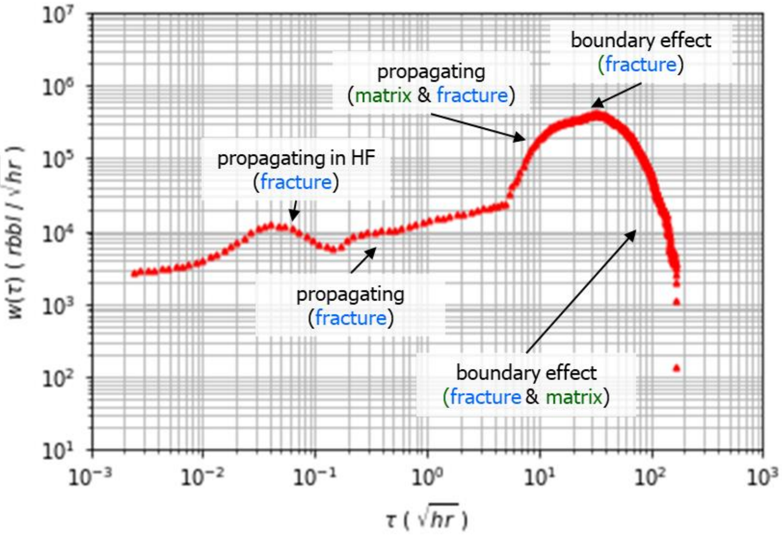

Figure 3.22 $w(\tau)$ plot for the field scale DPDK gas reservoir (reprinted with permission from Chen et al., 2021)

3.5.2 Embedded Discrete Fracture Models

Next, we applied our approach to the embedded discrete fracture models (EDFM). In the EDFM, the reservoir gridblocks are used to represent the matrix domain, while dominant fractures are explicitly described within the matrix domain as 2D planes. The matrix-fracture interactions are modeled by a local flow assumption with appropriate transmissibility which typically employs non-neighbor connections (NNCs) in the implementation. The realistic representation of large fractures and the flexibility in gridding are quite advantageous, and the EDFM approach is currently recognized as a promising alternative to classical fracture modeling approaches. The EDFM approach was originally introduced by Li and Lee (2008), and Moinfar et al. (2014) and Ţene et al. (2017) are some of the notable extensions. In this work, our EDFM implementation is based on the original work.

3D homogeneous case. First, we applied our approach to a simple 3D homogeneous case with a single hydraulic fracture described by the EDFM approach (Figure 3.23). The matrix domain is discretized into 75×75×5 gridblocks with cell sizes of 20.0×20.0×20.0 (ft^3). The fluid modeled in this study assumes typical shale oil reservoir properties(Iino et al. 2017). More detailed grid properties are summarized in Table 3.3.

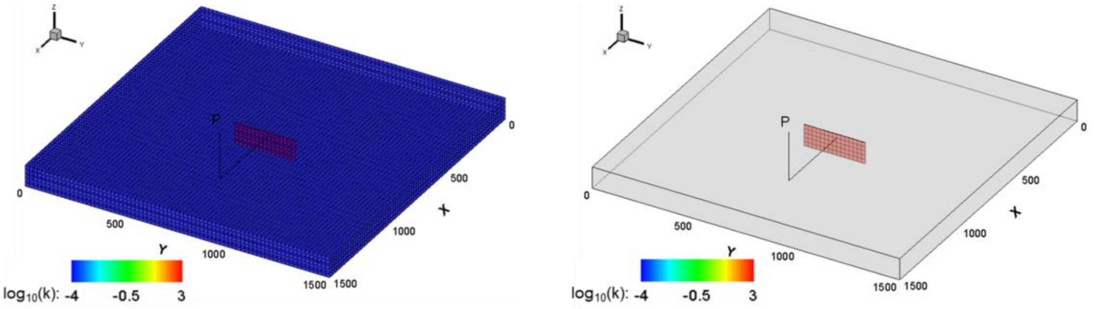

(a) (b)

Figure 3.23 Homogeneous 3D EDFM case showing uniform permeability distribution with a hydraulic fracture located at center of the domain. (a) with mesh, and (b) without matrix mesh (reprinted with permission from Chen et al., 2021)

Parameter	Value
Matrix	
Permeability, k_m, (mD)	1.0e-4
Porosity, ϕ_m, (-)	0.12
Hydraulic fracture	
Conductivity, $k_f w_f$, (mD-ft)	500
Porosity, ϕ_f, (-)	0.25
Half-length, x_f, (ft)	150
Height, h_f, (ft)	100

Table 3.3 Inputs for the 3D homogeneous EDFM case (reprinted with permission from Chen et al., 2021)

The results are summarized in Figure 3.24. As expected, the DTOF map shows linear flow at early time, followed by radial flow and boundary dominated PSS flow that correspond to the distinct $w(\tau)$ profiles, namely, a constant $w(\tau)$ at early time, followed by a unit slope and a sharp drop. These observations are consistent with the previous studies on the $w(\tau)$ diagnostic plots using a similar illustrative example (Yang et al. 2015, Xue et al. 2018).

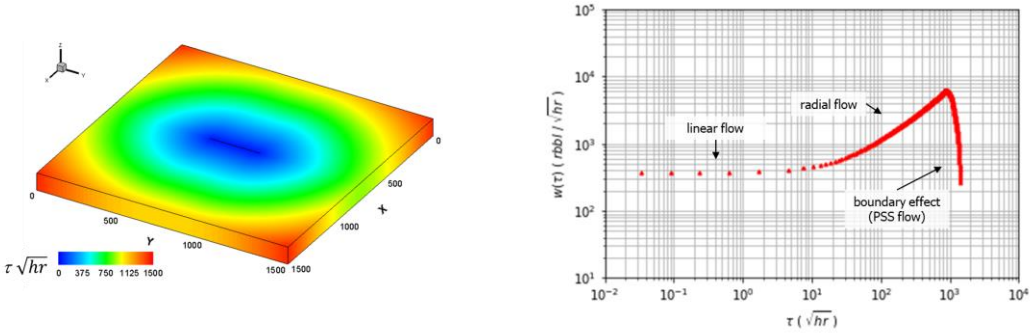

(a) (b)

Figure 3.24 FMM application on the 3D homogeneous EDFM case: (a) DTOF map and (b) $w(\tau)$ (reprinted with permission from Chen et al., 2021)

Unconventional reservoir with multistage hydraulic fractures. This case involves multistage hydraulic fractures along a horizontal well (Figure 3.25). The model settings are based on the previous study on the FMM implementation for the EDFM by Xue, Yang, et al. (2019a) in which 2.5D triangular prisms are the basic unit during the front tracking and the DTOF is calculated at local virtual tetrahedrons. While successful in cases with relatively small number of fractures, the approach becomes difficult to generalize as the number of fractures and their intersections increase because the sub-gridding becomes more and more complex. On the contrary, the proposed finite volume based approach depends on connections of the gridblocks, rather than the geometry, and can be seamlessly extended to the EDFM. We present an application of our implementation to a case involving a large number of natural fractures on top of the hydraulic fractures (case 2 in Figure 3.25). The case is sufficiently realistic and complex to demonstrate the efficacy and practicality of our approach. We note here that the natural fractures are generated using Petrel's fracture modeling module (Schlumberger). The same fluid model from the previous example (shale oil) is assumed, and the other detailed settings are summarized in Table 3.4.

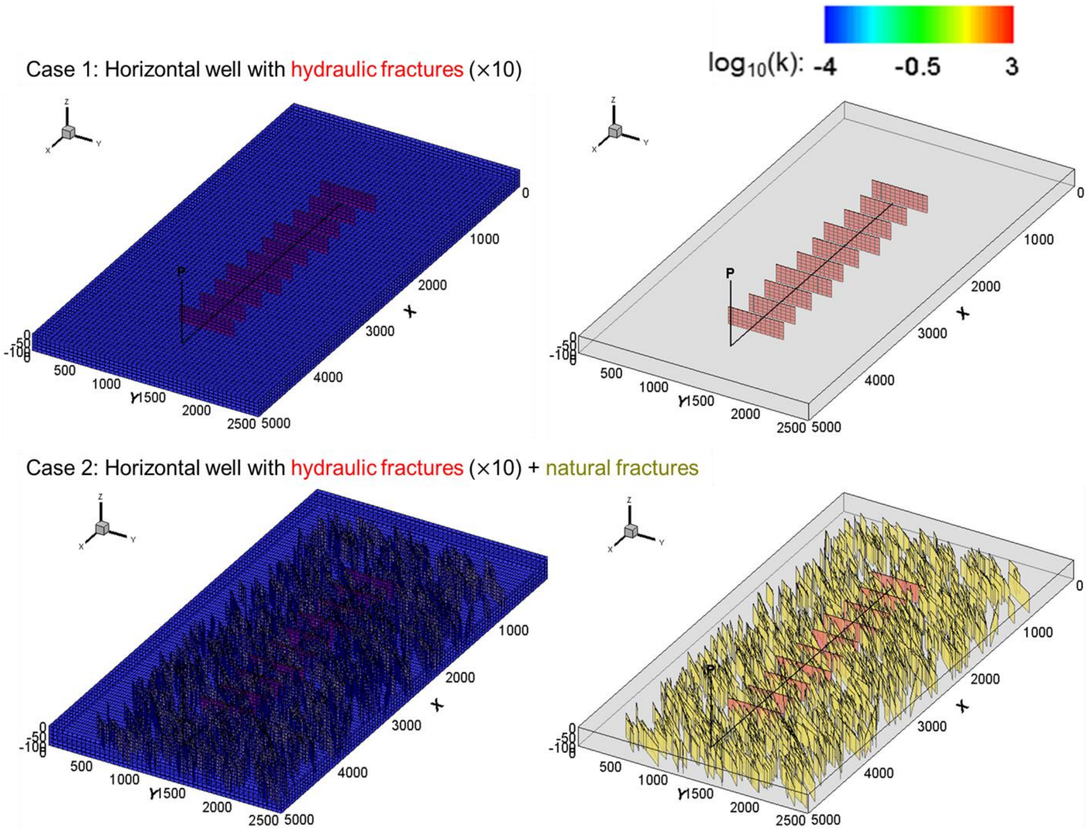

Figure 3.25 3D EDFM cases with hydraulic fractures along the horizontal well. Top: without natural fractures, and bottom: with natural fractures (reprinted with permission from Chen et al., 2021)

Parameter	Value
Matrix	
Permeability, k_m, (*mD*)	1.0e-4
Porosity, ϕ_m, (-)	0.046
Hydraulic fracture	
Conductivity, $k_f w_f$, (*mD-ft*)	200
Porosity, ϕ_f, (-)	0.25
Half-length, x_f, (*ft*)	250-300
Height, h_f, (*ft*)	100
Natural fracture	
Conductivity, $k_{nf} w_{nf}$, (*mD-ft*)	1.0
Porosity, ϕ_{nf}, (-)	0.25

Table 3.4 Inputs for the 3D realistic EDFM cases (reprinted with permission from Chen et al., 2021)

A comparison of the drainage volume evolution with and without natural fractures is provided in Figure 3.26a. The effects of the natural fractures can be clearly observed. Figure 3.26b shows the $w(\tau)$ diagnostic plot. While we have been focusing on identifying flow regimes using the trends of the $w(\tau)$ diagnostic plots, the amplitude of the $w(\tau)$ at early time and intermediate time can be used as an indicator of the fracture surface area. Specifically, greater magnitude of the $w(\tau)$ indicates greater fracture surface area, and vice versa. In Figure 3.26a, as one might expect, the magnitude of $w(\tau)$ in case 2 (with natural fractures) is greater than case 1 (without natural fractures) at early and intermediate time, due to the natural fractures. Also, case 2 shows the boundary effects earlier than case 1 (without natural fractures). This is also because of the natural fractures that are more conductive and enhances the speed of the pressure front propagation. Finally, we conducted a CPU time comparison using the same machine (a 64-bit Intel® Xeon® central processing unit (CPU) E5-2630 v4 at 2.20 GHz and 32.0 GB RAM). The CPU time for case 1 (25,540 active gridblocks) and case 2 (66,630 active gridblocks) are roughly 0.02 seconds and 0.07 seconds, respectively. This demonstrates the efficiency of our implementation, even for the cases involving complex natural fractures.

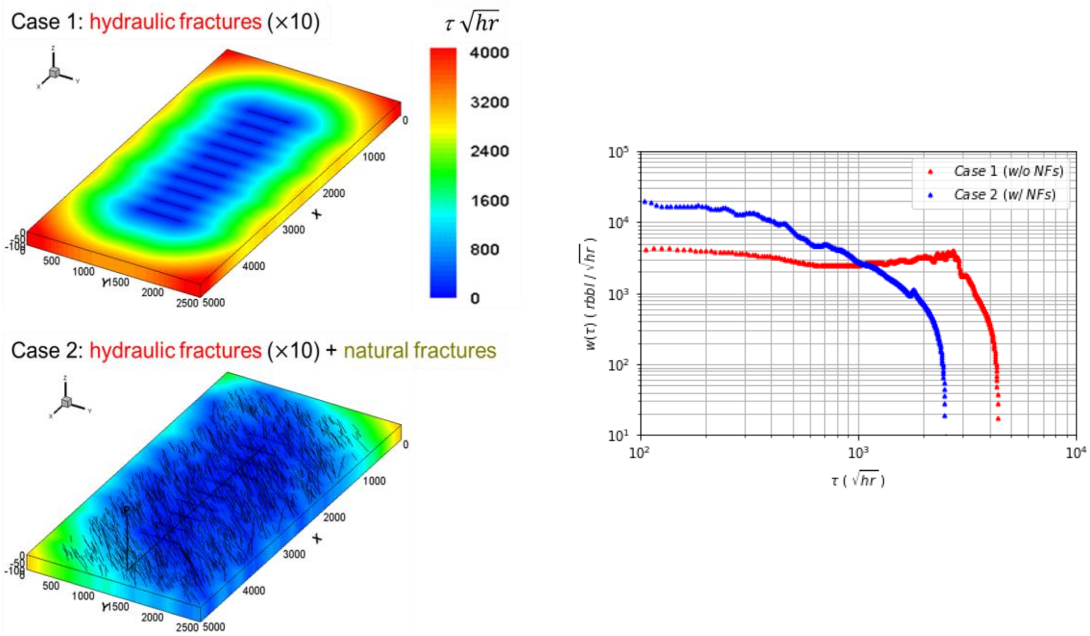

(a) (b)

Figure 3.26 FMM applications on 3D realistic EDFM cases: (a) DTOF maps and (b) $w(\tau)$ (reprinted with permission from Chen et al., 2021)

3.5.3 Unstructured Grid Systems

The last application of this novel finite volume based FMM will be on unstructured grids. Unstructured grids have been used to explicitly capture fluid flow in geometrically complex reservoirs with great flexibility (Heinemann et al. 1989, Palagi and Aziz 1994). They are able to maintain high resolution around fractures and are widely used to model fractured reservoirs. In the following unstructured grid examples, the Voronoi or PEBI gridding technique is used (Lie 2019). The Delaunay triangles are first generated such that no vertices of a triangle are inside the circumcircle of any other triangle. Next, the PEBI grid is formed by connecting the circumcenters of neighboring Delaunay triangles (Figure 3.27a). The transmissibility across the PEBI grid cells is deduced from the triangle geometry, and the detailed derivation and associated formulation can be found in Lie (2019).

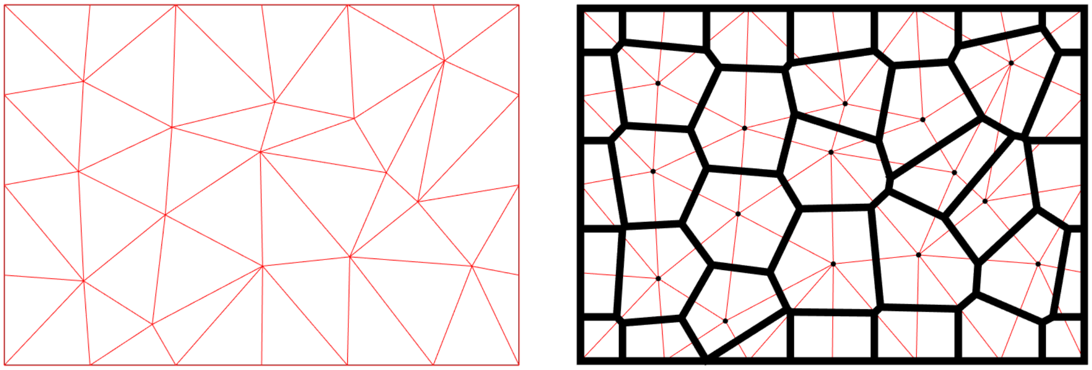
(a)

(b)

Figure 3.27 PEBI grid generation: (a) Delaunay triangulation and (b) PEBI grid based on the triangles (reprinted with permission from Chen et al., 2021)

Example 1: 2D homogeneous, isotropic case. The first example is a homogeneous square domain, 1,000*ft*×1,000*ft*. The permeability is 1*mD* and the porosity is 0.1. The grid consists of 17,424 cells with a producer at the center. Figure 3.28a shows the PEBI grid. For comparison purposes, the analytic DTOF is calculated at the centroids of PEBI grid cells (Figure 3.28b). The DTOF based on our proposed FMM is shown in Figure 3.28c. The FMM DTOF shows good agreement with the analytic DTOF. The relative error between the analytic and finite volume based FMM DTOF is 1.2×10^{-3}.

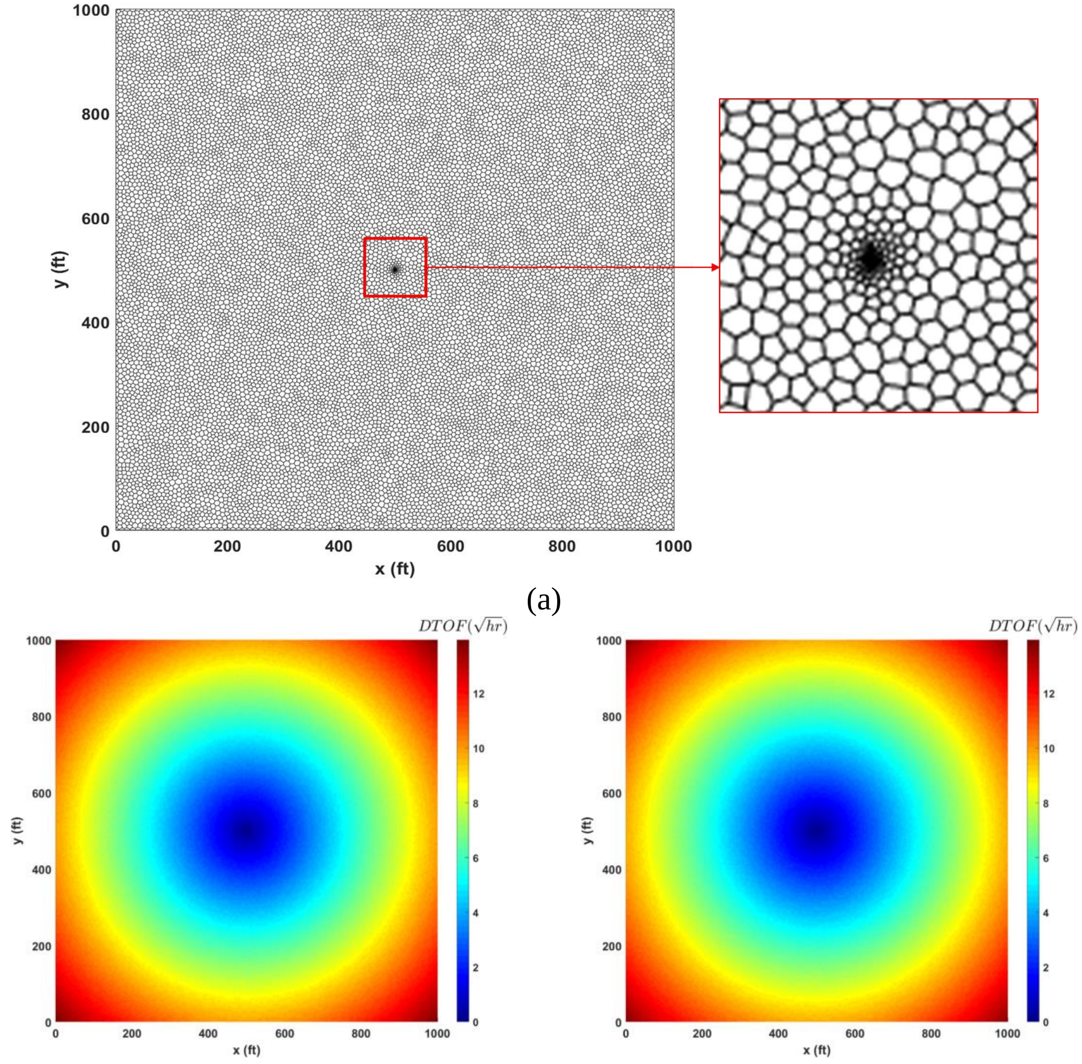

(a)

(b) (c)

Figure 3.28 2D Homogenous PEBI model: (a) grid, (b) analytic DTOF, (c) FMM-based DTOF (reprinted with permission from Chen et al., 2021)

The drainage volume and $w(\tau)$ diagnostic plot based on the analytic and finite volume based FMM DTOF are compared in Figure 3.29. Similar results are obtained compared to the previous validation example (Figure 3.6).

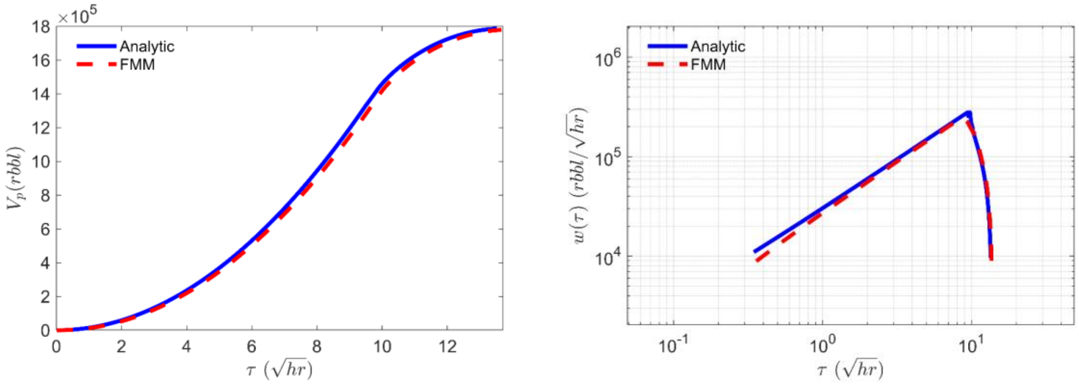

(a) (b)

Figure 3.29 Diagnostic plots comparing the analytical solution and our approach based on the 2D homogeneous PEBI model: (a) $V_p(\tau)$ and (b) $w(\tau)$ (reprinted with permission from Chen et al., 2021)

Example 2: 2D heterogeneous case. This example is using the same grid as example 1 but with heterogeneous permeability. Figure 3.30a shows permeability in log10 scale. Figure 3.30b shows the DTOF whose contours are distorted due to heterogeneity. The $w(\tau)$ diagnostic plot (Figure 3.30c) also reflects the impact of heterogeneity compared to Figure 3.29b.

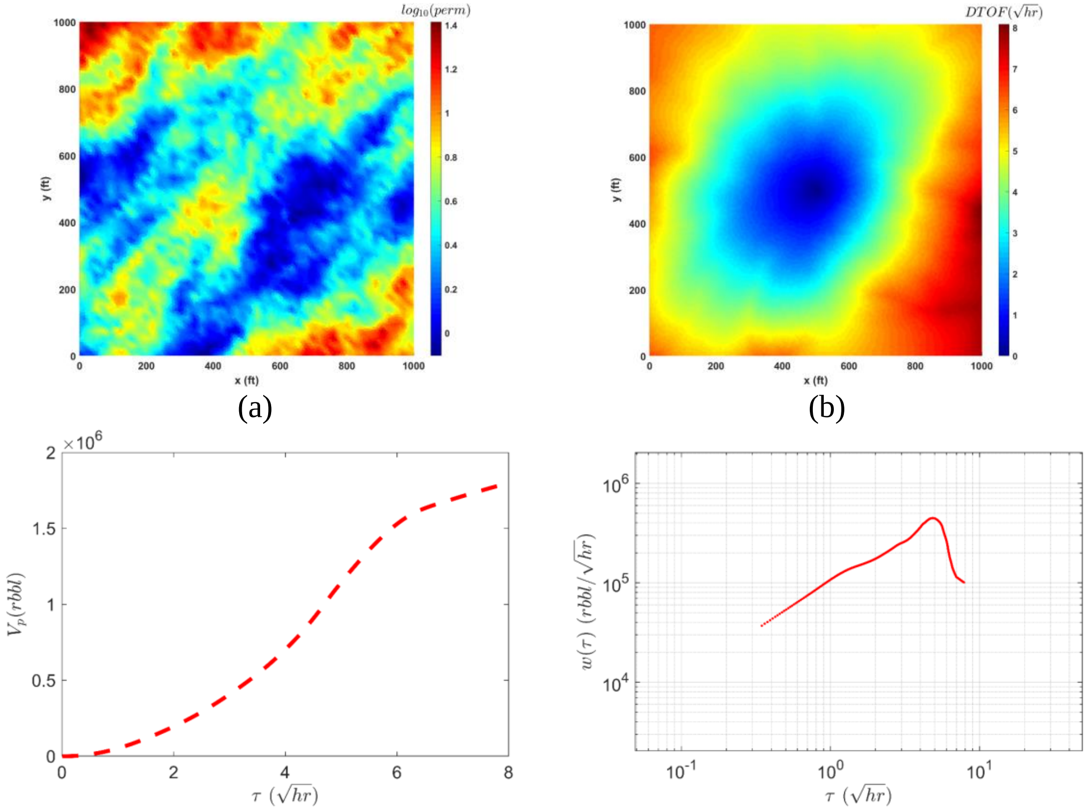

(a) (b)

(c) (d)

Figure 3.30 2D Heterogeneous PEBI model: (a) permeability field, (b) FMM-based DTOF, (c) $V_p(\tau)$, and (d) $w(\tau)$ (reprinted with permission from Chen et al., 2021)

Example 3: Complex fracture geometry. The last demonstration of the finite volume based FMM application on PEBI grid incorporates discrete fracture modeling. Two scenarios are examined. The first scenario contains simplified hydraulic fractures (Figure 3.31a), and the second scenario has natural fractures in addition (Figure 3.31b). The hydraulic fractures have a cluster spacing of approximate 200ft. The porosity is 0.05 for both the matrix and fractures. The matrix permeability is 0.0001 *mD*. Fracture conductivity for hydraulic and natural fractures are 10 *mD-ft* and 0.1 *mD-ft*, respectively. The pressure propagations in these two scenarios are shown in terms of DTOF (Figure 3.31c-d).

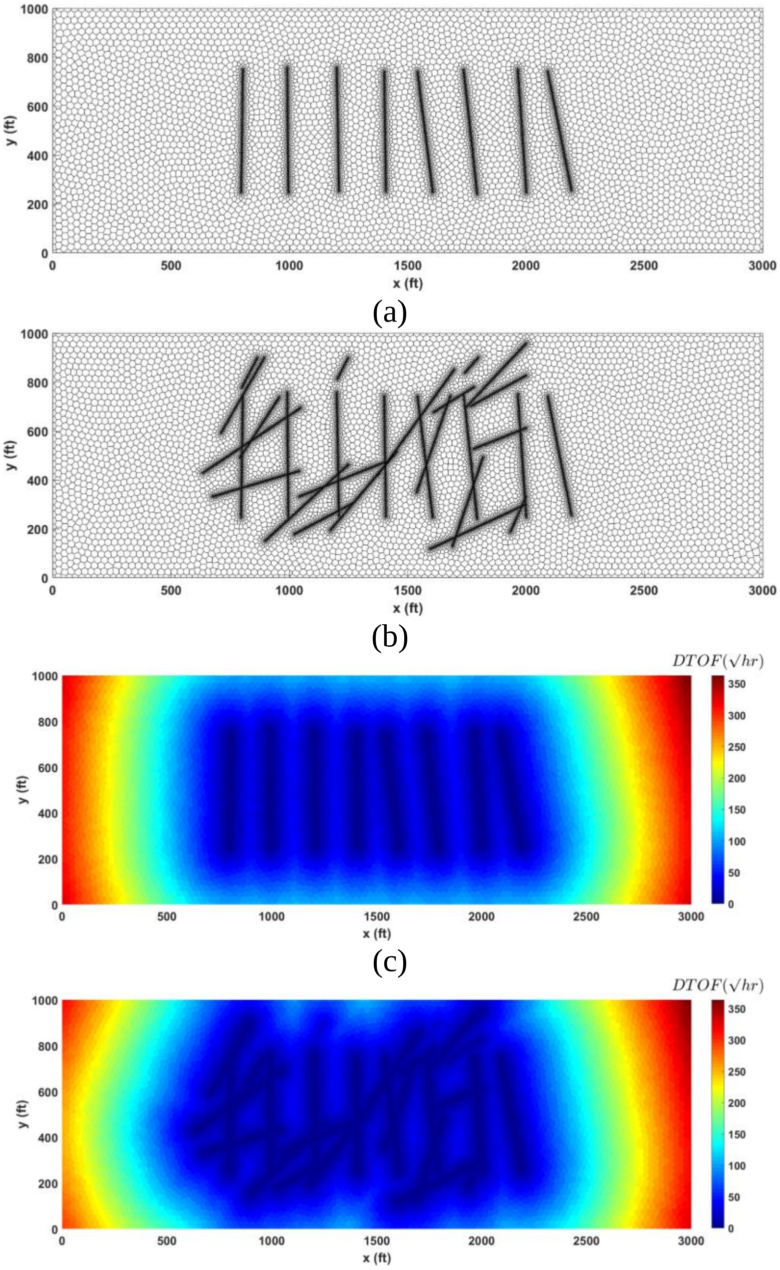

(a)

(b)

(c)

(d)

Figure 3.31 3D PEBI models: (a) scenario 1 containing hydraulic fracture only, (b) scenario 2 containing both hydraulic and natural fractures, (c) DTOF of scenario 1, and (d) DTOF of scenario 2 (reprinted with permission from Chen et al., 2021)

The example cases also show the impact of natural fractures on the transient process according to the drainage volume and $w(\tau)$ plots. The natural fractures connect the hydraulic fractures and ultimately form a network of fractures. Compared to scenario 1, scenario 2 has much faster pressure propagation (Figure 3.32a), larger surface area of the fracture network, indicated by the $w(\tau)$ value at early stage, and earlier detection of boundary effects (Figure 3.32b).

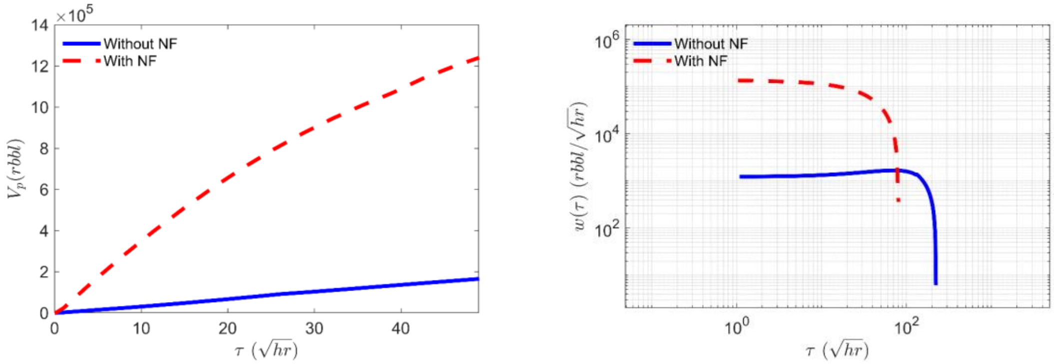

(a) (b)

Figure 3.32 Diagnostic plots comparing the two scenarios: (a) $V_p(\tau)$ and (b) $w(\tau)$ (reprinted with permission from Chen et al., 2021)

It is worth mentioning that unstructured grids are known for their capacity to preserve the transient fidelity in fracture models due to their high resolution around fractures (Cipolla et al. 2011). However, the fine grids also cause remarkable computation cost which can limit the application of unstructured grids in field scale applications. The FMM based approach presented here provides an efficient solution for ranking high fidelity fracture models.

3.6 Conclusions

In this study, we have proposed a novel and robust method for solving the Eikonal equation using finite volume discretization and the FMM. The approach can be applied to arbitrary simulation grids without the need of special treatments for irregular grid systems. The calculated DTOF provides powerful utilities in visualizing and analyzing the pressure front propagation in structured and unstructured grid systems.

- The finite volume form of the Eikonal equation is free of grid geometries and depends on cell volumes and intercell transmissibilities which are universal for both structured and unstructured grids and provided by finite volume simulators.
- The finite volume FMM implementation is validated with analytical solutions using isotropic and anisotropic models with homogeneous reservoir properties. Consistent DTOF distributions are obtained between the proposed approach and the analytical solutions.
- The implementation is applied to reservoirs with hydraulic and natural fractures modeled by complex grid systems such as DPDK models, EDFM, and unstructured grids (PEBI). The generated DTOF maps are utilized to visualize the pressure front propagation in fractured reservoirs. The $V_p(\tau)$ and $w(\tau)$ diagnostic plots based on the DTOF are used to identify flow regimes and fracture network surface area.
- For each type of grid, we have included applications on simplified and realistic field-scale fracture models. The simplified models illustrate the concepts and analysis involved in the applications, and the field-scale models demonstrate robustness and efficiency of the proposed method for realistic applications.

CHAPTER IV

AN EFFICIENT DEEP LEARNING-BASED WORKFLOW INCORPORATING A REDUCED PHYSICS MODEL FOR SUBSURFACE IMAGING IN UNCONVENTIONAL RESERVOIRS[§]

4.1 Chapter Summary

We present a novel deep learning-based workflow incorporating a reduced physics model that can efficiently visualize well drainage volume and pressure front propagation in unconventional reservoirs in near real-time. The visualizations can be readily used for qualitative and quantitative characterization and forecasting of unconventional reservoirs.

Our aim is to develop an efficient workflow that allows us to 'see' within the subsurface given measured data, such as production data. The most simplistic way to achieve the goal may be to merely train a deep learning-based regression model where the input consists of some measured data, and the output is a subsurface image, such as pressure field. However, the high output dimension that corresponds to spatio-temporal steps makes the training inefficient. To address this challenge, an autoencoder network is applied to discover lower dimensional latent variables that represent high dimensional output images. In our approach, the regression model is trained to predict latent variables,

---

[§] Part of this chapter is reprinted with permission from Onishi, Tsubasa, Chen, Hongquan, Datta-Gupta, Akhil et al. 2021. An Efficient Deep Learning-Based Workflow Incorporating a Reduced Physics Model for Subsurface Imaging in Unconventional Reservoirs. Proc., SPE Annual Technical Conference and Exhibition. Copyright 2021 Society of Petroleum Engineers. Further reproduction is prohibited without permission.

instead of directly constructing an image. In the prediction step, the trained regression model first predicts latent variables given measured data, then the latent variables will be used as inputs of the trained decoder to generate a subsurface image. In addition, fast marching-method (FMM)-based rapid simulation workflow which transforms original 2D or 3D problems into 1D problems, is used in place of full-physics simulation to efficiently generate datasets for training. The capability of the FMM-based rapid simulation allows us to generate sufficient datasets within realistic simulation times, even for field scale applications.

We first demonstrate the proposed approach using a simple illustrative example. Next, the approach is applied to a field scale reservoir model based on publicly available data on the Hydraulic Fracturing Test Site-I (HFTS-I), which is sufficiently complex to demonstrate the power and efficacy of the approach. We will further demonstrate the utility of the approach to account for subsurface uncertainty.

Our approach, for the first time, allows for data-driven visualization of unconventional well drainage volume in 3D. The novelty of our approach is the framework which combines the strengths of deep learning-based models and the FMM-based rapid simulation. The workflow has flexibility to incorporate various asset types and associated measured data.

4.2 Introduction

There has been extensive research on the development and application of modeling approaches for tight unconventional reservoirs as a response to their significant reserves in North America (EIA 2021). To date, many different approaches incorporating varying levels of data and physics have been proposed.

For time series data, such as production data, decline curve analysis (DCA) (Arps 1945, Fetkovich 1980, Carter 1985, Fetkovich et al. 1987, Blasingame et al. 1991, Palacio and Blasingame 1993, Agarwal et al. 1999, Ilk et al. 2008, Duong 2010, Valkó and Lee 2010) and pressure/rate transient analysis (PTA/RTA) (Wattenbarger et al. 1998, Ilk et al. 2010, Song and Ehlig-Economides 2011, Nobakht and Clarkson 2012b, 2012a, Uzun et al. 2016, He, Cheng, et al. 2018) have been widely used for forecasting and reservoir characterization. While these methods provide significant benefits in terms of simplicity and computational efficiency, capturing complex physics inherent in unconventional reservoirs, such as heterogeneities of hydraulic fracture and reservoir properties, still remains a challenge.

Numerical simulations are capable of capturing the complex nonlinear dynamics in unconventional reservoirs. Multiple continuum models (Warren and Root 1963, Kazemi, Merrill, et al. 1976), unstructured discrete fracture models (Cipolla et al. 2011, Cipolla et al. 2012, Sun and Schechter 2015, Marongiu-Porcu et al. 2016), multi-segment wells (Du et al. 2016), embedded discrete fracture models (EDFMs) (Li and Lee 2008, Moinfar et al. 2014, Ţene et al. 2017), and their hybrid models (Jiang and Younis 2016, Yang et al. 2018) are some of the notable numerical models. In most unconventional reservoir developments in the U.S., operators often first drill the minimum number of wells (parent wells) to hold the acreages, followed by drilling infill (child) wells to enhance the recovery (Lindsay et al. 2018). As many operators initiated their developments between 2003 and 2010, many parent wells have been depleted, leading to increasing number of infill wells in recent years. In fact, majority of the unconventional reservoirs have reached the point where the number of infill wells has surpassed that of newly drilled parent wells (Miller et al. 2016). Refracturing is another technique that can potentially improve the recovery from both parent and infill wells (Lindsay et al. 2016, Xu et al. 2017). Rather than the simple analytical models focusing on time series data, the capability of the numerical models that allows us to see within the subsurface by visualizing the simulation results on discretized gridblocks, such as pressure and stress fields, is particularly useful to better design field development plans including well and completion spacing as well as treatment designs. However, numerical simulation for unconventional reservoirs involving complex multiphase flow and geomechanics in high contrast systems with hydraulic and natural fractures can be too expensive to perform computationally intensive tasks like history matching, uncertainty quantification, and optimization.

To address the time consuming full physics simulations, the use of fast proxy or surrogate models has been extensively investigated. Reduced order models (ROMs) using a proper orthogonal decomposition (POD) (Van Doren et al. 2006, Cardoso et al. 2009, He and Durlofsky 2014, Ghasemi et al. 2015) or a dynamic mode decomposition (DMD) (Ghommem et al. 2013, Ghommem et al. 2016, Kutz et al. 2016, Bao and Gildin 2017) are some of the popular approaches on the basis of model decomposition. Although efficient, the training (offline) procedure requiring multiple full simulation runs can be computationally expensive. As a result, while applications of such ROMs to cases like 2D or simple 3D cases in both conventional and unconventional reservoirs are available (He et al. 2013, Klie and Florez 2020), field scale applications have not yet been fully explored. Another class of ROM is the fast-marching method (FMM)-based rapid simulation (Zhang et al. 2016). This method aims to achieve faster computations via coordinate transformation using the diffusive time-of-flight (DTOF), and it does not require the training processes as in the other ROMs discussed earlier. The DTOF represents the propagation time of the peak pressure disturbance caused by an impulse source and is given by a solution of the Eikonal equation which governs the propagation of pressure fronts and generalizes the depth of investigation for heterogeneous reservoirs (Datta-Gupta et al. 2011). The Eikonal equation can be efficiently solved by the FMM, a class of front tracking algorithm (Sethian 1999). Once the DTOF is obtained, the original 2D or 3D problems can be transformed into equivalent 1D problems along the DTOF, leading to significant savings in runtime of the simulation. The FMM-based simulation was originally developed for shale-gas reservoirs (Zhang et al. 2016), and has been extended to account for more complex problems including multi-phase and multi-component flow (Fujita et al. 2016, Iino et al. 2017), non-isothermal flow (Cui et al. 2016), gravity (Onishi et al. 2020), as well as more complex grid systems, such as unstructured grid (Yang et al. 2017) and EDFMs (Xue, Yang, et al. 2019a), and has shown to provide good approximation of full physics simulations. Furthermore, the robustness and efficiency of the method has been demonstrated by the field scale applications (Iino, Onishi, et al. 2020, Iino, Jung, et al. 2020).

The success of deep learning in a variety of fields including computer vision, natural language processing, and many others (Goodfellow et al. 2016) has led to the use of such techniques in subsurface modeling. We note here that the following literature review is focused on the models for predicting state maps that are relevant to our proposed workflow, rather than simpler models, for example, ones with a univariate output dimension. One of the earliest works reported by Zhu and Zabaras (2018) showed an application of an image-to-image regression using a convolutional encoder-decoder network, whereby gridblocks in the discretized flow domain are treated like pixels in an image, to construct a surrogate model that predicts state maps given permeability maps. The model is applied to a simple problem involving single phase steady-state flow with Gaussian permeability distribution. Extensions of the approach to multiphase flow (Mo et al. 2019) and non-Gaussian conductivity fields (Mo et al. 2020) were presented. In the context of reservoir simulation, Tang et al. (2020) applied a residual U-Net (Ronneberger et al. 2015) and a convolutional long short term memory recurrent neural network (Hochreiter and Schmidhuber 1997) to develop a surrogate model that predicts state maps and flow responses at wells given permeability maps in 2D channelized reservoir models. An application of the surrogate model within a probabilistic history matching workflow has been demonstrated. Subsequently, Zhong et al. (2021) presented a slightly different deep learning-based surrogate model using the coupled generative adversarial network (Co-GAN) that predicts pressure and saturation simultaneously. Several recent works have focused on the application of such techniques for modeling geologic CO_2 sequestration (Tang, Fu, et al. 2021, Tang, Ju, et al. 2021, Wen et al. 2021, Yan, Harp, Chen, et al. 2021).

Recently, there has been intensive research efforts on investigating the use of deep learning-based methods to solve forward and inverse problems in science and engineering applications. Notable works that brought a new paradigm of data-driven modeling have been presented by Raissi et al. (2019) and Zhu et al. (2019). The method is often referred to as physics-informed neural network (PINN) or physics-informed machine learning (PIML). While standard deep learning models are typically trained solely using data, the loss function in the PIML framework consists of data misfit term(s) as well as regularization term(s) based on some physical laws, which are typically residuals of governing partial differential equations, to ensure that the trained model is consistent with the given underlying physical laws. Partial derivatives in the physics term can be readily computed by leveraging the automatic differentiation (Baydin et al. 2018). In the field of reservoir modeling, applications of the PIML framework to the Buckley Leverett problem (Buckley and Leverett 1942) have been investigated by several authors (Fraces et al. 2020, Fuks 2020, Xu et al. 2021). More recently, Yan, Harp, and Pawar (2021) presented applications of PIML for modeling geologic CO_2 sequestration. Despite the widespread use of deep learning-based methods for subsurface modeling in recent years, the applications are mostly limited to simple cases like two phase flows in 2D or simple 3D grid systems. The challenge here is that the workflow becomes very expensive as the complexity of the problem in terms of size in space and time and nonlinearity increases. There are two components contributing to the expensive runtime: generating datasets for training by running a large number of full physics simulations and the training (solving the minimization problem) to find optimal weights and biases of the neurons. The latter tends to be more evident in the PIML framework due to the physics term(s) in the loss function that typically results in slower convergence, as in other minimization problems with regularizations.

In this paper, we put forth a novel deep learning-based workflow incorporating a ROM that can efficiently visualize the well drainage volume and pressure propagation in unconventional reservoirs. The workflow generates a subsurface image (e.g., pressure propagation) given routinely measured data from the fields (e.g., production data, distributed data along horizontal wells, etc.). The expensive runtime of full physics simulations is addressed by replacing the forward model by the FMM-based rapid simulation. Furthermore, we leverage an autoencoder for dimensionality reduction to further enhance the workflow. The architecture of the deep learning model is designed to be simple so that the choices of the ROM and measured data are readily changeable. As presented in the following sections, the proposed approach is simple, efficient, and applicable to 3D field scale unconventional reservoir models that involve a large number of hydraulic fractures and multiphase flow.

4.3 Methods

In this section, we first describe the FMM-based simulation approach, then provide a description of the proposed deep learning-based workflow, followed by an illustrative example.

4.3.1 The FMM-Based Rapid Simulation

In this study, we will take advantage of the FMM-based rapid simulation in place of the full physics simulation to accelerate the offline step. The workflow is summarized in Figure 4.1. Here, we will focus on the key concepts, and the reader is referred to Iino (2018) for more comprehensive details. The first step is to compute the multiphase diffusivity at all the gridlocks,

$$\alpha(\mathbf{x}) = \frac{\lambda_t(\mathbf{x}) k(\mathbf{x})}{\phi(\mathbf{x}) c_t(\mathbf{x})} \tag{4.1}$$

where, λ_t is total mobility, k is permeability, ϕ is porosity, c_t is total compressibility, and $\mathbf{x}$ is location. The next step is to compute the DTOF by solving the Eikonal equation which is derived from a high frequency asymptotic solution to the diffusivity equation. The derivation is based on an analogy between pressure propagation in porous media and wave propagation (Vasco and Datta-Gupta 2016).

$$\left|\nabla \tau(\mathbf{x})\right| = \frac{1}{\sqrt{\alpha(\mathbf{x})}} \tag{4.2}$$

where, τ and α are the DTOF and the diffusivity at location $\mathbf{x}$. The DTOF represents travel time of a propagating pressure front. The Eikonal equation can be solved by a front tracking algorithm called the FMM (Sethian 1999) that is very efficient, because the computations only involve solving local quadratic equations, and there is no global matrix inversion. Once the DTOF is obtained, it can be utilized as spatial coordinate to transform 3D problems into equivalent 1D problems. Visually, each of the rings in the step 2 in Figure 4.1 represents a single gridblock after the coordinate transformation. Mathematically, we can formulate 1D diffusivity equation as follows (Zhang et al. 2016),

$$\frac{1}{w(\tau)}\frac{\partial}{\partial\tau}\left[w(\tau)\frac{\partial p}{\partial\tau}\right]=\frac{\partial p}{\partial t} \tag{4.3}$$

where, the $w(\tau)$ function represents a surface area of propagating pressure front and defined as,

$$w(\tau)=\frac{\mathrm{d}V_p(\tau)}{\mathrm{d}\tau} \tag{4.4}$$

where, $V_p(\tau)$ is cumulative drainage pore volume along the DTOF. In other words, it is sum of pore volumes within gridblocks whose τ values are smaller than the τ of interest. After the coordinate transformation, the 1D flow domain is discretized, and the pore volumes and transmissibilities are computed. Finally, rapid 1D simulation is performed, which has been shown to be good approximation of the original 3D problem and offers significantly faster computations. While single phase and constant compressibility and viscosity are assumed in Eq. (4.3) for simplicity, extensions to multiphase and multicomponent flow as well as multiple continuum models are available in literature (Iino, Onishi, et al. 2020). This workflow will be used as a fast forward model in the following sections.

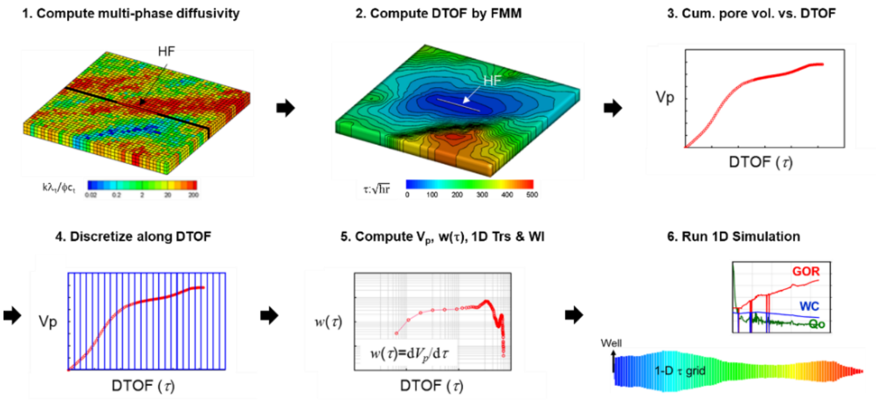

Figure 4.1 The FMM-based simulation workflow (Onishi et al. 2020) (reprinted with permission from Onishi et al., 2021)

4.3.2 The Proposed Approach

As an example, we consider a situation where measured data, including multiphase production rates, bottom-hole pressure, and flow rate along a lateral are available. Our aim is to develop an efficient workflow that allows us to 'see' within the subsurface given measured data (**Appendix A**).

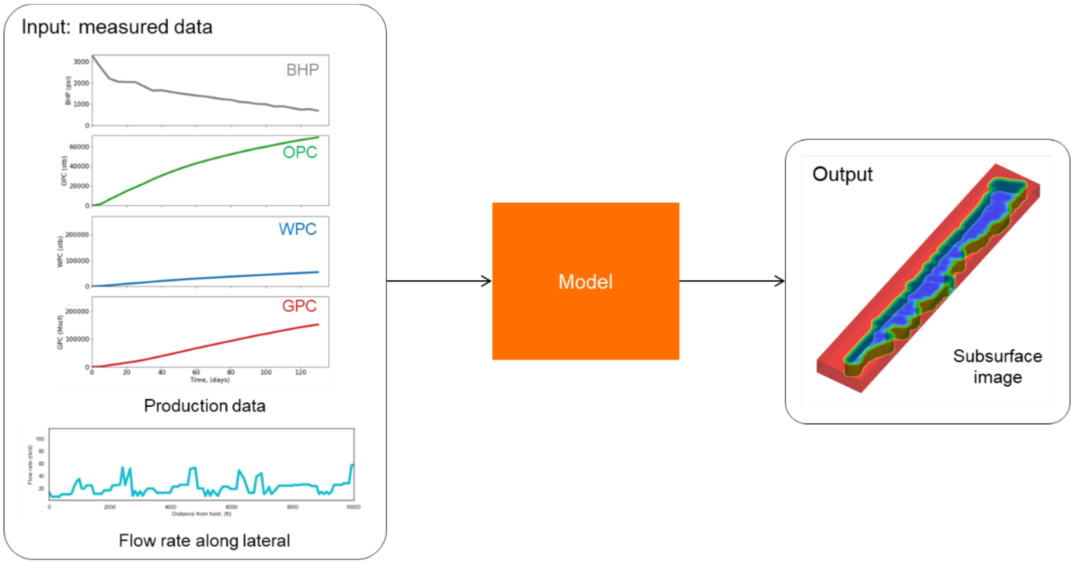

Figure 4.2 Overview of the proposed approach (reprinted with permission from Onishi et al., 2021)

The most simplistic model to achieve our objective may be a deep learning-based regression model using a feedforward neural network and convolutional neural networks (CNNs). Specifically, the inputs are first passed to the feedforward neural network containing several hidden layers. The last hidden layer is connected to a stack of CNNs that eventually outputs a 3D subsurface image. This simple architecture, however, may be difficult to train because of the high output dimension that corresponds to the number of discretized spatio-temporal steps. In practical applications, it can easily exceed the order of millions. A viable remedy would be the use of dimensionality reduction techniques, such as principal component analysis (PCA). PCA-based techniques have found various applications in geological parameterization (Oliver 1996, Reynolds et al. 1996, Sarma et al. 2006). A well-known limitation of the PCA-based parameterization techniques is the Gaussian assumption that makes it inapplicable to complex parameter distributions, such as those found in permeability distributions in channelized reservoirs (non-Gaussian). Subsequently, several extensions including the kernel PCA (KPCA) (Sarma et al. 2008) and the optimization-based PCA (O-PCA) (Vo and Durlofsky 2014) have been proposed. Recently, applications of deep learning-based generative models, such as (variational) autoencoders (Canchumuni et al. 2017, Laloy et al. 2017), generative adversarial network (GAN) (Chan and Elsheikh 2017, Laloy et al. 2018), and CNN-PCA (Liu et al. 2019), to geological parameterization are being actively explored. These techniques are essentially nonlinear generalization of PCA (Baldi and Hornik 1989) and have shown to outperform the existing PCA-based techniques in capturing more complex features. In our application, since the problem settings involve high contrast systems due to hydraulic and natural fractures, the output images are likely to exhibit sharp contrasts (similar to channelized reservoirs). Therefore, we adopt an autoencoder whose capability in capturing complex features is well suited for our problems of interest. Among the deep learning-based generative methods, an autoencoder may be one of the simplest methods. The use of more sophisticated methods will be investigated in future works.

A step by step workflow of the proposed approach is summarized in Figure 4.3, which is based on the well-known Design of Experiment (DoE)-based techniques (Bhark and

Dehghani 2014, Olalotiti-Lawal et al. 2018, Li et al. 2019). More detailed descriptions of the workflow in Figure 4.3 are as follows:

1. Parameters that potentially have influences on the objective function are identified, typically based on some prior knowledge. The objective function is defined as a root mean square error over n_d data points,

   $$O_j(\mathbf{m}) = \sqrt{\sum_{i=1}^{n_d} \left(d_i^{obs} - d_i^{sim}(\mathbf{m}) \right)^2 / n_d} \tag{4.5}$$

   where, $O_j(\mathbf{m})$ is the objective function for metric j (=oil production rate (OPR), water production rate (WPR), gas production rate (GPR), cumulative oil production (OPC), etc. at a certain well) given parameter $\mathbf{m}$, d_i^{obs} is observed data, and $d_i^{sim}(\mathbf{m})$ is simulation response given parameter $\mathbf{m}$ at step i. In this study, the one-variable-at-a-time design is applied to generate tornado plots, from which the influential parameters are selected for the subsequent steps. It should be noted that the simple tornado plots have several limitations: coverage of the uncertain space is limited, the results are strongly dependent on the base case, and interactions between parameters may not be accounted for (Li et al. 2019). More sophisticated statistical analysis, such as *t*-tests, will be considered in future work.
2. The selected influential parameters from the step 1 will be used in sampling via a Latin hypercube design (McKay et al. 2000) to generate cases for the FMM-based simulation. The number of samples is typically in the order of hundreds or thousands, depending on complexity of the problem.
3. The FMM-based rapid simulation is applied to the samples from the step 2 to generate datasets. The rapid simulation capability allows users to explore a variety of

parameters, even for field scale applications within realistic simulation times that would be difficult to achieve with full physics simulations.

4. The DTOF maps are used to train an autoencoder which learns a nonlinear mapping of an input image ($\mathbf{x}_i$) to a low dimensional latent space via $\mathbf{z}_i = \varphi(\mathbf{x}_i)$ (encoder), then back via $\hat{\mathbf{x}}_i = \psi(\mathbf{z}_i)$ (decoder) by solving the minimization problem,

$$\underset{\boldsymbol{\theta}_{AE}}{\arg\min} \frac{1}{n_s} \sum_{i=1}^{n_s} \left\| \mathbf{x}_i - \hat{\mathbf{x}}_i \right\|_2^2 \tag{4.6}$$

where, $\boldsymbol{\theta}_{AE}$ are the parameters to be tuned (weights and biases) in the autoencoder during the training, and n_s is the number of samples. The loss function is defined as a mean square error between an original DTOF image ($\mathbf{x}_i$) and a reconstructed DTOF image ($\hat{\mathbf{x}}_i$). Here, $\boldsymbol{\tau}_i$ is normalized to $\mathbf{x}_i$ [0 1] using minimum and maximum values of $\boldsymbol{\tau}$ among the training and validation datasets,

$$\mathbf{x}_i = \frac{\boldsymbol{\tau}_i - \tau_{\min}}{\tau_{\max} - \tau_{\min}} \tag{4.7}$$

The encoder and decoder include CNNs and dense layers, and more details of the architecture will be discussed in the following sections. In our application, instead of a set of pressure and saturation maps, a DTOF map is used as representative subsurface images over the simulation period. This means that each sample has only one image of DTOF, rather than a set of pressure and saturation maps over the time steps. The intention behind this is as follows:

- The use of a single DTOF image per realization allows us to work with much simpler autoencoder architecture compared to the use of a set of the state maps that may require more complex architecture like recurrent neural networks, making the training more difficult.

- Once we predict the DTOF, it can be readily used as a 1D spatial coordinate in the rapid FMM-based simulation, from which we can obtain pressure and saturation maps. The runtime of the FMM-based simulation is typically less than a few minutes. Alternatively, we could use a more complex autoencoder for a set of pressure and saturation maps to directly predict them. However, the computational cost for the training is expected to be more expensive.
- The DTOF depends on the multiphase diffusivity which is a function of pressure and saturation (Eq. (4.1)), and therefore can change during simulations. The initial condition is typically used to compute the multiphase diffusivity (step 1 in Figure 4.1). As reported by Iino, Onishi, et al. (2020), changes in the total mobility and total compressibility due to pressure and saturation changes are compensated by each other (Eq. (4.1)) in typical unconventional reservoir development scenarios (i.e., depletion), and the shape of the DTOF map does not significantly change during simulations. Therefore, it is reasonable to use a single representative DTOF image per realization.

5. In this step, we train a deep learning-based regression model consisting of a simple feedforward neural network that predicts a vector of the latent variable given measured data, such as production data, by solving the following minimization problem,

$$\underset{\boldsymbol{\theta}_{reg}}{\arg\min} \frac{1}{n_s} \sum_{i=1}^{n_s} \left\| \mathbf{z}_i - \hat{\mathbf{z}}_i \right\|_2^2 \tag{4.8}$$

where, $\boldsymbol{\theta}_{reg}$ are the weights and biases on the neurons in the regression model, $\mathbf{z}$ is the known latent variable (normalized to [0 1] in a similar manner to Eq. (4.7)) from the trained autoencoder, and $\hat{\mathbf{z}}$ is the predicted latent variables. While the multiphase production data and flow rate along the lateral are collected and saved for this step in Figure 4.3, the workflow has flexibility to incorporate different data types, and is applicable to various asset types and associated measured data.

6. We have already trained and saved the autoencoder (step 4) and the regression model (step 5) from the previous steps. In this step, the two models are combined to construct a hybrid model that consists of the regression model and the decoder (part of the autoencoder). The hybrid model predicts a DTOF map given measured data. An extension of the workflow to account for uncertainties will be discussed in the next section.

It should be noted that there exist recent works that present deep learning-based methods combining a regression model with an autoencoder (Champion et al. 2019, Razak and Jafarpour 2020) and an approach combining a reduced physics model and a response surface design (Tanaka et al. 2020), and part of our workflow is inspired by them. The novelty of our approach is the use of the FMM-based simulation and the concept of the DTOF that substantially accelerates the workflow, making it applicable to field-scale applications. Additionally, the simple and flexible workflow is applicable to various types of measured data.

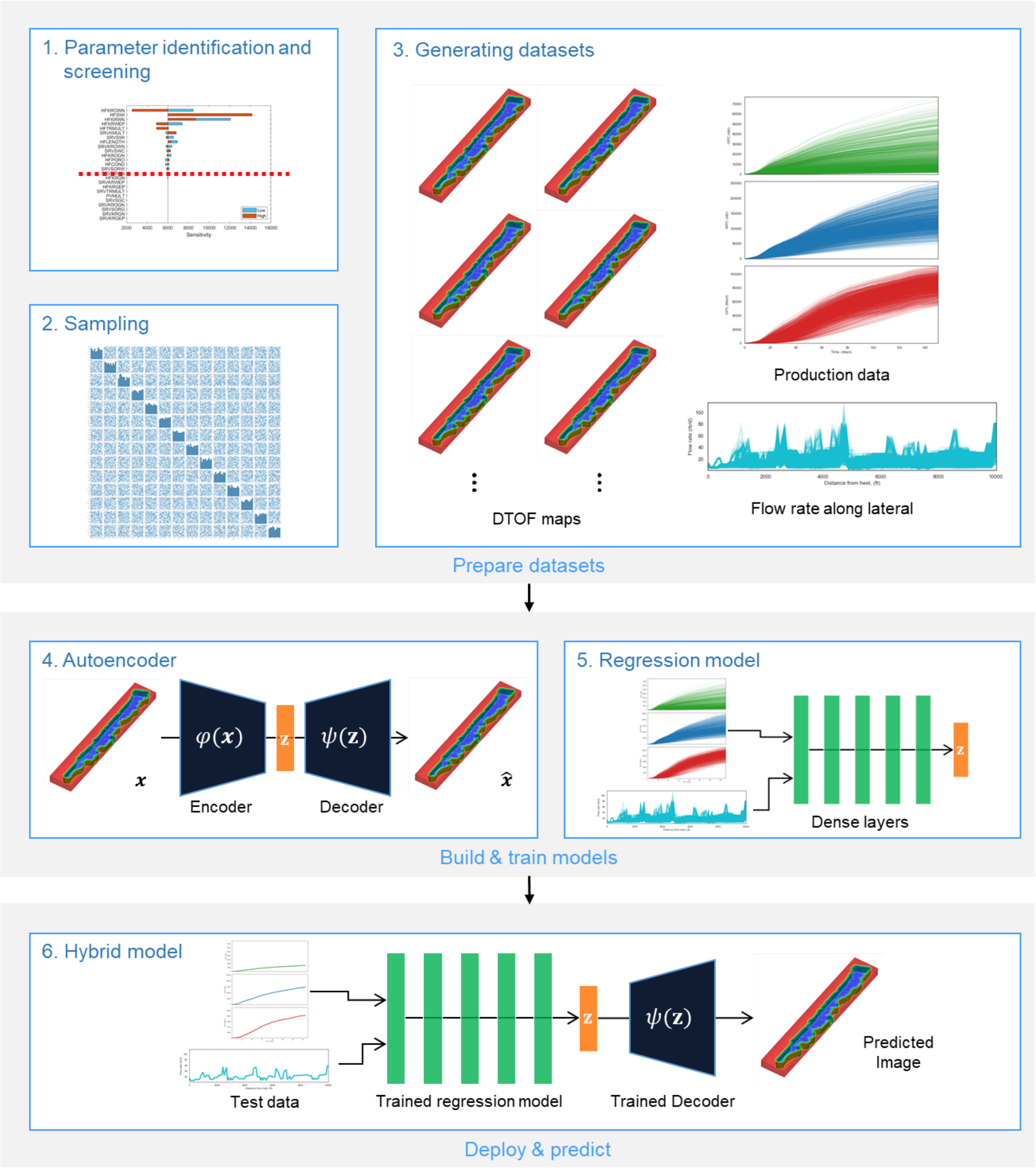

Figure 4.3 The proposed deep learning-based workflow incorporating the FMM-based rapid simulation (reprinted with permission from Onishi et al., 2021)

4.3.3. Example: A Synthetic Unconventional Reservoir

Case Description. In this section, we demonstrate the proposed workflow using a 2D synthetic unconventional reservoir. The model size is 1,000 × 1,000 × 10 ft^3 with

100×100×1 grid discretization for the matrix domain. The model consists of a horizontal well (P1) with 5 hydraulic fractures and 10 natural fractures as shown in Figure 4.4. In addition, there is a monitoring well (O1) near P1 that measures downhole pressure at the five gauges (gray dots along O1 in Figure 4.4). In this example, we skip the step 1 in Figure 4.3 and focus on geometry and orientation of both hydraulic and natural fractures as parameters of interest as shown in Table 4.1. Assuming uniform distributions for all the parameters, a Latin hypercube sampling is applied to generate 1,000 samples for step 3 in Figure 4.3. The fractures are described by the EDFM technique (Li and Lee 2008) that enables flexible mesh generation and is well suited for our application, where a large number of realizations with different fracture orientation and geometry will be generated. For hydraulic and natural fracture gridblocks, uniform conductivity values of 100 (mD-ft) and 10 (mD-ft) are assigned, and the matrix domain has homogeneous properties as shown in Figure 4.4. In addition, for the matrix gridblocks connected with: (1) the hydraulic fracture gridblocks and (2) natural fracture gridblocks connecting with the hydraulic fractures, a permeability value of 1.0 (mD) is used to mimic the results of stimulation. Next, DTOF maps are generated using the FMM for all the samples. Although well established for structured grid systems, for irregular grid systems like EDFMs, special treatments, such as sub-gridding, are required to compute the DTOF using the original FMM approach based on the finite difference discretization (Xue, Yang, et al. 2019a). Such special treatments are typically not straightforward and difficult to be generalized. In our application, we utilized the recently proposed finite volume based FMM that is robust and applicable to arbitrary grid systems (Chen et al. 2021). Grid geometry of one of the samples and corresponding DTOF are provided in Figure 4.4, from which we observe effects of the fractures. Specifically, while the DTOF propagates smoothly in the homogeneous matrix domain, it shows discontinuities near the hydraulic fractures due to the large conductivity contrasts as seen in the enlarged view in Figure 4.4.

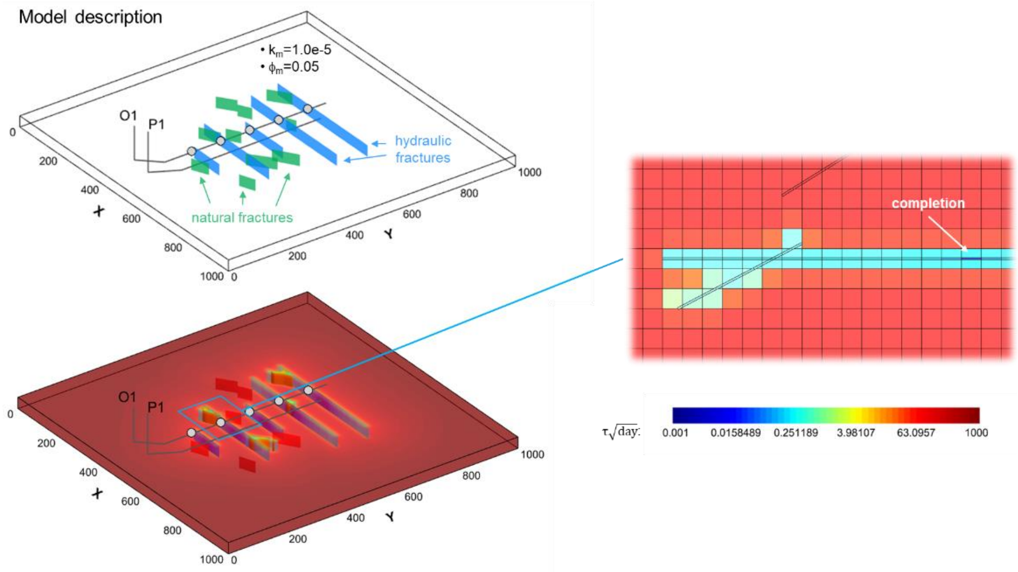

Figure 4.4 2D synthetic unconventional reservoir. Top: model domain and fracture geometry, and bottom: the DTOF map and an enlarged view (reprinted with permission from Onishi et al., 2021)

Parameter	Low	High
Hydraulic fractures (x5)		
Length, L_{HF}, (ft)	100	500
Natural fractures (x10)		
Coordinate of origin, x_0, (ft)	200	650
Coordinate of origin, y_0, (ft)	200	650
Angle (degree from horizontal line, $y=y_0$)	20	40
Length, L_{NF}, (ft)	35	100

Table 4.1 Input variables and their ranges (reprinted with permission from Onishi et al., 2021)

The FMM-based simulation. The following inputs are used together with the grid information for the FMM-based simulation. The fluids modeled in this study are described by three phase (oil, water, and gas) flow based on the publicly available data on the HFTS-I test site in the West Texas Midland Basin. The relative permeability curves are provided in Figure 4.5a, and capillary pressure is assumed to be negligible. Rock compaction effects due to depletion are described by transmissibility and pore volume multipliers shown in Figure 4.5b. The model is initialized using uniform pressure, water saturation, and gas saturation of 3,500 (psi), 0.4, and 0. The bubble point pressure is approximately 2,800 (psi), and the reservoir is initially undersaturated. The well (P1) produces fluids for 200 days with a minimum bottom-hole pressure control of 1,000 (psi).

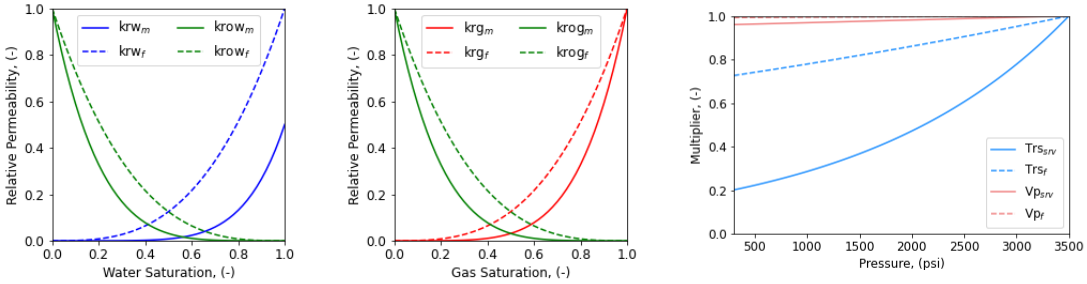

(a) (b)

Figure 4.5 (a): three phase relative permeability curves, and (b): rock compaction table. *Trs* and V_p stand for transmissibility and pore volume multipliers. The subscripts are domain indices. '*m*', '*srv*', and '*f*' stand for matrix, stimulated reservoir volume (matrix gridblock connecting with fractures), and fracture (reprinted with permission from Onishi et al., 2021).

Validation of the ROM. Before applying any ROMs, it is useful to ensure that the ROM is good approximation of the full-physics simulation. We randomly selected 100 from the 1,000 samples and compared the simulation results between the full-physics simulation and the FMM-based simulation. The average runtimes of the full physics simulation and

FMM-based simulation are roughly 70 and 30 seconds, respectively. In the FMM-based simulation workflow, there are additional steps for preprocessing (solving the Eikonal equation, Eq. (4.2) via the FMM) for which the runtime is observed to be almost negligible (~0.005 seconds). As reported by Iino, Onishi, et al. (2020), the speedup factor is expected to be more significant as the complexity of the problem increases. Comparisons of cumulative production are provided in **Appendix A**, from which an overall good agreement is obtained. We will further validate the FMM-based simulation by conducting more quantitative comparisons through the application of the relative error over the time steps,

$$\delta_j^s = \frac{\sum_{i=1}^{n_d}\left(d_i^{ref} - d_i^{FMM}\right)^2}{\sum_{i=1}^{n_d}\left(d_i^{ref}\right)^2} \tag{4.9}$$

where, δ_j^s is the relative error of sample *s*, in terms of metric *j* (=OPR, WPR, and GPR), n_d is the number of data points (time steps), d_i^{ref} and d_i^{FMM} stand for the simulation results using reference solution (full-physics simulation) and FMM-based simulation at step *i*. The overall relative error of metric *j* over the randomly selected 100 samples is computed as,

$$\delta_j = \frac{1}{n_s^{FMM}} \sum_{s=1}^{n_s^{FMM}} \delta_j^s \tag{4.10}$$

where, n_s^{FMM} is the number of samples (=100). As a result, the overall relative error values of 1.01e-5, 2.47e-5, and 3.95e-5 are obtained for OPR, WPR, and GPR. We notice here that the FMM-based simulation slightly overestimates the cumulative productions. This is because it is based on the 1D DTOF coordinate that approximates the original 2D problem. For more details on assumptions in the FMM-based simulation and potential limitations, the reader is referred to Iino (2018). Nevertheless, the relative errors are sufficiently small, validating the use of the FMM-based simulation.

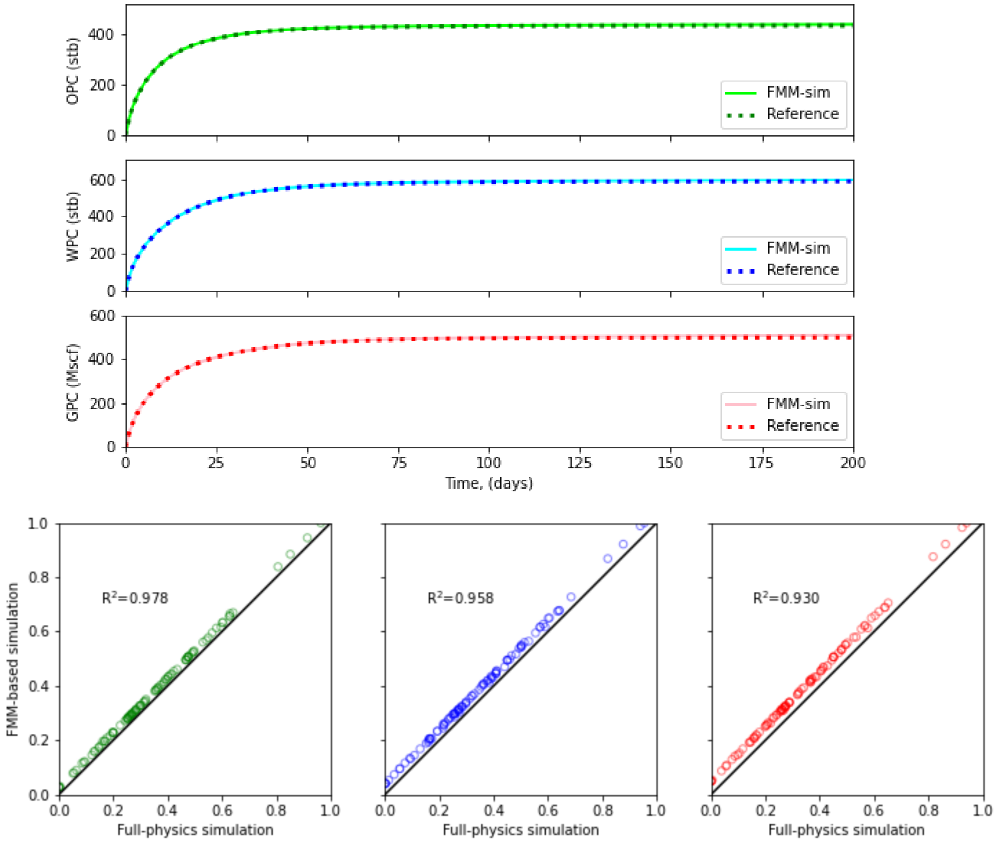

Figure 4.6 Comparisons between full-physics simulation (reference) vs FMM-based simulation. Top: cumulative production comparisons of one of the samples. Bottom: Cross-plots comparing cumulative production at the end of simulation period for the randomly selected 100 samples (reprinted with permission from Onishi et al., 2021).

Generating datasets. The FMM-based simulation is applied to all the 1,000 samples to generate datasets. The DTOF maps, multiphase production data, and pressure data at the pressure gauges along the monitoring well are saved for the subsequent steps (Figure 4.7). The use of downhole pressure data at the pressure gauges instead of flow rate data along a lateral as in Figure 4.3 is to demonstrate flexibility of the proposed workflow. An interesting observation here is that some of the samples show flat pressure responses at the gauges, whereas others show declining trends. This is because lengths of the five hydraulic fractures vary in each sample. The flat trends are observed at the pressure gauges that are not affected by hydraulic fractures. For the next steps, the samples are divided into 700, 150, and 150 for training, validation, and test, for training both an autoencoder and a regression model.

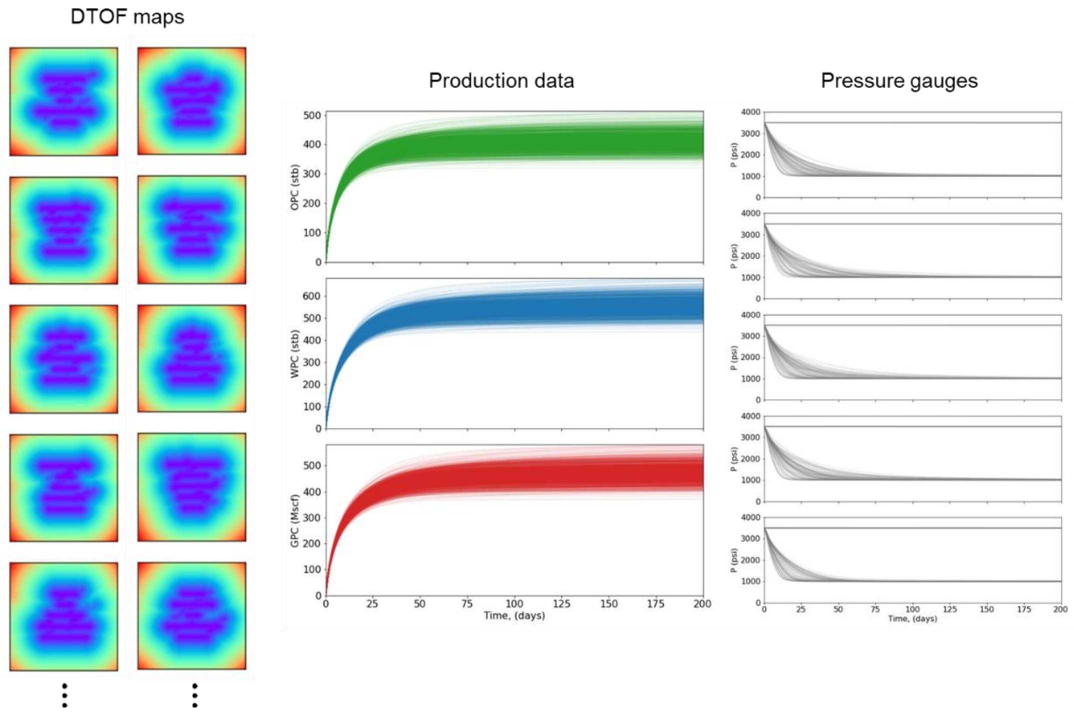

Figure 4.7 Datasets generated using the FMM-based rapid simulation (reprinted with permission from Onishi et al., 2021)

Training an autoencoder. Next step is to train an autoencoder to discover latent variables, $\boldsymbol{z}$ from high-dimensional input data. Architecture of the autoencoder includes CNNs and dense layers shown in Figure 4.8 and more detailed settings of the autoencoder are provided in **Appendix A**. We note here that, the number of active gridblocks (or pixels) has to be the same in all the samples for an autoencoder training. In the EDFM framework, fractures are discretized at boundaries of the matrix gridblocks, and the discretized fracture control volumes are connected with the matrix gridblocks via non-neighbor connections (NNCs). Therefore, the number of active gridblocks (matrix + fractures) can vary in different samples with different fracture configurations, and the raw DTOF maps are not directly applicable to an autoencoder. In our application, since our primary goal is to visualize the subsurface images, we focus on the matrix domain so that dimensions of the DTOF maps are consistent across all the samples. This is a reasonable workaround for the following reasons. First, effects of the fractures are implicitly reflected in the matrix gridblocks connecting with the fracture gridblocks. Second, the discrete fractures have very small pore volumes, and the flow inside the fractures typically does not exhibit significant impact on analyses using DTOF maps, such as the $w(\tau)$ diagnostic plot (Xue, Yang, Park, et al. 2019).

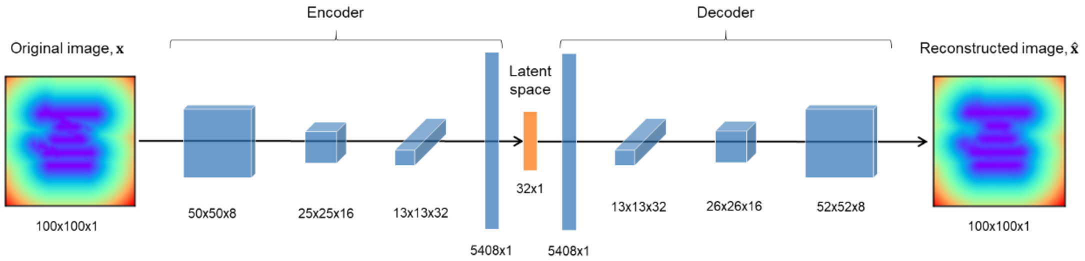

Figure 4.8 Schematic of the autoencoder (reprinted with permission from Onishi et al., 2021)

For the training, batch size of 64, the maximum number of epochs of 5,000, and patience of 50, are used. The optimization algorithm used in this study is the adaptive moment estimation (ADAM) (Kingma and Ba 2014), a commonly used gradient-based method in training deep learning models. The initial learning rate in ADAM is 0.001. The runtime for the training process was approximately 3 minutes, which had stopped at around 1200 epochs because the validation loss did not show improvement in the last 50 epochs (=patience) (Figure 4.9). The training was run on a GPU in Google Colaboratory (Bisong 2019) which is a shared GPU, the runtime is observed to be slightly different in each run depending on the available memory. The trained model is then applied to the test dataset (150 samples), and visual comparisons between the original DTOF maps and reconstructed (predicted) maps are shown in Figure 4.10. Although some small effects of natural fractures are partially not captured in the predicted DTOF maps, an overall good agreement is obtained. Additionally, the relative errors are evaluated for the test samples as,

$$\delta_\tau^s = \frac{\sum_{i=1}^{n_b^m} \left(\tau_i - \hat{\tau}_i\right)^2}{\sum_{i=1}^{n_b^m} \left(\tau_i\right)^2} \tag{4.11}$$

where, δ_τ^s is the relative error of sample s, in terms of τ, n_b^m is the number of the matrix gridblocks (not the total number of active gridblocks including fractures). Then, the overall relative error over the 150 test samples is computed as,

$$\delta_\tau = \frac{1}{n_s^{test}} \sum_{s=1}^{n_s^{test}} \delta_\tau^s \tag{4.12}$$

n_s^{test} is the number of test samples (=150). As a result, an overall relative error of 2.81e-4 is obtained. The low value indicates successful training of the autoencoder.

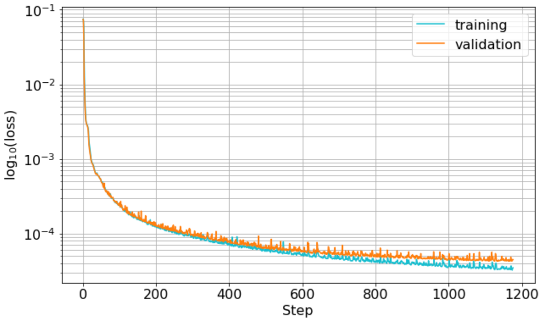

Figure 4.9 Model loss on training and validation datasets (autoencoder) (reprinted with permission from Onishi et al., 2021)

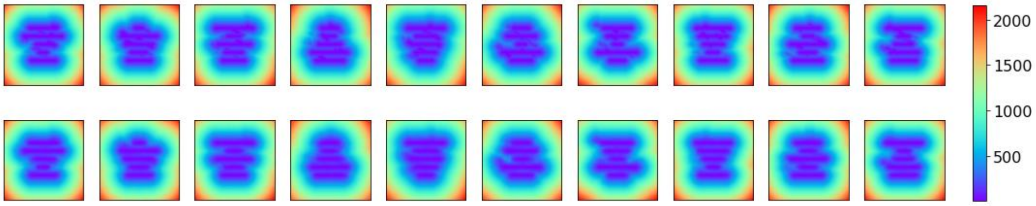

Figure 4.10 Visual comparison of DTOF maps between randomly selected 10 samples among the 150 test samples (top), and corresponding reconstructed DTOF maps ($\sqrt{\text{days}}$) using the trained autoencoder (bottom) (reprinted with permission from Onishi et al., 2021)

Training a regression model. Next, a regression model is trained using a simple feedforward neural network and the same training and validation datasets. Its architecture is shown in Figure 4.11, and more detailed settings can be found in **Appendix A**. The ADAM optimizer with the same settings as the autoencoder training is applied, and the result of the minimization is provided in Figure 4.12. With the simple architecture, runtime for the training was less than one minute. Again, the relative error for the regression model was computed as follows,

$$\delta_z^s = \frac{\sum_{i=1}^{n_z}\left(z_i - \hat{z}_i\right)^2}{\sum_{i=1}^{n_z}\left(z_i\right)^2} \tag{4.13}$$

where, δ_z^s is the relative error of sample s, in terms of z, n_z is dimension of the latent space (=32). Then, the overall relative error over the 150 test samples is,

$$\delta_z = \frac{1}{n_s^{test}} \sum_{s=1}^{n_s^{test}} \delta_z^s \tag{4.14}$$

As a result, we obtained the relative error of 5.57e-2. For both the autoencoder and the regression model, multiple combinations of hyperparameters (model architecture, activation function, batch size, learning rate, etc.) were tested, and the ones that showed the best performance (minimum validation loss) were used. The models could be further improved by exploring the hyperparameter space (Bergstra and Bengio 2012), and this will be investigated in our future work.

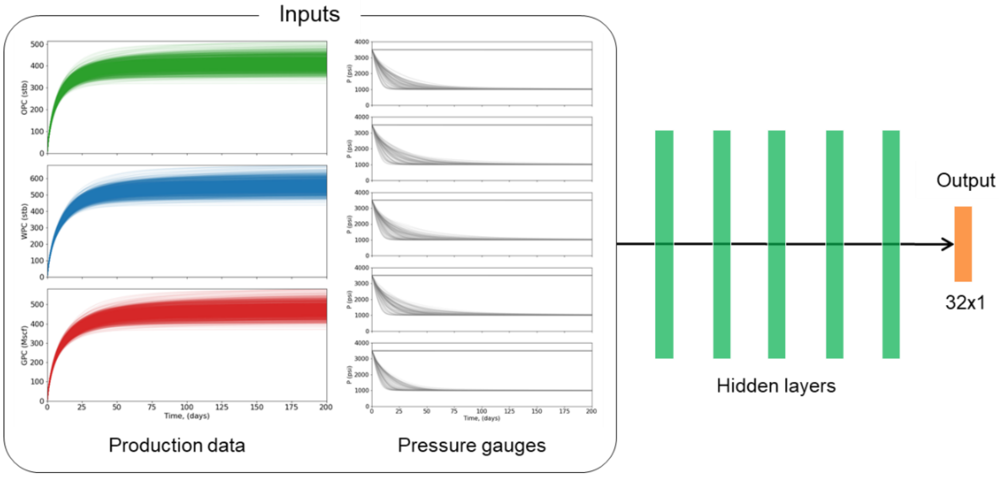

Figure 4.11 Architecture of the regression model (reprinted with permission from Onishi et al., 2021)

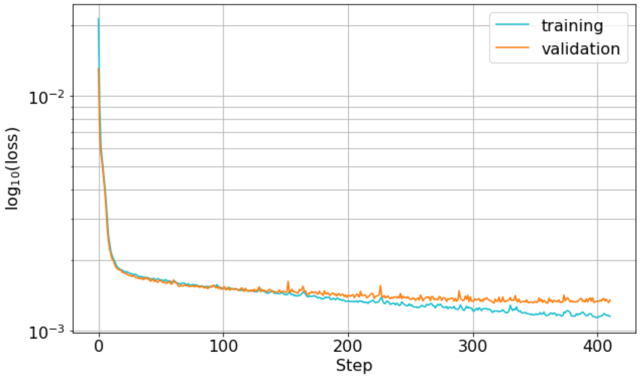

Figure 4.12 Model loss on training and validation datasets (regression model) (reprinted with permission from Onishi et al., 2021)

Prediction (blind-test). The trained regression model and the decoder are combined to build a hybrid model that predicts DTOF maps given measured data. The hybrid model is applied to measured data from one of the test samples. A comparison between the predicted DTOF map and the true DTOF map is shown on the right hand side in Figure 4.13, from which the predicted DTOF visually shows good agreement with the true DTOF. We notice here that the 3rd hydraulic fracture is shorter than the others. This observation is consistent with the measured data at the pressure gauges, where only the 3rd gauge shows flat pressure throughout the simulation period, meaning that the 3rd fracture did not reach the 3rd gauge. The relative error between the predicted DTOF and true DTOF maps (Eq. (4.11)) is 1.44e-3. In addition, the hybrid model was applied to all the 150 test samples. Visual comparisons of DTOF maps are provided in Figure 4.14 where we can confirm similar trends between the true DTOF maps and the predicted maps. Furthermore, we evaluated the overall relative error over the test samples using Eq. (4.12) and obtained a value of 3.52e-3, validating the hybrid model.

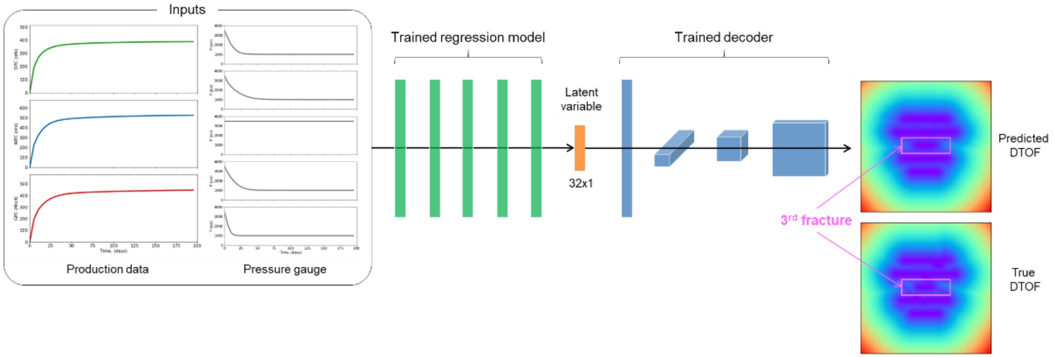

Figure 4.13 Architecture of the hybrid model (reprinted with permission from Onishi et al., 2021)

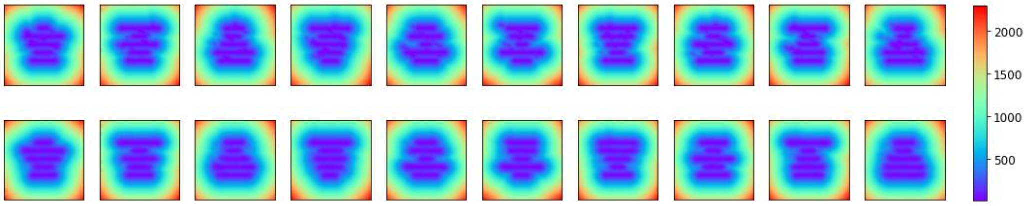

Figure 4.14 Visual comparison of DTOF maps between randomly selected 10 samples among the 150 test samples (top), and corresponding predicted DTOF maps ($\sqrt{\text{days}}$) using the hybrid model (bottom) (reprinted with permission from Onishi et al., 2021)

Let us consider a situation where the measured data shown in left side in Figure 4.13 is available. We predicted a single DTOF map using the hybrid model. At this point, the prediction is deterministic, and we would like to obtain multiple plausible realizations of DTOF maps to account for subsurface uncertainty. In our approach, we aim to find samples among the training and validation datasets that are similar to the predicted DTOF map. To this end, multidimensional scaling (MDS) is applied. MDS is a technique to translate a dissimilarity matrix consisting of pair-wise dissimilarities between individuals associated with high-dimensional data into a configuration of points in n-D Euclidian space (Borg and Groenen 2005). The visually intuitive representation of the individuals in a low dimensional map is useful for understanding dissimilarities between them. In the context of subsurface modeling, MDS has found many applications, for example, uncertainty quantification in reservoir performance (Scheidt and Caers 2009). In our application, we utilized MDS to map the training and validation samples together with the test case into a low dimensional (2D) space, whereby the measure of dissimilarity to compute a dissimilarity matrix is values of the latent variables ($\mathbf{z}$) associated with each of the samples. The resultant 2D map through the application of MDS is provided in Figure 4.15, in which each point represents a sample, and distances between points indicate dissimilarities between the samples, in terms of the values of latent variable ($\mathbf{z}$). As seen here, DTOF maps associated with the points that are far away from each other show quite different characteristics. In contrast, similar DTOF maps are obtained from the nearest neighbors (red points) of the test case (×). The nearest neighbors can be viewed as multiple plausible realizations of subsurface images in this example and can be utilized for a variety of applications. For example, the visualizations can help engineers design field development strategies, such as well and completion spacing for infill wells. Also, the DTOF maps can be utilized as a 1D spatial coordinate (Figure 4.1) to perform rapid simulations for the multiple scenarios.

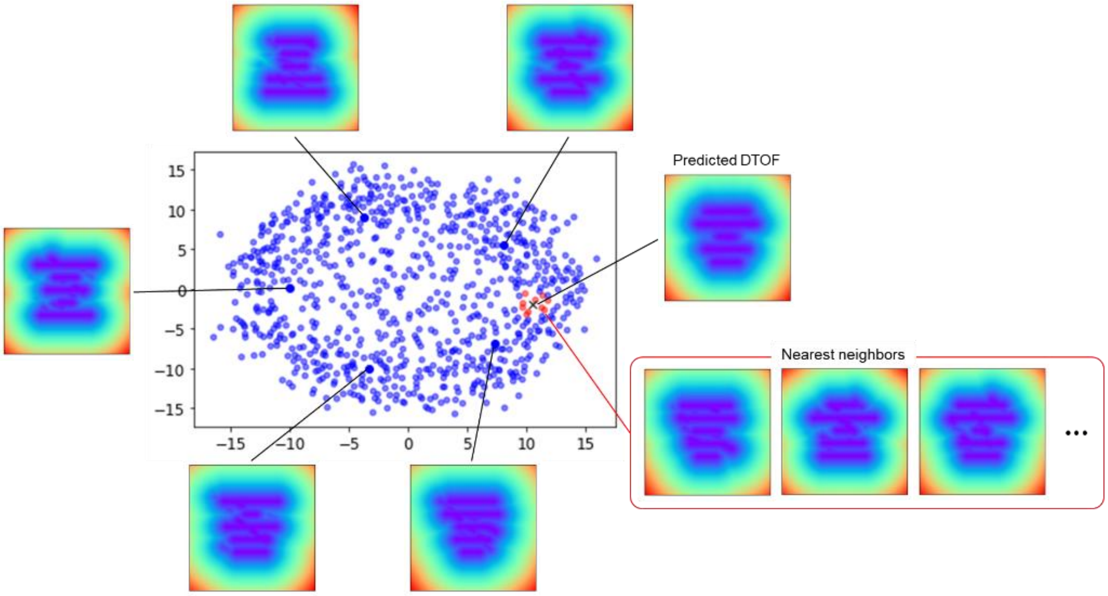

Figure 4.15 2D MDS space where each point represents a sample (reprinted with permission from Onishi et al., 2021).

Furthermore, we will demonstrate the utility of our approach using another scenario where the pressure gauges are not available. In this case, the regression model was trained solely based on the production data and then was combined with the trained decoder. Subsequently, the hybrid model was used to predict a DTOF map given the production data from the same test sample as shown in Figure 4.16. As opposed to the previous scenario, the predicted DTOF map shows much larger discrepancies compared with the true DTOF map (the relative error of DTOF is 1.20e-2). This observation suggests that the pressure gauges provide valuable information for understanding the subsurface. Although this conclusion is foreseeable in this simple exercise, the workflow is flexible and applicable to various scenarios and is a useful tool to evaluate different data-acquisition programs. That is, the workflow allows us to ask questions like “should we install pressure gauges? If so, where and how many of them do we need?” This can be quickly answered by training multiple regression models (step 5 in Figure 4.3) with varying availability and locations of the gauges (typically takes less than one minute each), then evaluating the performance of the hybrid model. Since the dynamic pressure responses at different locations in the reservoir can be readily accessible from the existing simulation outputs (step 2 in Figure 4.3), locations of the gauges do not have to be the same as the five gauges in the example. Also, the data type is not limited to pressure responses. Any data type, as long as it is available in outputs or inputs of the simulator, can be readily incorporated in the workflow. Optimal combinations of types and amount of data to be collected and resultant uncertainty reduction can be systematically found. For example, we can solve a minimization problem, where the regression is a forward model, and the objective function consists of a test error term for DTOF maps and is simultaneously penalized as cost of the measurements increases. The workflow can be further enhanced by incorporating more elegant approaches for uncertainty quantification (e.g., He, Sarma, et al. (2018)) or sensor placing optimization (Manohar et al. 2018). We leave these potential applications for future work.

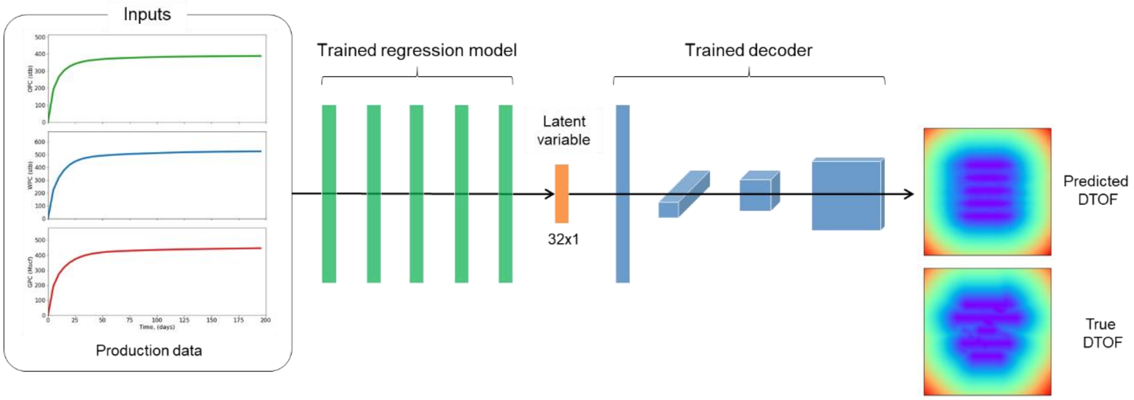

Figure 4.16 Architecture of the hybrid model. Inputs consist of production data only (reprinted with permission from Onishi et al., 2021).

4.4 Field Application

In this section, we present an application of our approach to a field-scale unconventional reservoir. The case is sufficiently realistic to demonstrate practicality of the proposed approach.

Case Description. The case is built after a field-based hydraulic fracturing research program in the West Texas Midland Basin, the HFTS-I (Ciezobka and Reeves 2021). The primary targets of the study are eleven horizontal wells with 400+ stages drilled in upper and middle Wolfcamp formation. A variety of collected field data, such as core data and microseismic surveys, has been made publicly available by the operaters. In our application, we focus on one of the wells, and built a sector geologic model (Figure 4.17a). The size of the model is 1,886.5×11,237×618 ft^3 with 23×137×47 grid discretization for the matrix domain. More than 100 hydraulic fractures are added on top the matrix domain via the EDFM approach, and their extent and orientations are based on the available microseismic data (Maity 2018, Stegent and Candler 2018). The fluid model is the same as the one in the previous example case. For the matrix domain, homogeneous permeability and porosity (k_m=0.05 nD and ϕ_m=0.05) are assumed, and uniform values of 3000 psi, 0.3, 0, and 0.987 are assigned for initial pressure, water saturation, gas saturation, and solution gas-oil-ratio. These values on the gridblocks are based on the available data and a previous simulation study (Forrest et al. 2018). The bubble point pressure is approximately 2,800 (psi), and therefore the reservoir is initially undersaturated. In addition, since little observed data during production phase is available, synthetic observed data, including multiphase production and bottom-hole pressure data for 150 days, is generated (Figure 4.17b).

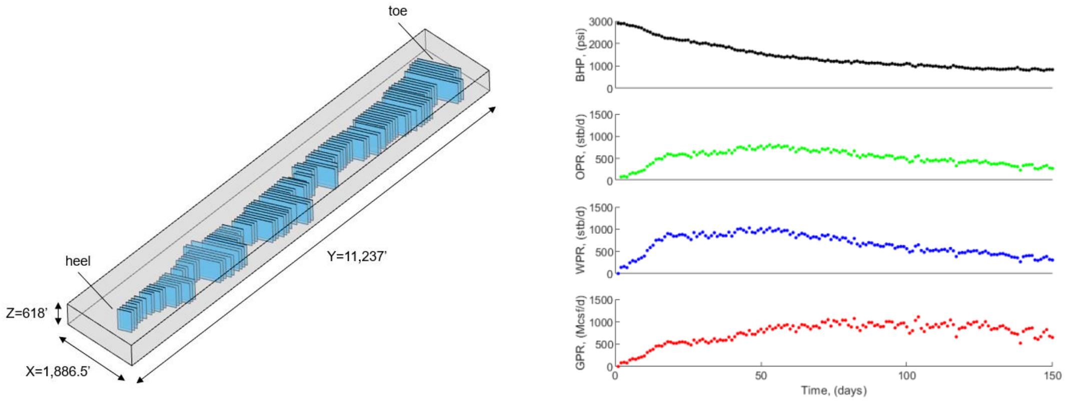

(a) (b)

Figure 4.17 (a) Field-scale reservoir with 100+ hydraulic fractures described by EDFMs and (b) the observed data (reprinted with permission from Onishi et al., 2021)

Parameterization. The first step is to identify an initial set of parameters that are thought to be influential on the observed data, and their distribution and ranges as shown in Table 4.2. There are two regions: hydraulic fractures and stimulated reservoir volume (SRV). The SRV region is defined as matrix gridblocks connecting with fracture gridblocks via non-neighbor connections (NNCs), whereas the hydraulic fracture regions are simply the hydraulic fracture gridblocks. This means that the SRV region varies in each realization with different fracture geometries. The hydraulic fractures described by the EDFMs (Figure 4.17) correspond to propped regions that are part of the estimated fracture extents based on the microseismic data at HFTS-I and its interpretation (Stegent and Candler 2018). Lengths (horizontal extent and height) of the fractures are parameterized by a uniform multiplier that corresponds to fraction of the propped region. Properties of the fractures including their conductivity and porosity are also considered. The effects of stimulation near the fractures, such as small natural fractures connecting with the hydraulic fractures, are represented as effective gridblock permeability at the SRV region, to which a uniform permeability multiplier is applied. For both fracture and SRV domain, uniform values of high initial water saturation are assigned to mimic the effects of fracturing treatments. In addition, rock compaction effects due to depletion are described by transmissibility and pore volume multipliers (Raghavan and Chin 2002, Park et al. 2021),

$$TRMULT_j = \exp\left(-b\Delta P\right) \tag{4.15}$$

and,

$$PVMULT_j = \left(\frac{1}{c_{pp}}\ln\left(TRMULT_j\right)+1\right) \tag{4.16}$$

where, $TRMULT_j$ is transmissibility multiplier for region j (fracture or SRV), b_j is the transmissibility multiplier coefficient that corresponds to values of *TRMULT* in Table 4.2 for region j, $\Delta P = P_{ini}-P$, *PVMULTj* is pore volume multiplier for region j, and c_{pp} is pore volume multiplier coefficient (*PVMULT* in Table 4.2). In this application, the three phase relative permeability functions for the two regions are modeled according to the Brooks-Corey function (Brooks and Corey 1964) defined as,

$$k_{rw} = k_{rw}^0 S_w^{n_w}; k_{row} = k_{row}^0\left(1-S_w\right)^{n_{ow}} \tag{4.17}$$

$$k_{rg} = k_{rg}^0 S_g^{n_g}; k_{rog} = \left(1-S_g\right)^{n_{og}} \tag{4.18}$$

where, the normalized water and gas saturations are given by,

$$S_w = \frac{S_w - S_{wc}}{1-S_{orw}-S_{wc}}; S_g = \frac{S_g}{1-S_{org}-S_{wc}} \tag{4.19}$$

The three phase oil relative permeability is then computed as,

$$k_{ro} = \frac{S_g k_{rog} + \left(S_w - S_{wc}\right) k_{row}}{S_g + S_w - S_{wc}} \tag{4.20}$$

where, the residual and connate saturations are assumed to be zero. Also, end-points of the relative permeabilities are 1.0 except for the water relative permeability for the matrix (water-wet). These setting are based on the laboratory experiments on core samples obtained from the Wolfcamp formation (Ojha et al. 2018). For the sensitivity study, we will focus on the exponents and end-point water relative permeability for the matrix. An example of rock compaction tables and relative permeability curves is provided in Figure 4.5.

Parameter	Symbol	Low	Base	High	Distribution
Hydraulic fractures (HF)					
Length multiplier, (-)	HF_LENGTH	0.2	0.35	0.5	Uniform
Conductivity, (mD-ft)	HF_COND	10	60	100	Uniform
Porosity, (-)	HF_PORO	0.05	0.1	0.2	Uniform
Transmissibility multiplier coefficient, (psi^{-1})	HF_TRMULT	-5	-4	-3	Uniform (log_{10})
Initial water saturation, (-)	HF_SWI	0.5	0.7	0.9	Uniform
Water relative permeability exponent, (-)	HF_KRWN	1	3	5	Uniform
Oil-water relative permeability exponent, (-)	HF_KROWN	1	3	5	Uniform
Gas relative permeability exponent, (-)	HF_KRGN	1	3	5	Uniform
Gas-oil relative permeability exponent, (-)	HF_KROGN	1	3	5	Uniform
SRV					
Permeability multiplier, (-)	SRV_KMULT	3	5	7	Uniform (log_{10})
Transmissibility multiplier coefficient, (psi^{-1})	SRV_TRMULT	-4.3	-3.3	-2.3	Uniform (log_{10})
Initial water saturation, (-)	SRV_SWI	0.3	0.45	0.6	Uniform
End point water relative permeability, (-)	SRV_KRWEP	0.3	0.5	0.7	Uniform
Water relative permeability exponent, (-)	SRV_KRWN	4	8	12	Uniform
Oil-water relative permeability exponent, (-)	SRV _KROWN	2	5	8	Uniform
Gas relative permeability exponent, (-)	SRV _KRGN	2	5	8	Uniform
Gas-oil relative permeability exponent, (-)	SRV _KROGN	2	5	8	Uniform
HF & SRV					
Pore volume multiplier coefficient in rock compaction table, (-)	PVMULT	30	40	80	Uniform

Table 4.2 Identified uncertain parameters and their ranges for the field-scale unconventional reservoir (reprinted with permission from Onishi et al., 2021)

While we have defined the parameters for large-scale updates, such as uniform multipliers, in Table 4.2, we eventually would like to consider more local information like stage-level hydraulic fracture lengths. To this end, we follow a two-step hierarchical approach. First, we perform large-scale updates of the reservoir properties in Table 4.2 by integrating the observed production data into the reservoir model using the multi-objective genetic algorithm (MOGA). The history matched reservoir model and reduced uncertainties of the parameters will be the starting point of the next step which involves sampling of the influential parameters (step 2 in Figure 4.3). The parameters for the sampling include two categories: (1) lengths of the hydraulic fractures, and (2) parameters whose uncertainties remained relatively high even after history matching, if any exist. For the other parameters, whose uncertainties are found to be sufficiently reduced after history matching, values from the best individual with the smallest objective function values will be used for all the samples. The subsequent steps are the same as the example case discussed before.

Sensitivity Analysis. A one-variable-at-a-time design is applied to generate tornado plots shown in Figure 4.18. The simulations are carried out with bottom-hole pressure constraint based on the observed data, and therefore the metrics of the objective functions are OPR, WPR, and GPR (Eq. (4.5)). As a result, majority of the parameters for the hydraulic fractures and two parameters among the parameters for the SRV region including permeability multiplier and initial water saturation are found to be sensitive, and these will be used during history matching.

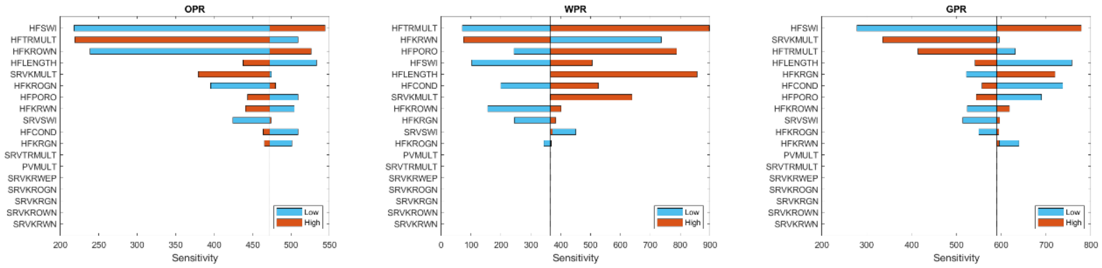

Figure 4.18 Tornado plots showing the results of the sensitivity analysis (reprinted with permission from Onishi et al., 2021)

Validation of the ROM. While the 3D flow simulations were used in the sensitivity analysis, running hundreds or thousands of them for history matching can be computationally expensive. Instead, the FMM-based rapid simulation will be used to accelerate the workflow. In this section, we validate the accuracy of the FMM-based simulation by comparing with 3-D simulation results for the 37 samples used in the sensitivity analysis (high and low cases for 18 parameters plus the base case). The comparisons are summarized in Figure 4.19, in which there are excellent agreements between the two methods. Furthermore, the overall relative errors with respect to OPR, WPR, and GPR are 8.58e-6, 9.44e-6, and 1.34e-6, respectively. These observations validate the use of the FMM-based simulation approach. We notice here that the accuracy is better than the example case (Figure 4.6). This may be because of the absence of natural fractures in this case. The runtime of the FMM-based simulations is 2-3 minutes on average, which is roughly 5 fold reduction compared to the 3D simulation. The speedup factor becomes more evident as size and complexity of the problem increases.

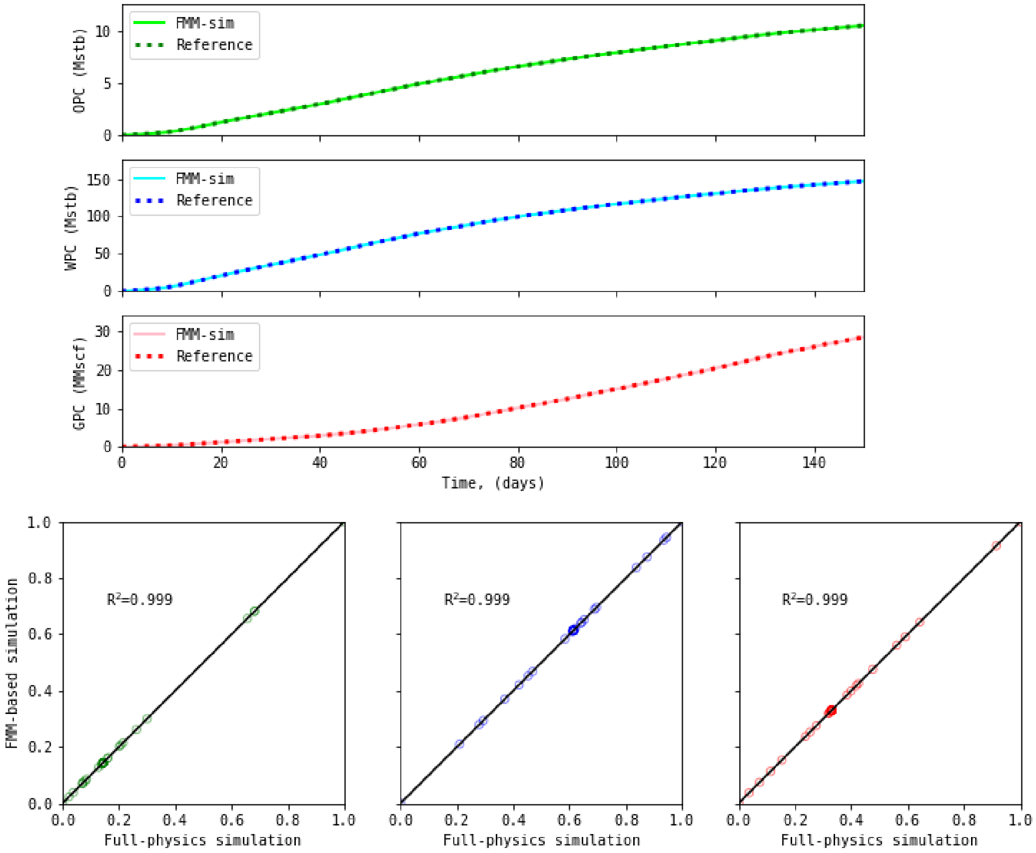

Figure 4.19 Comparisons between full-physics simulation (reference) vs FMM-based simulation. Top: cumulative production comparisons of one of the samples. Bottom: Cross-plots comparing cumulative production at the end of simulation period for the 37 samples used in the sensitivity analysis (reprinted with permission from Onishi et al., 2021)

Global history matching. Reservoir model calibration is performed using the MOGA (Park et al. 2013) to update the 11 sensitive parameters identified from the sensitivity analysis. Three objective functions are defined as misfits between the observed data and simulated responses, as described in Eq. (4.5) where the metric j = OPR, WPR, and GPR. In our application, first 120 days of the observed data is used to compute the objective functions, whereas the rest (30 days) will be used for validation. The MOGA was run for 30 generations with a population size of 50, and the results are provided in Figure 4.20.

We see that values of the objective functions are decreasing as generation advances (Figure 4.20a). Also, trends of the observed data are well captured by the updated individuals (Figure 4.20b). At the same time, a satisfactory reduction in uncertainties was obtained for most parameters, as shown in Figure 4.21. We notice here that uncertainties of certain parameters including fracture conductivity and the exponents for the water-oil relative permeability curves for the hydraulic fractures remained relatively high even after history matching.

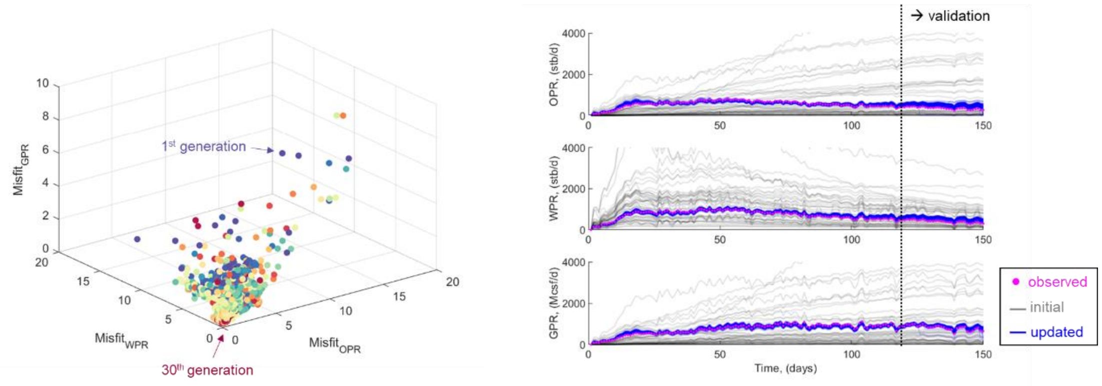

(a) (b)

Figure 4.20 Results of the history matching. (a) objective function reduction with generation and (b) flow response comparisons before and after the history matching (reprinted with permission from Onishi et al., 2021)

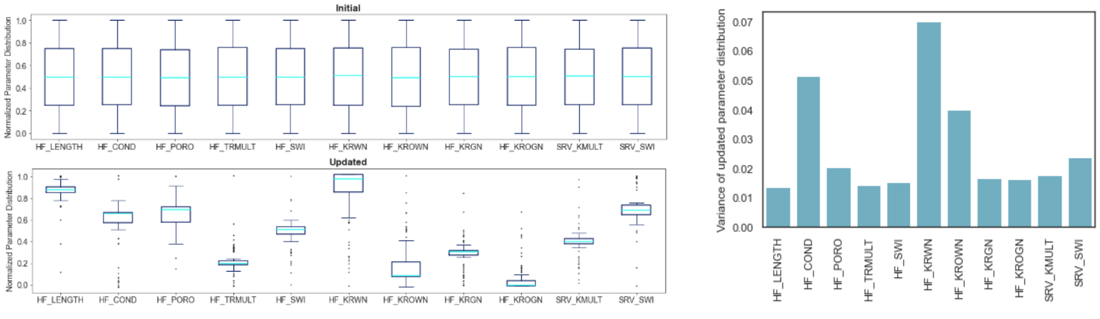

(a) (b)

Figure 4.21 (a) Box-plots of normalized parameter distributions and (b) a bar chart showing variance of each of the parameters after history matching (reprinted with permission from Onishi et al., 2021)

Following Figure 4.3, the next step is to conduct sampling. The parameters of interest include the three relatively uncertain parameters from the history matching results (HF_COND, HF_KRWN, and HF_KROWN), and lengths of the hydraulic fractures. According to the available data, there are 37 stages along the lateral, and 11 of them are representative stages (Figure 4.22), at which measurement errors are minimal, and the data exhibits high confidence (Warpinski 2009, Stegent and Candler 2018). The parameters for the hydraulic fractures will be stage-level length multipliers [0.75 1.25] for each of the representative stages (×11). Subsequently, 2000 samples were generated through the application of a Latin hypercube design.

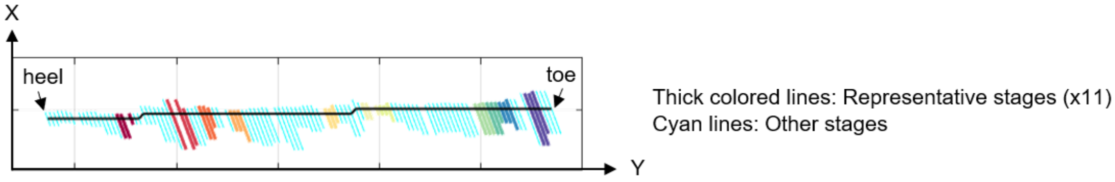

Figure 4.22 Schematic of the lateral with hydraulic fractures (reprinted with permission from Onishi et al., 2021)

Generating datasets. The FMM-based simulation is applied to all the 2000 samples to generate datasets. The simulations are constrained by the observed bottom-hole pressure. The DTOF maps, multiphase production data, and distributed flow rate data along the lateral at a certain time, which can be obtained from production logging tools in practice, are saved for the trainings as shown in Figure 4.23. In regard to multiphase production responses, we observe wider ranges in oil and water production than gas production. This is likely because the exponents for oil-water relative permeability curves are the parameters of interest, whereas fixed oil-gas relative permeability curves are used for all the samples. The other observation here is that the flow rate profiles show higher values at stages with longer length, because of greater surface area of the hydraulic fractures. The samples are divided into 1400, 300, and 300, for training, validation, and test, respectively.

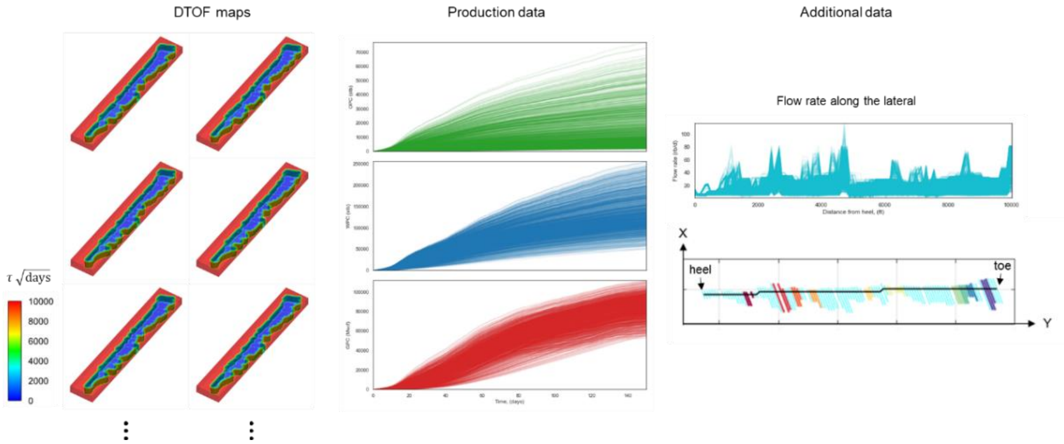

Figure 4.23 Datasets generated using the FMM-based rapid simulation for the field-scale application (reprinted with permission from Onishi et al., 2021)

Training an autoencoder. Next, we trained an autoencoder. Architecture of the autoencoder includes CNNs and dense layers as shown in Figure 4.24, and more detailed settings are provided in **Appendix A**. In contrast to the 2D example case, 3D CNNs that are typically used with 3D image data, such as images from computerized tomography (CT) scans (Zheng et al. 2020), are employed for the 3D DTOF maps.

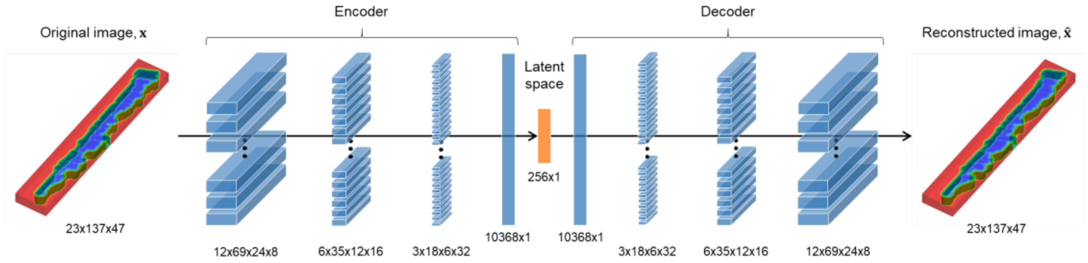

Figure 4.24 Schematic of the autoencoder for the field-scale application (reprinted with permission from Onishi et al., 2021)

For the training, batch size of 256, the maximum number of epochs of 10,000, and patience of 50, are used. The other settings and the procedures are the same as the example case. The runtime for the training process was approximately 110 minutes, which had stopped at around 4800 epochs (Figure 4.25). The increased runtime compared to the example case is because of the large and more complex neural network architecture, resulting in more parameters (weights and biases) to be tuned during the training. The trained model is then applied to the test dataset (300 samples), and visual comparisons between the original DTOF maps and reconstructed maps are shown in Figure 4.26, and an overall relative error of 4.92e-3 is obtained. Although it is difficult to visually verify if the reconstructed 3D images are close enough to the original 3D images in Figure 4.26, the low relative error value validates accuracy of the trained autoencoder.

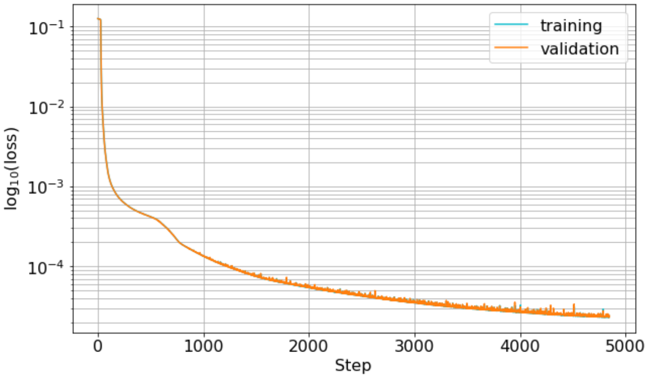

Figure 4.25 Model loss on training and validation datasets (autoencoder) (reprinted with permission from Onishi et al., 2021)

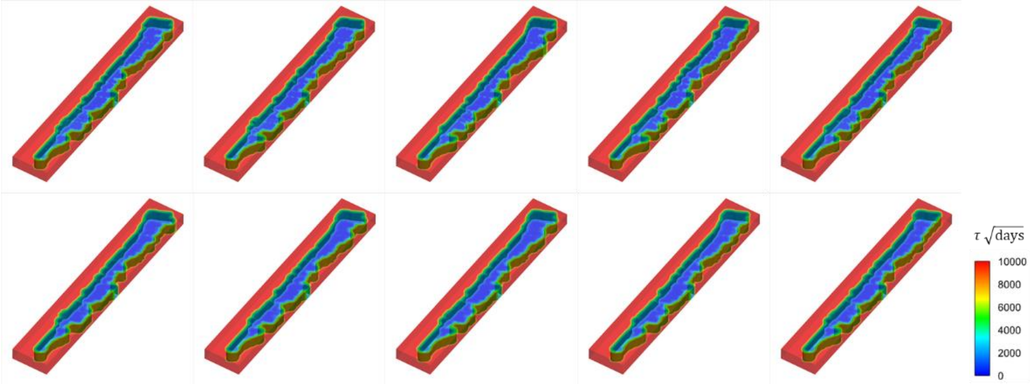

Figure 4.26 Visual comparison of DTOF maps between randomly selected 5 samples among the 300 test samples (top), and corresponding reconstructed DTOF maps using the trained autoencoder (bottom) (reprinted with permission from Onishi et al., 2021)

Training a regression model. Next, a regression model is trained. Architecture of the model is displayed in Figure 4.27. In this application, the dimensions of the input data are different, specifically, the dimensions of the production data and the distributed flow rate data correspond to the number of time steps and the number of data points along the lateral. To accommodate the two different data types, two separate input layers are used for each of them. The input layers are connected with the intermediate layers that will be concatenated to form a single hidden layer connected with a set of other hidden layers. More details of the architecture are provided in **Appendix A**. The training procedure is the same as the example case and is finished at around 150 epochs, as shown in Figure 4.28. The runtime was approximately 38 seconds.

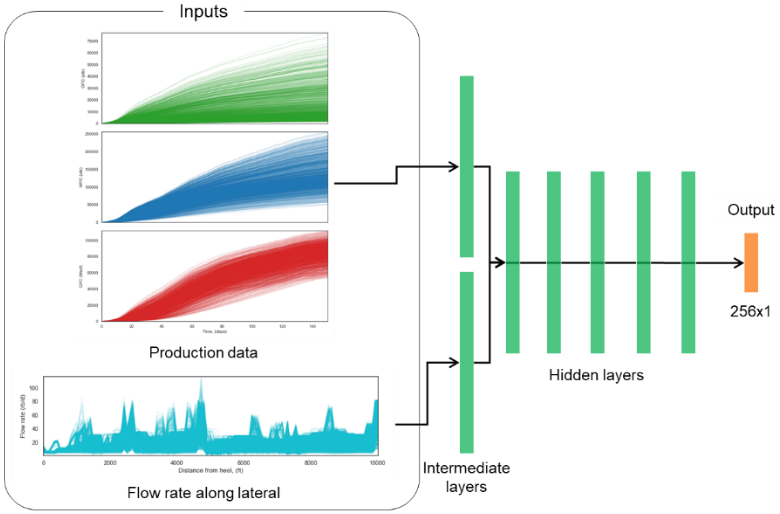

Figure 4.27 Architecture of the regression model (reprinted with permission from Onishi et al., 2021)

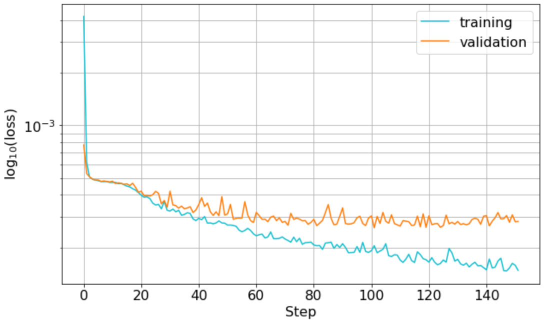

Figure 4.28 Model loss on training and validation datasets (regression model) (reprinted with permission from Onishi et al., 2021)

Prediction (blind-test). Finally, the trained regression model and the decoder are combined to build a hybrid model. The hybrid model is applied to measured data from one of the test samples. Figure 4.29 shows architecture of the model and a comparison between the predicted DTOF map and the true DTOF map. The predicted DTOF map visually shows good agreement with the true DTOF. The relative error between the predicted DTOF and true DTOF maps (Eq. (4.11)) was 1.93e-3. In a similar manner as the example in Figure 4.15, MDS is applied to the training and validation samples, and the test sample, and the resultant 2D MDS map is shown in Figure 4.30. The data points in close proximity to the × in the figure (red points) indicate similarity of the latent variables ($\mathbf{z}$) for the DTOF maps. In contrast, data points that are located further apart have very little similarity, especially within the circled region of the DTOF maps. As demonstrated above, the proposed workflow is applicable to 3D field scale unconventional reservoirs. The outcome of the workflow (DTOF maps) can be utilized for various applications including visualization, rapid simulations, and uncertainty quantification.

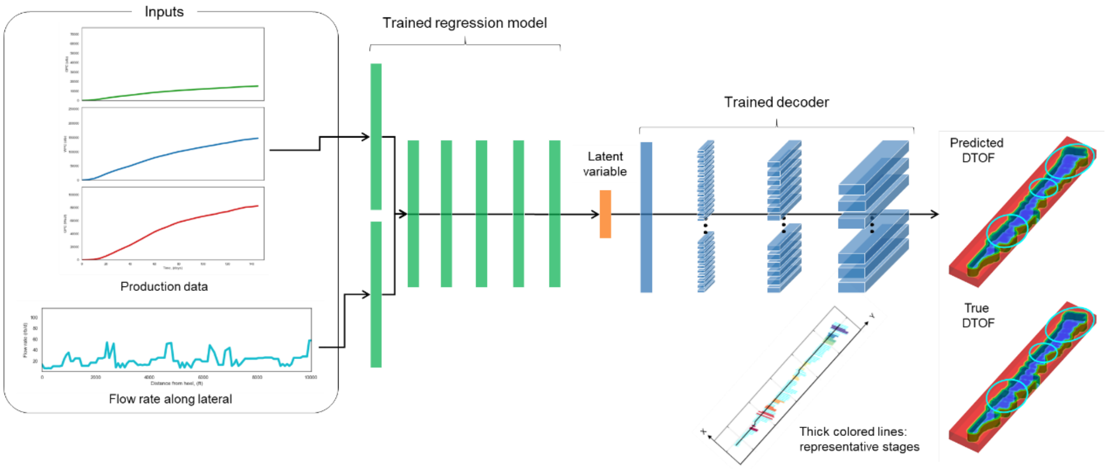

Figure 4.29 Architecture of the hybrid model for the field-scale application (reprinted with permission from Onishi et al., 2021)

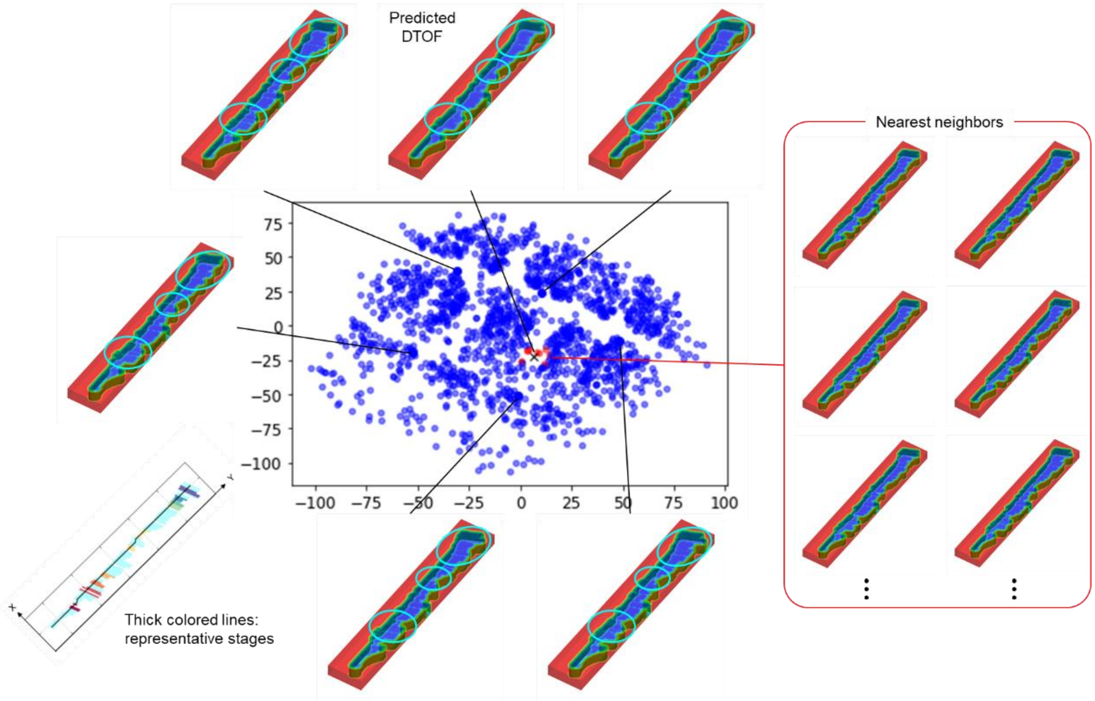

Figure 4.30 2D MDS space where each point represents a sample (reprinted with permission from Onishi et al., 2021).

4.4 Conclusion

We presented a deep learning-based workflow incorporating the FMM-based rapid simulation. The workflow has been successfully applied to a synthetic 2D case and a 3D field-scale case. From the discussions made, the following conclusions can be drawn.

- A novel deep learning-based workflow that can efficiently visualize subsurface flow has been developed. The approach incorporates the FMM-based rapid simulation and the concept of DTOF to accelerate the workflow. Specifically, generating training datasets can be efficiently done by using the FMM-based rapid simulation, and the use of DTOF allows us to use a simple architecture of the deep learning-based models. The dimensionality reduction via an autoencoder further enhances the workflow.

- The workflow has been demonstrated with a 2D illustrative example. We introduced potential applications of the approach, including the post-processing using MDS to account for uncertainties and the workflow that can be used to evaluate data acquisition programs.
- We applied the proposed approach to a 3D field scale unconventional reservoir involving more than 100 hydraulic fractures. The reservoir model was built after the publicly available data on the HFTS-I test site. The successful application demonstrated the robustness and efficacy of the approach. While we focused on the sector model encompassing a single horizontal well, the workflow can be extended to full field with multiple wells.
- The flexibility of the approach has been demonstrated using the two cases with different types of measured data. Specifically, the 2D case entails multiphase production data and pressure responses at the pressure gauges, whereas the 3D case has multiphase production data and distributed flow rate data along the lateral. The workflow can be readily extended to incorporate other data type, as long as it is available in inputs or outputs of the simulator.
- Since our primary focus in this work is to demonstrate the new workflow, relatively simple methods were used. The parameter screening procedure could be improved by using more sophisticated statistical analysis, such as *t*-tests, instead of the one-variable-at-a-time design. For deep learning models, we adopted an autoencoder and a simple feedforward neural network. The use of more advanced architecture, such as a variational autoencoder or a generative adversarial network, can potentially further

improve the workflow. Also, the models could be optimized by exploring the hyperparameter space. In addition, post-processing using MDS could be enhanced by incorporating some kernel methods to transform the Euclidian space.

CHAPTER V

CONCLUSIONS AND RECOMMENDATIONS

5.1 Chapter Summary

We have presented extensions of the Fast-Marching Method (FMM)-based rapid simulation workflow and a variety of applications. In this chapter, we discuss the conclusions reached and provide recommendations for future research.

5.2 Conclusions

In the 2nd Chapter, an extension of the FMM-based rapid simulation workflow accounting for gravity was proposed. Based on the study, the following conclusions are drawn.

- The proposed approach accounts for gravity effects and multiphase flow within hydraulic fractures by treating hydraulic fractures and a matrix domain separately. While 3-D problems in a matrix domain are transformed into 1-D problems along the DTOF, original 2-D gridblocks are retained for the hydraulic fracture planes. After the coordinate transformation via the DTOF, connections between the 1-D matrix domain and the hydraulic fractures are described by NNCs. These changes are relatively minor and can be easily implemented into an existing FMM-based rapid simulation workflow.
- The implementation has been benchmarked with a full-physics model with good agreement for synthetic and field scale cases.

- Through the simulation studies, we found that the effect of gravity is less significant in cases involving hydraulic fracture gridblocks with infinite conductivities. This is likely because all the hydraulic fracture planes deplete almost instantly and uniformly as soon as the well starts production. On the other hand, flow within hydraulic fractures planes can be more complex (heterogeneous) in finite conductivity hydraulic fracture cases. The proposed approach is well suited for such scenarios.
- In the field scale application, the proposed approach has been shown to be capable of capturing the effect of gravity and multiphase flow in the hydraulic fracture planes while maintaining computational efficiency of the rapid FMM-based simulation workflow.

Next, we introduced the robust FMM approach based on finite-volume discretization of the Eikonal equation. The proposed approach is dependent on pore volume and connections (transmissibilities) between gridblocks, rather than grid geometry as in the previously proposed finite-difference-based FMM approaches, and it is readily applicable to arbitrary finite-volume grid systems. This work addresses a major limitation of the prior FMM approaches for irregular grid systems, which is the need of the special treatments, such as sub-gridding, making it difficult to generalize. On the basis of discussions in the 3rd Chapter, we draw the following conclusions.

- The implementation has been first validated using simple homogeneous cases. Excellent agreements in terms of DTOF maps and the $V_p(\tau)$ and $w(\tau)$ diagnostic plots were obtained between the proposed approach and the analytical solution.

- The robustness and efficacy of the approach have been demonstrated through the applications of the approach to a variety of grid systems, including structured grids, EDFMs, DPDK, as well as unstructured PEBI grids, at varying levels of complexity. The finite-volume framework is compatible with commonly used commercial reservoir simulators.
- The existing FMM applications, such as the FMM-based simulation and the $V_p(\tau)$ and $w(\tau)$ diagnostic plots can be enhanced by incorporating the proposed approach within the workflow.

Finally, an efficient deep learning-based workflow for subsurface imaging in unconventional reservoir is presented. Our approach, for the first time, allows for data-driven visualization of unconventional well drainage volume in 3D. From the discussions made, the following conclusions can be drawn.

- A novel deep learning-based workflow that can efficiently visualize subsurface has been developed. The approach incorporates the FMM-based rapid simulation and the concept of DTOF to accelerate the workflow. Specifically, generating training datasets can be efficiently done by using the FMM-based rapid simulation, and the use of DTOF allows us to use a simple architecture of the deep learning-based models. The dimensionality reduction via an autoencoder further enhances the workflow.
- We demonstrated the efficacy and utility of the approach using the two examples, a synthetic case and a field-scale application, with different types of measured data.

- We introduced potential applications of the approach, including the post-processing using MDS to account for uncertainties and the workflow that can be used to evaluate data acquisition programs.
- Since our primary focus in this work is to demonstrate the new workflow, relatively simple methods were used. Therefore, the workflow can be further enhanced by incorporating more advanced methods. This will be discussed in the next section.

5.3 Recommendations

Although the FMM-based simulation approach accounting for gravity has been shown to be a good approximation of the full-physics simulation in the synthetic examples, we observed that the solutions degrade to some degree in the field-scale application involving 100+ hydraulic fractures. This indicates that the surface area weighted averaged transmissibilities (Eq. (2.5)) may not be able to capture the complex connections between the many hydraulic fracture gridblocks and the surrounding matrix gridblocks. In addition, the FMM-based simulation results are found to be sensitive to discretization scheme (the number of 1-D DTOF gridblocks), especially near the well, as reported by (Iino 2018). A viable remedy would be extending the region where we use original 2-D or 3-D gridblocks. Accuracy and stability of the approach can be improved by retaining the matrix (or SRV) gridblocks surrounding the hydraulic fracture planes in addition to the hydraulic fracture planes and connecting surface area of the retained gridblocks with the first 1-D DTOF gridblock via NNCs, as shown in Figure 5.1.

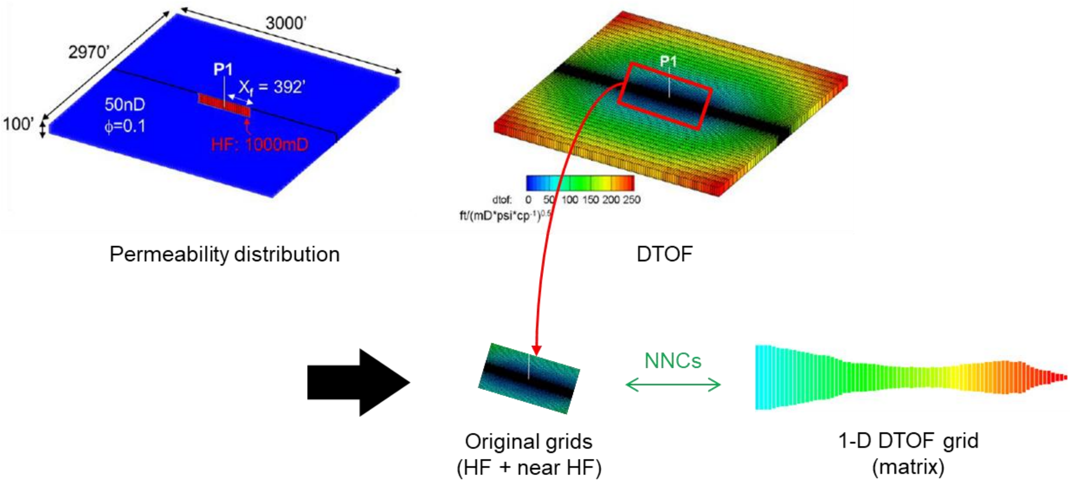

Figure 5.1 An extension of the FMM-based simulation workflow accounting for gravity

Transmissibility calculations using this approach are likely less affected by the averaging effects as reservoir properties in the matrix are typically much less heterogeneous. Also, the gridding scheme is expected to be less sensitive for the 1-D DTOF domain corresponding to the matrix, where there are little changes in pressure and saturations during simulations. We note here that, while this treatment is likely to improve the accuracy and stability of the approach, the number of gridblocks in the FMM-based simulation becomes greater than the original workflow, resulting in increased runtime. Multiple scenarios using different gridding schemes need to be investigated to find an optimal trade-off between accuracy and runtime.

For the finite-volume based FMM approach, the use of grid refinement techniques, such as local grid refinement can improve accuracy of the approach. It is similar to the multi-stencil FMM based on the finite difference discretization (Hassouna and Farag 2007) but differs in a sense that the implementation can be done in a much simpler way.

In the existing multi-stencil FMM approach, the sub-gridding is dependent on the grid geometry, and it is difficult to generalize for complex grid systems. In our approach, we can take advantage of the capability of the existing commercial reservoir simulator to perform grid refinements within the simulator, and local pore volumes and connection information (NNCs) are readily obtained from outputs of the simulator. Then, the Eikonal equation can be solved for the DTOF without any modifications in our implementation. In addition, while well established for single porosity models and dual-porosity single-permeability models, the FMM-based simulation approach for DPDK reservoir models has not yet been fully explored. Recommendations in this research direction are summarized in **Appendix B**.

Finally, for the deep learning-based subsurface imaging method, the following research directions are recommended:

- The parameter screening procedure could be improved by using more sophisticated statistical analysis, such as *t*-test, instead of the one-variable-at-a-time design.
- An investigation of more advanced methods, such as a variational autoencoder or a generative adversarial network, as a dimensionality reduction technique in the workflow would be an interesting area of future research.
- For the deep learning model architectures, although we tested multiple combinations of the hyperparameters and used the best ones (minimum validation loss), extensively exploring hyper parameter space (Bergstra and Bengio 2012) could further optimize the models.

- Post-processing using MDS could be enhanced by incorporating some kernel methods to transform the Euclidian space.
- Application of the proposed workflow to conventional reservoirs is also an interesting research direction. An example would be an application of the workflow to subsurface imaging and risk assessment during geologic CO_2 sequestration, which has been an active area of research in recent years in response to climate change due to higher CO_2 concentration in the atmosphere. Incorporating the convective time-of-flight (Datta-Gupta and King 2007), instead of the DTOF, in the workflow may be a better option in capturing convective fluxes, hence movement of CO_2 plume. On the other hand, the DTOF may be directly applicable if the problem of interest is tracking pressure during CO_2 sequestration for situations like pressure management and risk assessment of brine leakage through legacy wells (Onishi, Nguyen, et al. 2019).

REFERENCES

Agarwal, Ram G, Gardner, David C, Kleinsteiber, Stanley W et al. 1999. Analyzing well production data using combined-type-curve and decline-curve analysis concepts. *SPE Reservoir Evaluation & Engineering* **2** (05): 478-486.

Alhuthali, Ahmed, Oyerinde, Adedayo, and Datta-Gupta, Akhil. 2007. Optimal waterflood management using rate control. *SPE Reservoir Evaluation & Engineering* **10** (05): 539-551.

Arps, Jan J. 1945. Analysis of decline curves. *Transactions of the AIME* **160** (01): 228-247.

Baldi, Pierre and Hornik, Kurt. 1989. Neural networks and principal component analysis: Learning from examples without local minima. *Neural networks* **2** (1): 53-58.

Bao, A.. and Gildin, E.. 2017. Data-Driven Model Reduction Based on Sparsity-Promoting Methods for Multiphase Flow in Porous Media. *Proc.,* SPE Latin America and Caribbean Petroleum Engineering Conference. https://doi.org/10.2118/185514-MS.

Batycky, RP, Blunt, Martin J, and Thiele, Marco R. 1997. A 3D field-scale streamline-based reservoir simulator. *SPE Reservoir Engineering* **12** (04): 246-254.

Baydin, Atilim Gunes, Pearlmutter, Barak A, Radul, Alexey Andreyevich et al. 2018. Automatic differentiation in machine learning: a survey. *Journal of machine learning research* **18**.

Bergstra, James and Bengio, Yoshua. 2012. Random search for hyper-parameter optimization. *Journal of machine learning research* **13** (2).

Bhark, Eric and Dehghani, Kaveh. 2014. Assisted History Matching Benchmarking: Design of Experiments-based Techniques. *Proc.*, SPE Annual Technical Conference and Exhibition. https://doi.org/10.2118/170690-MS.

Bhark, Eric, Rey, Alvaro, Datta-Gupta, Akhil et al. 2012. A multiscale workflow for history matching in structured and unstructured grid geometries. *SPE Journal* **17** (03): 828-848.

Bisong, Ekaba. 2019. Google colaboratory. In *Building Machine Learning and Deep Learning Models on Google Cloud Platform*, 59-64. Springer.

Blasingame, TA, McCray, TL, and Lee, WJ. 1991. Decline curve analysis for variable pressure drop/variable flowrate systems. *Proc.,* SPE Gas Technology Symposium.

Borg, Ingwer and Groenen, Patrick JF. 2005. *Modern multidimensional scaling: Theory and applications*: Springer Science & Business Media.

Brooks, Royal Harvard and Corey, Arthur Thomas. 1964. Hydraulic properties of porous media and their relation to drainage design. *Transactions of the ASAE* **7** (1): 26-0028.

Buckley, Se E and Leverett, MCi. 1942. Mechanism of fluid displacement in sands. *Transactions of the AIME* **146** (01): 107-116.

Canchumuni, Smith Arauco, Emerick, Alexandre A, and Pacheco, Marco Aurelio. 2017. Integration of ensemble data assimilation and deep learning for history matching facies models. *Proc.,* OTC Brasil.

Cardoso, Marco A, Durlofsky, Louis J, and Sarma, Pallav. 2009. Development and application of reduced‐order modeling procedures for subsurface flow simulation. *International journal for numerical methods in engineering* **77** (9): 1322-1350.

Carter, Robert D. 1985. Type curves for finite radial and linear gas-flow systems: constant-terminal-pressure case. *Society of Petroleum Engineers Journal* **25** (05): 719-728.

Champion, Kathleen, Lusch, Bethany, Kutz, J Nathan et al. 2019. Data-driven discovery of coordinates and governing equations. *Proceedings of the National Academy of Sciences* **116** (45): 22445-22451.

Chan, Shing and Elsheikh, Ahmed H. 2017. Parametrization and generation of geological models with generative adversarial networks. *arXiv preprint arXiv:170801810*.

Chen, Hongquan, Onishi, Tsubasa, Olalotiti-Lawal, Feyi et al. 2020. Streamline tracing and applications in embedded discrete fracture models. *Journal of Petroleum Science and Engineering*: 106865.

Chen, Hongquan, Onishi, Tsubasa, Park, Jaeyoung et al. 2021. Computing Pressure Front Propagation Using the Diffusive-Time-of-Flight in Structured and Unstructured Grid Systems via the Fast-Marching Method. *SPE Journal*: 1-21.

Chen, Hongquan, Yang, Changdong, Datta-Gupta, Akhil et al. 2020. Fracture inference and optimal well placement using a multiscale history matching in a HPHT tight gas reservoir, Tarim Basin, China. *Upstream Oil and Gas Technology* **2**: 100002.

Cheng, Hao, Datta-Gupta, Akhil, and He, Zhong. 2005. A comparison of travel-time and amplitude matching for field-scale production-data integration: Sensitivity, nonlinearity, and practical implications. *Spe Journal* **10** (01): 75-90.

Cheng, Hao, Osako, Ichiro, Datta-Gupta, Akhil et al. 2006. A rigorous compressible streamline formulation for two and three-phase black-oil simulation. *SPE Journal* **11** (04): 407-417.

Ciezobka, Jordan and Reeves, Scott. 2021. Overview of Hydraulic Fracturing Test Sites (HFTS) in the Permian Basin and Summary of Selected Results (HFTS-I in Midland and HFTS-II in Delaware). *Proc.,* Latin America Unconventional Resources Technology Conference, 16-18 November 202093-102.

Cipolla, Craig L, Fitzpatrick, Tony, Williams, Michael John et al. 2011. Seismic-to-simulation for unconventional reservoir development. *Proc.,* SPE Reservoir Characterisation and Simulation Conference and Exhibition.

Cipolla, Craig L, Maxwell, Shawn C, and Mack, Mark Gavin. 2012. Engineering guide to the application of microseismic interpretations. *Proc.,* SPE hydraulic fracturing technology conference.

Cui, Jingyuan, Yang, Changdong, Zhu, Ding et al. 2016. Fracture diagnosis in multiple-stage-stimulated horizontal well by temperature measurements with fast marching method. *Spe Journal* **21** (06): 2,289-2,300.

Datta-Gupta, Akhil and King, Michael Joseph. 2007. *Streamline simulation: theory and practice,* Vol. 11: Society of Petroleum Engineers Richardson.

Datta-Gupta, Akhil, Xie, Jiang, Gupta, Neha et al. 2011. Radius of Investigation and its Generalization to Unconventional Reservoirs. *Journal of Petroleum Technology* **63** (07): 52-55. https://doi.org/10.2118/0711-0052-JPT.

Du, Song, Yoshida, Nozomu, Liang, Baosheng et al. 2016. Application of multi-segment well approach: Dynamic modeling of hydraulic fractures. *Journal of Natural Gas Science and Engineering* **34**: 886-897.

Duong, Anh N. 2010. An unconventional rate decline approach for tight and fracture-dominated gas wells. *Proc.*, Canadian unconventional resources and international petroleum conference.

EIA. 2021. Proved Reserves of Crude Oil and Natural Gas in the United States, Year-End 2019.

Fetkovich, M.J. 1980. Decline Curve Analysis Using Type Curves. *Journal of Petroleum Technology* **32** (06): 1065-1077. https://doi.org/10.2118/4629-PA.

Fetkovich, M.J., Vienot, M.E., Bradley, M.D. et al. 1987. Decline Curve Analysis Using Type Curves: Case Histories. *SPE Formation Evaluation* **2** (04): 637-656. https://doi.org/10.2118/13169-PA.

Forrest, James, Zhu, Tiejun, Xiong, Hongjie et al. 2018. The effect of initial conditions and fluid PVT Properties on unconventional oil and gas recoveries in the Wolfcamp formation in the Midland basin. *Proc.*, Unconventional Resources Technology Conference, Houston, Texas, 23-25 July 2018895-908.

Fraces, Cedric G, Papaioannou, Adrien, and Tchelepi, Hamdi. 2020. Physics Informed Deep Learning for Transport in Porous Media. Buckley Leverett Problem. *arXiv preprint arXiv:200105172*.

Fujita, Yusuke, Datta-Gupta, Akhil, and King, Michael J. 2016. A comprehensive reservoir simulator for unconventional reservoirs that is based on the Fast Marching method and diffusive time of flight. *SPE Journal* **21** (06): 2276-2288.

Fuks, Olga. 2020. *Physics Informed Machine Learning and Uncertainty Propagation for Multiphase Transport in Porous Media*: Stanford University.

Ghasemi, Mohammadreza, Yang, Yanfang, Gildin, Eduardo et al. 2015. Fast multiscale reservoir simulations using pod-deim model reduction. *Proc.*, SPE reservoir simulation symposium.

Ghommem, Mehdi, Gildin, Eduardo, and Ghasemi, Mohammadreza. 2016. Complexity reduction of multiphase flows in heterogeneous porous media. *SPE Journal* **21** (01): 144-151.

Ghommem, Mehdi, Presho, Michael, Calo, Victor M et al. 2013. Mode decomposition methods for flows in high-contrast porous media. Global–local approach. *Journal of computational physics* **253**: 226-238.

Goodfellow, Ian, Bengio, Yoshua, Courville, Aaron et al. 2016. *Deep learning*, Vol. 1: MIT press Cambridge.

Hassouna, M Sabry and Farag, Aly A. 2007. Multistencils fast marching methods: A highly accurate solution to the eikonal equation on cartesian domains. *IEEE transactions on pattern analysis and machine intelligence* **29** (9): 1563-1574.

He, Jincong and Durlofsky, Louis J. 2014. Reduced-Order Modeling for Compositional Simulation by Use of Trajectory Piecewise Linearization. *SPE Journal* **19** (05): 858-872. https://doi.org/10.2118/163634-PA.

He, Jincong, Sarma, Pallav, Bhark, Eric et al. 2018. Quantifying expected uncertainty reduction and value of information using ensemble-variance analysis. *SPE Journal* **23** (02): 428-448.

He, Jincong, Sarma, Pallav, and Durlofsky, Louis J. 2013. Reduced-order flow modeling and geological parameterization for ensemble-based data assimilation. *Computers & geosciences* **55**: 54-69.

He, Youwei, Cheng, Shiqing, Rui, Zhenhua et al. 2018. An improved rate-transient analysis model of multi-fractured horizontal wells with non-uniform hydraulic fracture properties. *Energies* **11** (2): 393.

He, Zhong, Datta-Gupta, A, and Yoon, S. 2002. Streamline-Based Production Data Integration with Gravity and Changing Field Conditions. SPEJ 7 (4): 423-436, SPE-81208-PA.

Heinemann, ZE, Brand, C, Munka, Margit et al. 1989. Modeling reservoir geometry with irregular grids. *Proc.*, SPE Symposium on Reservoir Simulation.

Hochreiter, Sepp and Schmidhuber, Jürgen. 1997. Long Short-Term Memory. *Neural Computation* **9** (8): 1735-1780. https://doi.org/10.1162/neco.1997.9.8.1735.

Huang, Jixiang, Olalotiti-Lawal, Feyisayo, King, Michael J et al. 2017. Modeling Well Interference and Optimal Well Spacingin Unconventional Reservoirs Using Fast Marching Method. *Proc.*, Unconventional Resources Technology Conference, Austin, Texas, 24-26 July 20172352-2372.

Hui, Mun-Hong, Dufour, Gaelle, Vitel, Sarah et al. 2019. A Robust Embedded Discrete Fracture Modeling Workflow for Simulating Complex Processes in Field-Scale Fractured Reservoirs. *Proc.*, SPE Reservoir Simulation Conference.

Iino, Atsushi. 2018. *Efficient History Matching and Optimization of Unconventional Reservoirs Using the Fast Marching Method*.

Iino, Atsushi and Arihara, Norio. 2007. Use of streamline simulation for waterflood management in naturally fractured reservoirs. *Proc.*, International Oil Conference and Exhibition in Mexico.

Iino, Atsushi, Jung, Hye Young, Onishi, Tsubasa et al. 2020. Rapid Simulation Accounting For Well Interference in Unconventional Reservoirs Using Fast Marching Method. *Proc.*, Unconventional Resources Technology Conference, 20–22 July 20204725-4743.

Iino, Atsushi, Onishi, Tsubasa, and Datta-Gupta, Akhil. 2020. Optimizing CO2-and field-gas-injection EOR in unconventional reservoirs using the fast-marching method. *SPE Reservoir Evaluation & Engineering* **23** (01): 261-281.

Iino, Atsushi, Vyas, Aditya, Huang, Jixiang et al. 2017. Rapid Compositional Simulation and History Matching of Shale Oil Reservoirs Using the Fast Marching Method. *Proc.*, Unconventional Resources Technology Conference, Austin, Texas, 24-26 July 20172834-2854.

Ilk, D.., Anderson, D.M.. M., Stotts, G.W.J.. W.J. et al. 2010. Production-Data Analysis—Challenges, Pitfalls, Diagnostics. *SPE Reservoir Evaluation & Engineering* **13** (03): 538-552. https://doi.org/10.2118/102048-PA.

Ilk, Dilhan, Rushing, Jay Alan, Perego, Albert Duane et al. 2008. Exponential vs. hyperbolic decline in tight gas sands: understanding the origin and implications for reserve estimates using Arps' decline curves. *Proc.*, SPE annual technical conference and exhibition.

Jeong, Won-ki and Whitaker, R. 2007. A fast eikonal equation solver for parallel systems. *Proc.*, SIAM conference on Computational Science and Engineering.

Jessen, K and Orr Jr, FM. 2002. Compositional streamline simulation. *Proc.*, SPE Annual Technical Conference and Exhibition.

Jiang, Jiamin and Younis, Rami M. 2016. Hybrid coupled discrete-fracture/matrix and multicontinuum models for unconventional-reservoir simulation. *SPE Journal* **21** (03): 1,009-1,027.

Jimenez, Eduardo, Datta-Gupta, Akhil, and King, Michael J. 2010. Full-field streamline tracing in complex faulted systems with non-neighbor connections. *SPE Journal* **15** (01): 7-17.

Kam, Dongjae and Datta-Gupta, Akhil. 2016. Streamline-based transport tomography with distributed water arrival times. *SPE Reservoir Evaluation & Engineering* **19** (02): 265-277.

Karimi-Fard, M. and Firoozabadi, A. 2001. Numerical Simulation of Water Injection in 2D Fractured Media Using Discrete-Fracture Model. *Proc.*, SPE Annual Technical Conference and Exhibition. https://doi.org/10.2118/71615-MS.

Kazemi, H, Merrill Jr, LS, Porterfield, KL et al. 1976. Numerical simulation of water-oil flow in naturally fractured reservoirs. *Society of Petroleum Engineers Journal* **16** (06): 317-326.

Kazemi, H., Merrill, L.S., Jr., Porterfield, K.L. et al. 1976. Numerical Simulation of Water-Oil Flow in Naturally Fractured Reservoirs. *Society of Petroleum Engineers Journal* **16** (06): 317-326. https://doi.org/10.2118/5719-PA.

King, Michael J., Wang, Zhenzhen, and Datta-Gupta, Akhil. 2016. Asymptotic Solutions of the Diffusivity Equation and Their Applications. *Proc.*, SPE Europec featured at 78th EAGE Conference and Exhibition. https://doi.org/10.2118/180149-MS.

Kingma, Diederik P and Ba, Jimmy. 2014. Adam: A method for stochastic optimization. *arXiv preprint arXiv:14126980*.

Klie, Hector and Florez, Horacio. 2020. Data-Driven Prediction of Unconventional Shale-Reservoir Dynamics. *SPE Journal*.

Kulkarni, Kari Nordaas, Datta-Gupta, Akhil, and Vasco, Don W. 2001. A streamline approach for integrating transient pressure data into high-resolution reservoir models. *Spe Journal* **6** (03): 273-282.

Kumar, Sarwesh, Rey, Alvaro, Dufour, Gaelle et al. 2019. Understanding Fluid Flow Behavior in Fractured Reservoir using Dual Porosity Dual Permeability and Discretized Fracture Model. *Proc.*, SPE Annual Technical Conference and Exhibition.

Kutz, J Nathan, Brunton, Steven L, Brunton, Bingni W et al. 2016. *Dynamic mode decomposition: data-driven modeling of complex systems*: SIAM.

Laloy, Eric, Hérault, Romain, Jacques, Diederik et al. 2018. Training‐image based geostatistical inversion using a spatial generative adversarial neural network. *Water Resources Research* **54** (1): 381-406.

Laloy, Eric, Hérault, Romain, Lee, John et al. 2017. Inversion using a new low-dimensional representation of complex binary geological media based on a deep neural network. *Advances in water resources* **110**: 387-405.

Lantz, RB. 1971. Quantitative evaluation of numerical diffusion (truncation error). *Society of Petroleum Engineers Journal* **11** (03): 315-320.

Lee, John. 1982. *Well testing*: Society of Petroleum Engineers.

Li, Boxiao, Bhark, Eric W, Billiter, Travis C et al. 2019. Best practices of assisted history matching using design of experiments. *SPE Journal* **24** (04): 1435-1451.

Li, Chen. 2018. *Application of the Fast Marching Method to Reservoir Characterization and Pressure Transient Analysis in Structured and Corner Point Grid Geometries*.

Li, Liyong and Lee, Seong H. 2008. Efficient field-scale simulation of black oil in a naturally fractured reservoir through discrete fracture networks and homogenized media. *SPE Reservoir Evaluation & Engineering* **11** (04): 750-758.

Lie, Knut-Andreas. 2019. *An introduction to reservoir simulation using MATLAB/GNU Octave: User guide for the MATLAB Reservoir Simulation Toolbox (MRST)*: Cambridge University Press.

Lie, Knut–Andreas, Møyner, Olav, and Krogstad, Stein. 2015. Application of flow diagnostics and multiscale methods for reservoir management. *Proc.*, SPE Reservoir Simulation Symposium.

Lindsay, G, Miller, G, Xu, T et al. 2018. Production performance of infill horizontal wells vs. pre-existing wells in the major US unconventional basins. *Proc.*, SPE hydraulic fracturing technology conference and exhibition.

Lindsay, GJ, White, DJ, Miller, GA et al. 2016. Understanding the applicability and economic viability of refracturing horizontal wells in unconventional plays. *Proc.*, SPE hydraulic fracturing technology conference.

Liu, Tian, Chen, Hongquan, Hetz, Gill et al. 2020. Integration of time-lapse seismic data using the onset time approach: The impact of seismic survey frequency. *Journal of Petroleum Science and Engineering*: 106989.

Liu, Yimin, Sun, Wenyue, and Durlofsky, Louis J. 2019. A deep-learning-based geological parameterization for history matching complex models. *Mathematical Geosciences* **51** (6): 725-766.

Maity, Debotyam. 2018. Microseismicity analysis for HFTS pad and correlation with completion parameters. *Proc.*, Unconventional Resources Technology Conference, Houston, Texas, 23-25 July 20183810-3821.

Manohar, Krithika, Brunton, Bingni W, Kutz, J Nathan et al. 2018. Data-driven sparse sensor placement for reconstruction: Demonstrating the benefits of exploiting known patterns. *IEEE Control Systems Magazine* **38** (3): 63-86.

Marongiu-Porcu, Matteo, Lee, Donald, Shan, Dan et al. 2016. Advanced modeling of interwell-fracturing interference: an Eagle Ford shale-oil study. *SPE Journal* **21** (05): 1567-1582.

Matringe, Sebastien Francois and Juanes, Ruben. 2005. Streamline tracing on general triangular or quadrilateral grids. *Proc.*, SPE Annual Technical Conference and Exhibition.

McKay, Michael D, Beckman, Richard J, and Conover, William J. 2000. A comparison of three methods for selecting values of input variables in the analysis of output from a computer code. *Technometrics* **42** (1): 55-61.

Miller, Grant, Lindsay, Garrett, Baihly, Jason et al. 2016. Parent Well Refracturing: Economic Safety Nets in an Uneconomic Market. *Proc.*, SPE Low Perm Symposium. https://doi.org/10.2118/180200-MS.

Mo, Shaoxing, Zabaras, Nicholas, Shi, Xiaoqing et al. 2020. Integration of Adversarial Autoencoders With Residual Dense Convolutional Networks for Estimation of Non‐Gaussian Hydraulic Conductivities. *Water Resources Research* **56** (2): e2019WR026082.

Mo, Shaoxing, Zhu, Yinhao, Zabaras, Nicholas et al. 2019. Deep convolutional encoder‐decoder networks for uncertainty quantification of dynamic multiphase flow in heterogeneous media. *Water Resources Research* **55** (1): 703-728.

Moinfar, Ali, Varavei, Abdoljalil, Sepehrnoori, Kamy et al. 2014. Development of an efficient embedded discrete fracture model for 3D compositional reservoir simulation in fractured reservoirs. *SPE Journal* **19** (02): 289-303.

Møyner, Olav, Krogstad, Stein, and Lie, Knut-Andreas. 2015. The application of flow diagnostics for reservoir management. *SPE Journal* **20** (02): 306-323.

Natvig, Jostein R, Lie, Knut–Andreas, Eikemo, Birgitte et al. 2007. An efficient discontinuous Galerkin method for advective transport in porous media. *Advances in water resources* **30** (12): 2424-2438.

Nobakht, Morteza and Clarkson, Christopher R. 2012a. A new analytical method for analyzing linear flow in tight/shale gas reservoirs: constant-flowing-pressure boundary condition. *SPE Reservoir Evaluation & Engineering* **15** (03): 370-384.

Nobakht, Morteza and Clarkson, Christopher R. 2012b. A new analytical method for analyzing linear flow in tight/shale gas reservoirs: constant-rate boundary condition. *SPE Reservoir Evaluation & Engineering* **15** (01): 51-59.

Ojha, Shiv Prakash, Misra, Siddharth, Sinha, Ankita et al. 2018. Relative Permeability and Production-Performance Estimations for Bakken, Wolfcamp, Eagle Ford, and Woodford Shale Formations. *SPE Reservoir Evaluation & Engineering* **21** (02): 307-324.

Olalotiti-Lawal, Feyi, Hetz, Gil, Salehi, Amir et al. 2020. Application of Flow Diagnostics to Rapid Production Data Integration in Complex Grids and Dual-Permeability Models. *SPE Journal*.

Olalotiti-Lawal, Feyi, Onishi, Tsubasa, Datta-Gupta, Akhil et al. 2018. Post-Combustion CO2 WAG Pilot in a Mature Field: Model Calibration and Optimization. *Proc.*, SPE Annual Technical Conference and Exhibition.

Olalotiti-Lawal, Feyi, Onishi, Tsubasa, Datta-Gupta, Akhil et al. 2019. Model calibration and optimization of a post-combustion CO2 WAG pilot in a mature oil field. *Fuel* **255**: 115810.

Olalotiti-Lawal, Feyi, Tanaka, Shusei, and Datta-Gupta, Akhil. 2020. Streamline-Based Simulation of Carbon Dioxide Sequestration in Saline Aquifers. *arXiv preprint arXiv:200412139*.

Oliver, Dean S. 1996. Multiple realizations of the permeability field from well test data. *SPE Journal* **1** (02): 145-154.

Onishi, Tsubasa, Iino, Atsushi, Jung, Hye Young et al. 2019. Fast Marching Method Based Rapid Simulation Accounting for Gravity.

Onishi, Tsubasa, Iino, Atsushi, Jung, Hye Young et al. 2020. Fast Marching Method Based Rapid Simulation Accounting for Gravity. *Proc.*, Asia Pacific Unconventional Resources Technology Conference, Brisbane, Australia, 18-19 November 20191093-1111.

Onishi, Tsubasa, Nguyen, Minh C, Carey, J William et al. 2019. Potential CO2 and brine leakage through wellbore pathways for geologic CO2 sequestration using the National Risk Assessment Partnership tools: Application to the Big Sky Regional Partnership. *International Journal of Greenhouse Gas Control* **81**: 44-65.

Palacio, JC and Blasingame, TA. 1993. Decline curve analysis using type curves: Analysis of gas well production data. *paper SPE* **25909**: 12-14.

Palagi, Cesar Luiz and Aziz, Khalid. 1994. Use of Voronoi grid in reservoir simulation. *SPE Advanced Technology Series* **2** (02): 69-77.

Park, Han-Young, Datta-Gupta, Akhil, and King, Michael J. 2013. Handling conflicting multiple objectives using Pareto-based evolutionary algorithm during history matching of reservoir performance. *Proc.*, SPE Reservoir Simulation Symposium.

Park, Jaeyoung, Iino, Atsushi, Datta-Gupta, Akhil et al. 2021. Novel hybrid fast marching method-based simulation workflow for rapid history matching and completion design optimization of hydraulically fractured shale wells. *Journal of Petroleum Science and Engineering* **196**: 107718.

Pollock, David W. 1988. Semianalytical computation of path lines for finite ‐ difference models. *Groundwater* **26** (6): 743-750.

Prevost, Mathieu, Edwards, Michael G, and Blunt, Martin J. 2001. Streamline tracing on curvilinear structured and unstructured grids. *Proc.*, SPE Reservoir Simulation Symposium.

Raghavan, Rajagopal and Chin, Lee Y. 2002. Productivity changes in reservoirs with stress-dependent permeability. *Proc.*, SPE annual technical conference and exhibition.

Raissi, Maziar, Perdikaris, Paris, and Karniadakis, George E. 2019. Physics-informed neural networks: A deep learning framework for solving forward and inverse problems involving nonlinear partial differential equations. *Journal of Computational Physics* **378**: 686-707.

Razak, Syamil Mohd and Jafarpour, Behnam. 2020. Convolutional neural networks (CNN) for feature-based model calibration under uncertain geologic scenarios. *Computational Geosciences* **24** (4): 1625-1649.

Reynolds, Albert C, He, Nanqun, Chu, Lifu et al. 1996. Reparameterization techniques for generating reservoir descriptions conditioned to variograms and well-test pressure data. *SPE Journal* **1** (04): 413-426.

Ronneberger, Olaf, Fischer, Philipp, and Brox, Thomas. 2015. U-net: Convolutional networks for biomedical image segmentation. *Proc.*, International Conference on Medical image computing and computer-assisted intervention234-241.

Sarma, Pallav, Durlofsky, Louis J, and Aziz, Khalid. 2008. Kernel principal component analysis for efficient, differentiable parameterization of multipoint geostatistics. *Mathematical Geosciences* **40** (1): 3-32.

Sarma, Pallav, Durlofsky, Louis J, Aziz, Khalid et al. 2006. Efficient real-time reservoir management using adjoint-based optimal control and model updating. *Computational Geosciences* **10** (1): 3-36.

Scheidt, Céline and Caers, Jef. 2009. Uncertainty quantification in reservoir performance using distances and kernel methods--application to a west africa deepwater turbidite reservoir. *SPE Journal* **14** (04): 680-692.

Schlumberger. Petrel Fracture Modeling, software.slb.com/products/petrel/petrel-geology-and-modeling/fracture-modeling.

Schlumberger. 2015. ECLIPSE Technical description. *Schlumberger Ltd*.

Sethian, James A. 1999. Fast marching methods. *SIAM review* **41** (2): 199-235.

Sethian, James A and Vladimirsky, Alexander. 2001. Ordered upwind methods for static Hamilton–Jacobi equations. *Proceedings of the National Academy of Sciences* **98** (20): 11069-11074.

Shahvali, Mohammad, Mallison, Bradley, Wei, Kaihong et al. 2012. An alternative to streamlines for flow diagnostics on structured and unstructured grids. *SPE Journal* **17** (03): 768-778.

Song, Bo and Ehlig-Economides, Christine. 2011. Rate-Normalized Pressure Analysis for Determination of Shale Gas Well Performance. *Proc.*, North American Unconventional Gas Conference and Exhibition. https://doi.org/10.2118/144031-MS.

Stegent, Neil and Candler, Cody. 2018. Downhole microseismic mapping of more than 400 fracturing stages on a multiwell pad at the Hydraulic Fracturing Test Site (HFTS): discussion of operational challenges and analytic results. *Proc.*, Unconventional Resources Technology Conference, Houston, Texas, 23-25 July 20183754-3781.

Sun, Jianlei and Schechter, David. 2015. Optimization-based unstructured meshing algorithms for simulation of hydraulically and naturally fractured reservoirs with variable distribution of fracture aperture, spacing, length, and strike. *SPE Reservoir Evaluation & Engineering* **18** (04): 463-480.

Tanaka, Shusei, Datta-Gupta, Akhil, and King, Michael J. 2014. Compositional Streamline simulation of Co2 Injection Accounting for Gravity and Capillary Effects Using Orthogonal Projection. *Proc.*, SPE Improved Oil Recovery Symposium.

Tanaka, Shusei, Kam, Dongjae, Datta-Gupta, Akhil et al. 2015. Streamline-based history matching of arrival times and bottomhole pressure data for multicomponent compositional systems. *Proc.*, SPE Annual Technical Conference and Exhibition.

Tanaka, Shusei, Kam, Dongjae, Xie, Jiang et al. 2017. A Generalized Derivative-Free Rate Allocation Optimization for Water and Gas Flooding Using Streamline-Based Method. *Proc.*, SPE Annual Technical Conference and Exhibition.

Tanaka, Shusei, Onishi, Tsubasa, Kam, Dongjae et al. 2020. Application of Combined Streamline Based Reduced-Physics Surrogate and Response Surface Method for

Field Development Optimization. *Proc.*, International Petroleum Technology Conference. https://doi.org/10.2523/IPTC-19958-MS.

Tang, Hewei, Fu, Pengcheng, Sherman, Christopher S et al. 2021. A Deep Learning-Accelerated Data Assimilation and Forecasting Workflow for Commercial-Scale Geologic Carbon Storage. *arXiv preprint arXiv:210509468*.

Tang, Meng, Ju, Xin, and Durlofsky, Louis J. 2021. Deep-learning-based coupled flow-geomechanics surrogate model for CO $ _2 $ sequestration. *arXiv preprint arXiv:210501334*.

Tang, Meng, Liu, Yimin, and Durlofsky, Louis J. 2020. A deep-learning-based surrogate model for data assimilation in dynamic subsurface flow problems. *Journal of Computational Physics* **413**: 109456.

Țene, Matei, Bosma, Sebastian BM, Al Kobaisi, Mohammed Saad et al. 2017. Projection-based embedded discrete fracture model (pEDFM). *Advances in Water Resources* **105**: 205-216.

Thiele, Marco R and Batycky, Rod. 2003. Water injection optimization using a streamline-based workflow. *Proc.*, SPE Annual Technical Conference and Exhibition.

Thomas, Sunil, Du, Song, Dufour, Gaelle et al. 2019. Recent Developments in Unstructured Aggregation-Based Upscaling for Simulation Workflows and Applications. *Proc.*, SPE Reservoir Simulation Conference.

Uzun, Ilkay, Kurtoglu, Basak, and Kazemi, Hossein. 2016. Multiphase rate-transient analysis in unconventional reservoirs: theory and application. *SPE Reservoir Evaluation & Engineering* **19** (04): 553-566.

Valkó, Peter P and Lee, W John. 2010. A better way to forecast production from unconventional gas wells. *Proc.*, SPE Annual technical conference and exhibition.

Van Doren, Jorn FM, Markovinović, Renato, and Jansen, Jan-Dirk. 2006. Reduced-order optimal control of water flooding using proper orthogonal decomposition. *Computational Geosciences* **10** (1): 137-158.

Vasco, D Wr, Yoon, Seongsik, and Datta-Gupta, Akhil. 1998. Integrating dynamic data into high-resolution reservoir models using streamline-based analytic sensitivity coefficients. *Proc.*, SPE Annual Technical Conference and Exhibition.

Vasco, Donald Wyman and Datta-Gupta, Akhil. 2016. *Subsurface Fluid Flow and Imaging: With Applications for Hydrology, Reservoir Engineering, and Geophysics*: Cambridge University Press.

Vasco, DW, Keers, Henk, and Karasaki, Kenzi. 2000. Estimation of reservoir properties using transient pressure data: An asymptotic approach. *Water Resources Research* **36** (12): 3447-3465.

Vo, Hai X and Durlofsky, Louis J. 2014. A new differentiable parameterization based on principal component analysis for the low-dimensional representation of complex geological models. *Mathematical Geosciences* **46** (7): 775-813.

Wang, Zhenzhen, Malone, Andrew, and King, Michael J. 2018. Quantitative production analysis and EUR prediction from unconventional reservoirs using a data-driven drainage volume formulation. *Proc.*, ECMOR XVI-16th European Conference on the Mathematics of Oil Recovery1, 1-39.

Warpinski, Norm. 2009. Microseismic monitoring: Inside and out. *Journal of Petroleum Technology* **61** (11): 80-85.

Warren, J.E. and Root, P.J. 1963. The Behavior of Naturally Fractured Reservoirs. *Society of Petroleum Engineers Journal* **3** (03): 245-255. https://doi.org/10.2118/426-PA.

Wattenbarger, Robert A, El-Banbi, Ahmed H, Villegas, Mauricio E et al. 1998. Production analysis of linear flow into fractured tight gas wells. *Proc.,* SPE rocky mountain regional/low-permeability reservoirs symposium.

Wen, Gege, Hay, Catherine, and Benson, Sally M. 2021. CCSNet: a deep learning modeling suite for CO $ _2 $ storage. *arXiv preprint arXiv:210401795*.

Xie, Jiang, Yang, Changdong, Gupta, Neha et al. 2015. Depth of investigation and depletion in unconventional reservoirs with fast-marching methods. *SPE Journal* **20** (04): 831-841.

Xu, Rui, Zhang, Dongxiao, Rong, Miao et al. 2021. Weak form theory-guided neural network (TgNN-wf) for deep learning of subsurface single-and two-phase flow. *Journal of Computational Physics* **436**: 110318.

Xu, Tao, Lindsay, Garrett, Baihly, Jason et al. 2017. Unique multidisciplinary approach to model and optimize pad Refracturing in the Haynesville Shale. *Proc.,* Unconventional Resources Technology Conference, Austin, Texas, 24-26 July 20173289-3303.

Xue, Xu, Yang, Changdong, Onishi, Tsubasa et al. 2019a. Modeling Hydraulically Fractured Shale Wells Using the Fast-Marching Method With Local Grid Refinements and an Embedded Discrete Fracture Model. *SPE Journal* **24** (06): 2,590-2,608.

Xue, Xu, Yang, Changdong, Onishi, Tsubasa et al. 2019b. Modeling Hydraulically Fractured Shale Wells Using the Fast Marching Method with Local Grid Refinements LGRs and Embedded Discrete Fracture Model EDFM. *Proc.,* SPE Reservoir Simulation Conference.

Xue, Xu, Yang, Changdong, Park, Jaeyoung et al. 2018. Reservoir and Fracture-Flow Characterization Using Novel Diagnostic Plots. *SPE Journal*.

Xue, Xu, Yang, Changdong, Park, Jaeyoung et al. 2019. Reservoir and fracture-flow characterization using novel diagnostic plots. *SPE Journal* **24** (03): 1,248-1,269.

Yan, Bicheng, Harp, Dylan Robert, Chen, Bailian et al. 2021. A Physics-Constrained Deep Learning Model for Simulating Multiphase Flow in 3D Heterogeneous Porous Media. *arXiv preprint arXiv:210509467*.

Yan, Bicheng, Harp, Dylan Robert, and Pawar, Rajesh J. 2021. A Gradient-based Deep Neural Network Model for Simulating Multiphase Flow in Porous Media. *arXiv preprint arXiv:210502652*.

Yang, Changdong, Sharma, Vishal, Datta-Gupta, Akhil et al. 2015. A novel approach for production transient analysis of shale gas/oil reservoirs.

Yang, Changdong, Xue, Xu, King, Michael J. et al. 2017. Flow Simulation of Complex Fracture Systems With Unstructured Grids Using the Fast Marching Method. *Proc.,* SPE/AAPG/SEG Unconventional Resources Technology Conference. https://doi.org/10.15530/URTEC-2017-2691393.

Yang, D., Xue, X., and Chen, J. 2018. High Resolution Hydraulic Fracture Network Modeling Using Flexible Dual Porosity Dual Permeability Framework. *Proc.*, SPE Western Regional Meeting.

Zhang, Yanbin, Bansal, Neha, Fujita, Yusuke et al. 2016. From streamlines to Fast Marching: Rapid simulation and performance assessment of shale-gas reservoirs by use of diffusive time of flight as a spatial coordinate. *SPE Journal* **21** (05): 1883-1898.

Zhang, Yanbin, He, Jincong, Yang, Changdong et al. 2018. A physics-based data-driven model for history matching, prediction, and characterization of unconventional reservoirs. *SPE Journal* **23** (04): 1,105-1,125.

Zhang, Yanbin, King, Michael J, and Datta‐Gupta, Akhil. 2012. Robust streamline tracing using inter‐cell fluxes in locally refined and unstructured grids. *Water Resources Research* **48** (6).

Zhang, Yanbin, Yang, Changdong, He, Jincong et al. 2019. Multiphase Production Data Analysis for Shale and Tight Reservoirs Using the Diffusive Diagnostic Function. *Proc.*, Unconventional Resources Technology Conference, Denver, Colorado, 22-24 July 20191955-1982.

Zhang, Yanbin, Yang, Changdong, King, Michael J et al. 2013. Fast-marching methods for complex grids and anisotropic permeabilities: Application to unconventional reservoirs. *Proc.*, SPE Reservoir Simulation Symposium.

Zheng, Chuansheng, Deng, Xianbo, Fu, Qing et al. 2020. Deep learning-based detection for COVID-19 from chest CT using weak label. *MedRxiv*.

Zhong, Zhi, Sun, Alexander Y., Ren, Bo et al. 2021. A Deep-Learning-Based Approach for Reservoir Production Forecast under Uncertainty. *SPE Journal*: 1-27. https://doi.org/10.2118/205000-PA.

Zhu, Yinhao and Zabaras, Nicholas. 2018. Bayesian deep convolutional encoder–decoder networks for surrogate modeling and uncertainty quantification. *Journal of Computational Physics* **366**: 415-447.

Zhu, Yinhao, Zabaras, Nicholas, Koutsourelakis, Phaedon-Stelios et al. 2019. Physics-constrained deep learning for high-dimensional surrogate modeling and uncertainty quantification without labeled data. *Journal of Computational Physics* **394**: 56-81.

APPENDIX A

DEEP LEARNING MODEL SETTING DETAILS

Detailed deep learning model settings in terms of operations at each of the layers and output shapes are summarized in the tables below. ‘None’ in the ‘Output Shape’ columns corresponds to the number of batch size during the trainings. The ‘Relu’ activation function is used for all the layers, except for the output layers, where ‘Sigmoid’ is used to scale the values to [0, 1].

Model	**Layer**	**Output Shape**
Encoder	Input	(None, 100, 100, 1)
	Conv2D layer #1 (8 filters, kernel size 3×3, stride 2)	(None, 50, 50, 8)
	Conv2D layer #2 (16 filters, kernel size 3×3, stride 2)	(None, 25, 25, 16)
	Conv2D layer #3 (32 filters, kernel size 3×3, stride 2)	(None, 13, 13, 32)
	Flatten	(None, 5048)
	Dense layer (latent space)	(None, 32)
Decoder	Decoder dense layer	(None, 5408)
	Reshape	(None, 13, 13, 32)
	Conv2D transpose layer (16 filters, kernel size 3×3, stride 2)	(None, 26, 26, 16)
	Conv2D transpose layer (8 filters, kernel size 3×3, stride 2)	(None, 52, 52, 8)
	Conv2D transpose layer (1 filters, kernel size 3×3, stride 2)	(None, 104, 104, 1)
	Cropping2D	(None, 100, 100, 1)

Table A1. Architecture of the autoencoder for the 2D synthetic case

Model	Layer	Output Shape
Feedforward	Input	(None, 8, 201)
	Dense #1	(None, 8, 40)
	Dense #2	(None, 8, 40)
	Dense #3	(None, 8, 40)
	Dense #4	(None, 8, 40)
	Dense #5	(None, 8, 40)
	Flatten	(None, 320)
	Dense #6 (output)	(None, 32)

Table A2. Architecture of the regression model for the 2D synthetic case

Model	Layer	Output Shape
Encoder	Input	(None, 23, 137, 47, 1)
	Conv3D layer #1 (8 filters, kernel size 3×3×3, stride 2)	(None, 12, 69, 24, 8)
	Conv3D layer #2 (16 filters, kernel size 3×3×3, stride 2)	(None, 6, 35, 12, 16)
	Conv3D layer #3 (32 filters, kernel size 3×3×3, stride 2)	(None, 3, 18, 6, 32)
	Flatten	(None, 10368)
	Dense layer (latent space)	(None, 256)
Decoder	Decoder dense layer	(None, 10368)
	Reshape	(None, 3, 18, 6, 32)
	Conv3D transpose layer (16 filters, kernel size 3×3×3, stride 2)	(None, 6, 36, 12, 16)
	Conv3D transpose layer (8 filters, kernel size 3×3×3, stride 2)	(None, 12, 72, 24, 8)
	Conv3D transpose layer (1 filters, kernel size 3×3×3, stride 2)	(None, 24, 144, 48, 1)
	Cropping3D	(None, 23, 137, 47, 1)

Table A3. Architecture of the autoencoder for the 3D field-scale application

Model	Layer	Output Shape
Feedforward	Input #1	(None, 3, 151)
	Input #2	(None, 1, 112)
	Intermediate layer #1	(None, 3, 100)
	Intermediate layer #2	(None, 1, 100)
	Concatenate	(None, 4, 100)
	Dense #1	(None, 4, 100)
	Dense #2	(None, 4, 100)
	Dense #3	(None, 4, 100)
	Flatten	(None, 400)
	Dense #4 (output)	(None, 256)

Table A4. Architecture of the regression model for the 3D field-scale application

APPENDIX B

THE FMM-BASED SIMULATION FOR DPDK RESERVOIR MODELS

Let us consider a single-phase flow problem in unconventional reservoirs. The key assumption in the FMM-based simulation is $P(\mathbf{x},t) \approx P(\tau(\mathbf{x}),t)$. In other words, we assume that the DTOF contours are aligned with pressure changes. Before investigating application of the FMM-based simulation approach to DPDK reservoir models, let us revisit a single-porosity problem. We consider a 2D homogeneous reservoir as shown in Figure B1(a). The model size is 3000×3000×100 (ft^3) with 101×101×1 grid discretization. Uniform permeability and porosity values of 1.0e-2 (mD) and 0.05 are used. There is a producer located at the center of the domain, producing fluids with a constant production rate. Figure B1 shows a visual comparison between a pressure map at a certain time step before the solutions are strongly affected by the finite boundary effects and the DTOF map. In addition, following King et al. (2016), a cross-plot comparing $exp(-\tau^2/4t)$ and dP/dt is provided in Figure B2, in which a high value of R^2 is obtained. Some scatters that are not aligned with the straight line (scatters at around $exp(-\tau^2/4t) = 1$) correspond to the near well region, where the DTOF calculations show numerical artifacts. Specifically, while it takes some time for the pressure front to travel from the well to boundary of the well cell, τ=0 is uniformly assigned at the well cell (source point) in the DTOF calculations because the solutions are based on the original grid resolution. This can be mitigated by using the local grid refinement technique for gridblocks at the near well region, for example. Nevertheless, *exp*(-$\tau^2/4t$) and *dP*/*dt* are mostly well aligned on the straight line, validating the assumption.

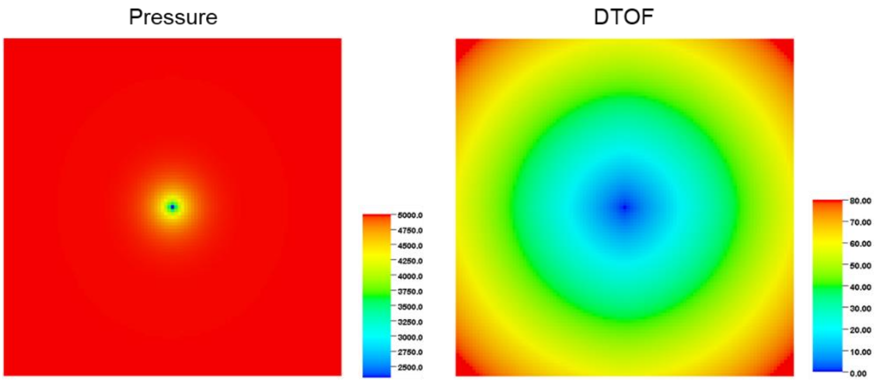

Figure B1 A visual comparison between a pressure map (left) and a DTOF map (right) for a 2D homogeneous single-porosity example

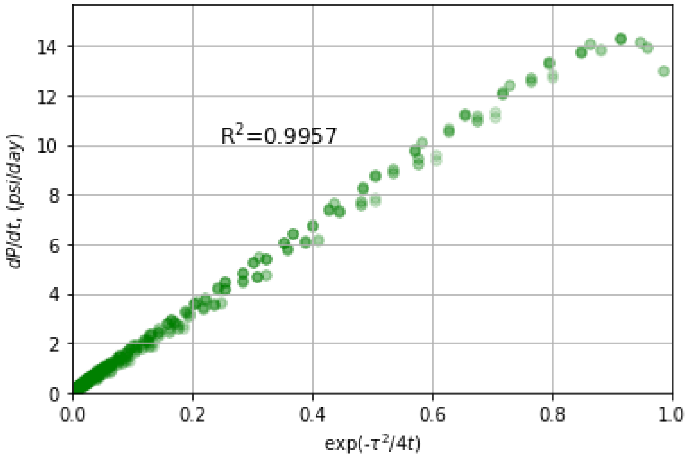

Figure B2 Numerical validation of the asymptotic pressure approximation for a 2D homogeneous single-porosity example

We repeated the same exercise using a DPDK reservoir model. The reservoir size and discretization scheme for each domain are the same as the single-porosity case, and the reservoir properties are summarized in Table B1. Visual comparisons of pressure and DTOF maps are shown in Figure B3. While we see slightly faster pressure front propagation in the fracture domain, the overall pressure and DTOF profiles are similar in the two systems. This is because the conductivity contrast between the two systems is moderate, as in typical settings in DPDK reservoir models, where both fracture and matrix domain contribute to the flow. Next, we compared $exp(-\tau^2/4t)$ and dP/dt, and the results are shown in Figure B4.

Parameter	Value
Permeability (matrix, fracture), k_m, k_f (mD)	1.0e-4, 1.0e-2
Porosity (matrix, fracture), ϕ_m, ϕ_f, (-)	0.05, 0.01
Shape factor, σ, (ft^{-2})	0.12

Table B1 Inputs for the 2D homogeneous DPDK case

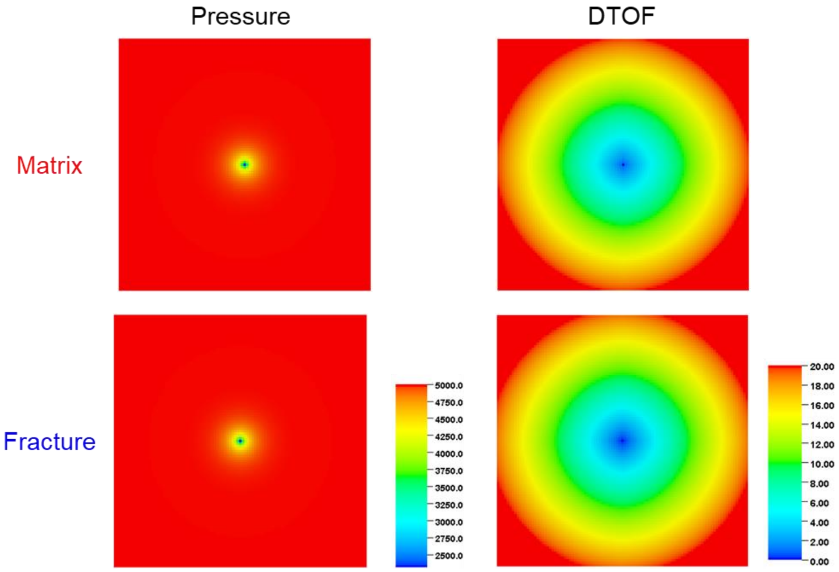

Figure B3 Visual comparisons between pressure maps (left column) and DTOF map (right column) for a 2D homogeneous DPDK reservoir

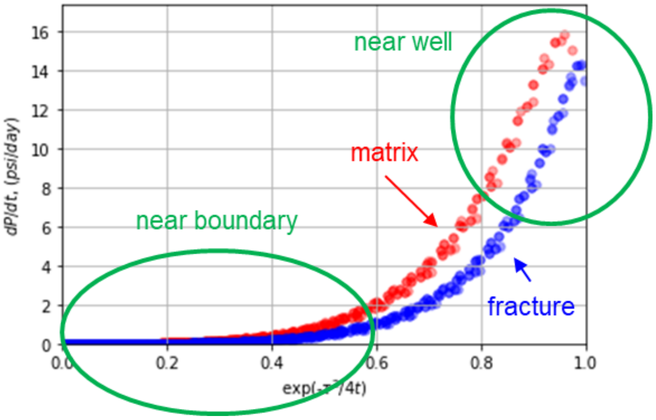

Figure B4 Numerical validation of the asymptotic pressure approximation for a 2D homogeneous DPDK reservoir

There are two interesting observations. First, there are two different groups of scatters that correspond to the two different systems. Second, in contrast to the single-porosity case, the scatters no longer follow a straight line trend. This is likely because of the interactions between the two systems. The resultant DTOF map may be utilized within the FMM-based simulation approach for DPDK reservoirs. However, while well established for single-porosity and dual-porosity single-permeability (DPSK) models (Fujita et al. 2016, Iino 2018), the use of DTOF within the FMM-based simulation workflow for DPDK reservoir models has not yet been fully explored. Here, we recommend an extension of the FMM-based simulation workflow for DPDK reservoirs. First, we compute the DTOF for fracture and matrix domains using the proposed FMM approach in Chapter III. Then, the DTOF is utilized for coordinate transformation for the two systems, as shown in Figure B5. Next, discretization in the DTOF coordinate can be done using the fracture DTOF following the FMM-based simulation approach for DPSK reservoir models. Then, we compute transmissibilities within each domain using the $w(\tau)$ function based on the cumulative drainage pore volume and DTOF in each domain as in Figure 4.1. In addition, transmissibilities (transfer transmissibilities) between the two domains ($T=C\cdot k_m\cdot V_{b,m}\cdot\sigma$ where C is a unit conversion constant (field), k_m is matrix permeability, $V_{b,m}$ is bulk volume of the matrix gridblock, and σ is the shape factor (Schlumberger 2015)) can be computed using averaged reservoir properties in each 1-D matrix gridblock along the DTOF, including permeability, bulk volume, and shape factor. This approach is similar to the existing FMM-based simulation approach for DPSK reservoir models (Fujita et al. 2016, Iino 2018), but differs in a sense that there are matrix-matrix connections. Another potential approach to compute the 1-D transmissibilities is to take advantage of the local quadratic equation based on the finite-volume discretization of the Eikonal equation (Eq. (3.13)).

$$\sum_{i}^{\substack{\text{upstream}\\\text{connections}}}\left(\left(\tau_c-\tau_i\right)^2 T_{A,i}\right)=V_p\mu c_t \qquad (3.13)$$

While τ_c (DTOF at cell center) is an unknown variable during the FMM calculations, after we compute the DTOF and perform coordinate transformation, Eq. (3.13) can be applied to compute 1-D transmissibilities using the known DTOF, pore volume, viscosity, and total compressibility. The transmissibilities within and between the domains can be computed solely based on Eq. (3.13). Although seemingly promising, this option is new and has not yet been tested. We recommend conducting validation and testing in future work. Once the 1-D transmissibilities are obtained, we can utilize them to build a 1-D DPDK simulation model. While we focused on single-phase flow problems above, extensions to multiphase flow can be readily done through the application of multiphase diffusivity (Iino 2018).

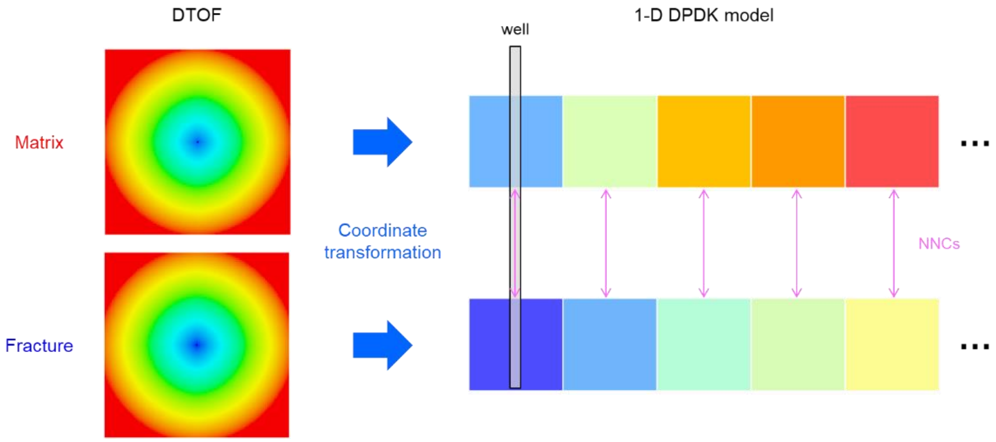

Figure B5 An illustration of the FMM-based simulation approach for a DPDK reservoir model